Chapter 5

Anemometry package: description and test

This chapter gives an overview of the equipment used for the measurement of wind velocity in the wheat field. Unlike the three-dimensional measurement system described in Chapter 4, the anemometers had already been used at Cranfield University prior to the research, so part of the technology was already available. For that reason, besides the basic description of the different elements which compose the anemometry package, the emphasis in this chapter is put on the assessment of the performance of the system as a whole, of its limitations and practical field use. Section 5.1 describes the hardware in use, and section 5.2 concentrates on the associated software which was developed during the research for wind data logging. Then sections 5.3 and 5.4 move on to present the tests performed on the hardware and the software, respectively, in order to assess their capability to make accurate field measurements. Section 5.5 shows how the raw wind data is converted to useful wind velocity vectors which can be related to the wheat motion measurements. Finally section 5.6 shows how the anemometry system is used in practice, and makes some concluding remarks on the system as a whole.

5.1 Description of the hardware

5.1.1 Overview of the system

The hardware available for the anemometry is composed of:

- 12 Digital Vane Anemometers (DVA), mounted in four triads,
- 4 mounts, each supporting one triad,
- 3 supporting poles for the mounts,
- 4 sets of three 50m long cables connecting the triads to the processing computer,
- 1 computer for data collection and processing (Viglen 486DX2 66MHz, 8MB RAM),

- 1 interface box with 15 pin connectors,
- 1 DVA-PC interface board, to connect the output cables of the DVAs with the computer,
- 1 analog/digital I/O board to collect data from the DVA-PC interface board,
- 1 clock board for sampling frequency selection,
- 1 wind vane,
- 1 power generator for the computer, and 1 5V battery for the boards and the wind vane,

Figure 5.1 gives an overview of the anemometry package.

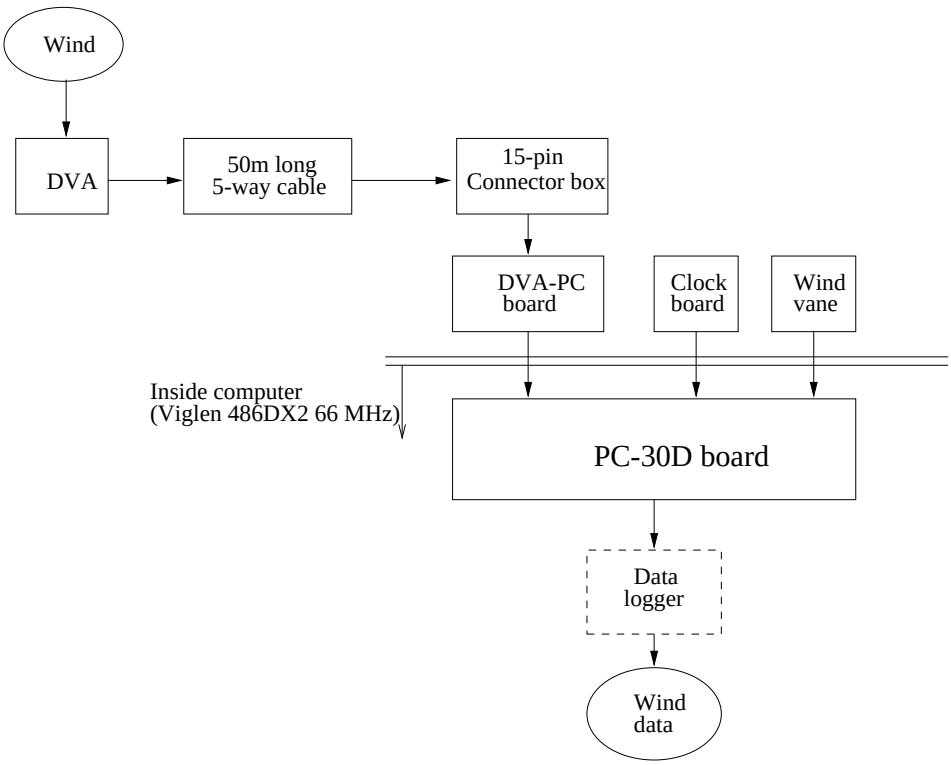

Figure 5.1: Schematics of the anemometry equipment. Solid line boxes denotes hardware, and the dotted line box denotes the software

The anemometers are connected to the 50 m long cables in order to allow measurements away from the wind data logging system. The long cables are themselves connected to a 15-pin connector box which acts as an interface with the electronics boards necessary for data logging. For reasons which are detailed later in the chapter, two boards are used by the system in its current version, although future developments could easily integrate the functions of the two boards in a single one. A wind vane is also in use by the system in order to provide an independent reading of the wind direction which can be compared to the wind direction obtained from the anemometers. Finally the system requires a power generator for the computer and the electronic boards.

5.1.2 The Digital Vane Anemometers

The choice of digital vane anemometers for field use is dictated by their ease of use in field conditions and their precision. Their successful use in other experiments at Cranfield University [42] suggested that they would be adapted to the purposes of the research.

DVA inputs and outputs

A DVA is composed of two pairs of photodiode/phototransistor, one pair to monitor the signal speed and the other for the signal direction. The photodiode (L.E.D. TIL23) illuminates the phototransistor (LS600) through gaps in the rotating hub of the anemometer. When illuminated the phototransistor conducts and an electronic square pulse is then emitted. The stronger the wind, the faster the vane rotates, and therefore the more often the phototransistor is illuminated. It follows that the pulse rate n (Hz) is linearly related to the wind speed v (m.s^{-1}). The linear relation was established in [63]:

$$v[m.s^{-1}] = 0.0243.n[Hz] + 0.0994 \tag{5.1}$$

The multiplying coefficient 0.0243 is related to the inertial properties of the vanes (MICA vanes) and the constant 0.0994 corresponds to the minimum wind speed necessary to actuate the vanes and their rotating mounting.

The necessary inputs to the DVAs are the wind which actuates the MICA vanes, and a 5V supply for its electronic components. The voltage to the two pairs of photodiode/phototransistor is supplied by three input lines (one for each pair and a ground line). The two outputs lines of the DVAs carry the speed signal and the direction signal. The direction signal is also composed of the same square wave as for the speed, but its phase is shifted compared to the speed signal. The DVAs are calibrated so that a positive phase shift corresponds to a positive wind direction, i.e. from the positive face of the DVA to its negative face. The positive and negative faces of the DVAs are marked. So in total there are 5 input/output lines which need to be connected. They are connected to the 15-pin connector box described in the next section.

DVA mounts and axis convention

The DVAs are mounted in triads, in order to retrieve a wind velocity vector. The axis convention of a DVA triad is as follows: the x-axis is along the mean wind direction, pointing in the direction of the motion of the wind, the z-axis is vertical upwards and the y-axis completes the orthogonal triad, i.e. it is pointing to the left when the triad is looked in the direction of the x-axis. The orientation of the x-axis in the mean wind direction ensures that the wind direction read by each DVA is always positive. The DVAs in a triad are numbered from 1 to 3: the DVA $n°3$ is the middle one, the DVA $n°1$ is on the positive side of the y-axis, i.e. on the left hand side when the triad is looked in the direction of the x-axis. The DVA $n°2$ is the remaining one. Figures 5.2 shows the numbering convention of a DVA triad.

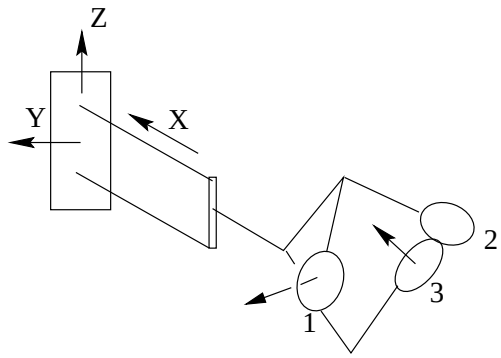

Figure 5.2: Axis convention for the DVA triad

Orientation of the DVAs in a triad

The direction cosines of the DVA axes is presented in [63] and reproduced here in Table 5.1. It gives the components, in the (x,y,z) triad coordinate system, of the unit vectors parallel to the main axis of the three DVAs. The anemometers are mounted in a non-orthogonal triad in which each DVA is at about 35° with respect to the mean flow. The reason for using a such a non-orthogonal triad is that, if the x axis of the triad is aligned with the mean wind direction, each DVA operates in a flow of air at an incident angle ranging from 0° to 60°, where the anemometers perform accurately [63].

DVA number	x component	y component	z component
1	$\sqrt{\frac{2}{3}}$	$\frac{1}{2}$	$-\frac{1}{2\sqrt{3}}$
2	$\sqrt{\frac{2}{3}}$	$-\frac{1}{2}$	$-\frac{1}{2\sqrt{3}}$
3	$\sqrt{\frac{2}{3}}$	0	$\frac{1}{\sqrt{3}}$

Table 5.1: Direction cosines of the standard DVA triad

The 3 poles used to support the DVA triad mounts are aluminium cylindrical tubes. One pole is used to support two triads, one at canopy level, the second one higher. The two other poles support one triad each, placed at canopy level. Figure 5.3 shows a DVA triad in the wheat field.

5.1.3 Cabling and DVA-PC interface

The DVAs are connected to a 15-pin connector box. Each of the 15 connections is composed of 5 pins which are connected to the 5 input/output lines of each DVA. The connection convention of the box is shown in Figure 5.4.

Each of the 5 pins of one connector is connected to each line of the 5-way 50 m long cable, which allows field measurements away from the PC and interface boards. To provide a low noise data transmission with these long cables, a current loop circuit is created on the DVA-PC interface board. On this board Schmitt triggers are also present (SN74LS14), in order to improve the receiving characteristics of the signals. This part of the interfacing was already available and is described in detail in [64].

Figure 5.3: DVA triad in operation in the wheat field

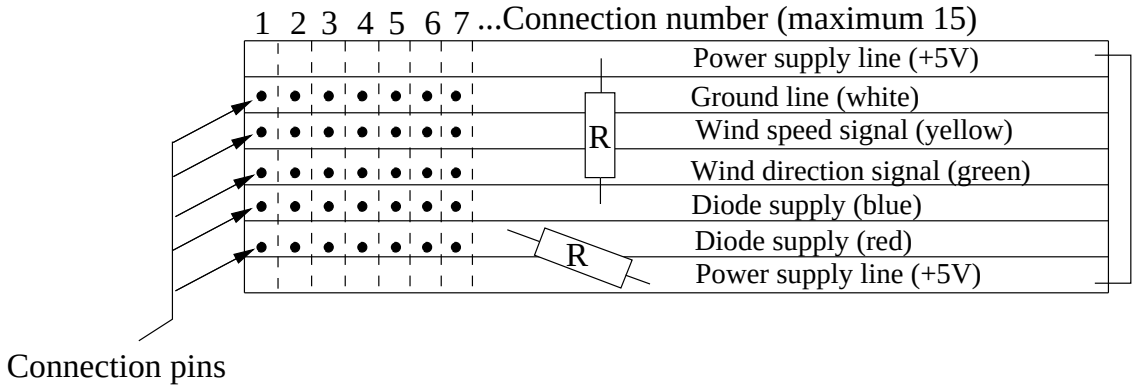

Figure 5.4: Connection lines of the interface box

The DVA-PC board can also provide a real-time direct logging of the wind data, together with a software control of the sampling frequency and convenient editing of the data. However, the tests made on the board and described in Section 5.3 will show that it cannot be used reliably and for that reason an alternative data logging system was built (to be detailed in the next sections). However the current loop circuit on the board can be used and is the reason why the original board is kept here. The outputs of the Schmitt triggers contains the speed information delivered by the DVAs. These outputs are read by the PC-30D board.

5.1.4 The PC-30D analog-digital I/O board

The PC-30D board is plugged into any of the expansion slots of a PC. It operates from the +5V, +12V, and -12V lines of the PC bus. Its subsystems are:

- An analogue to digital converter (ADC).
- A digital to analogue converter (DAC).
- A digital I/O subsystem, acting as an interface for the transfer of digital data from and to the PC bus, to and from one or more peripheral devices connected to the PC-30D board.
- An analogue I/O subsystem, for the same purposes as its digital equivalent.

Each output of the Schmitt triggers carrying the wind speed information (more precisely the square wave signal whose frequency is related to the wind speed) is connected to a digital channel of the board via a male 50-way D-type connector. The board is also connected to the wind vane via its analogue channels. So for the purpose of data collection from the DVAs and the wind vane, the ADC and DAC of the board are not used.

The board is supplied with a set of real-time device drivers which can be called from several programming languages including C. It is the language chosen to drive the board from the PC. The C program is described later in this section. The data channels containing the DVA outputs are accessed by a library of functions and the data is saved at the sampling frequency set by the clock board.

5.1.5 The clock board

The wind speed measured by the DVAs cannot be recorded continuously and need to be sampled at a user-defined sampling frequency. There are two ways to select this frequency: the PC internal clock can be used to read the DVA output at the chosen rate (software control), or alternatively an external source of precise known frequency can be input into the PC and used as a reference signal giving well defined and constant time intervals (hardware control). Section 5.3 will show that the use of the PC internal clock, in conjunction with the DVA-PC interface board, yields unreliable sampling time intervals which tend to cause a time drift with respect to real measurement time. For that reason an external clock is used to provide a steady, reliable, sampling frequency. The main components of the clock board are:

- a 10MHz oscillator,
- 5 frequency dividers connected in series,
- a switch/multiplexer assembly for frequency selection.

The frequency dividers (74HC390N/393N) divide the 10MHz frequency of the crystal oscillator into lower frequencies ranging from 0.25Hz to 100kHz. 7 of these frequencies (1, 2, 5, 10, 20, 40, and 100Hz) are connected to the multiplexer (74HC151N) for selection by the switch. Schmitt triggers (74HC04N) are also used in the circuit in order to generate a sharp square wave output signal. The different connections on the clock board and its layout are detailed in Appendix D, from which it is possible to reproduce the board if required. Due to the very high frequency of the oscillator, some special care needs to be taken in the layout of the board in order to minimise interferences. In particular, the crystal oscillator and the first frequency divider should be mounted close to each other, connected with thick insulation cables, and isolated from the other wires.

The clock output of the board is a square wave signal of selected frequency and is connected to one of the digital channels of the PC-30D board. It is read by the logging software, as described in Section 5.2.2, and for each cycle of the clock the number of pulses from each DVA is read and saved to a text file.

Additional elements are also present on the clock board, although they are not directly necessary for its use. They are placed on the clock board to minimise the number of space taken by the hardware. These additional elements are:

- a wind vane connector and its associated circuitry, to be detailed later in Section 5.1.6,

- a circuit used for simulation of wind conditions and testing of the system, presented in Section 5.4.2,

- a 0.25Hz LED flashing circuit, to be used for synchronisation with the video data.

5.1.6 The wind vane

With the use of four triads of DVAs, an additional wind vane is not absolutely necessary in the experiment. However, it is very useful to have a mean of verifying that the wind direction given by the triads is valid. So the wind vane is added in the experiment to provide this way of qualitatively comparing the DVAs readings to a more simple, easy to set up data source. The wind vane used for that purpose is a W200P from *Vector Instruments*. It is composed of a precisely wound potentiometer connected to a vane arm/fin assembly. Figure 5.5 shows the wind vane connections.

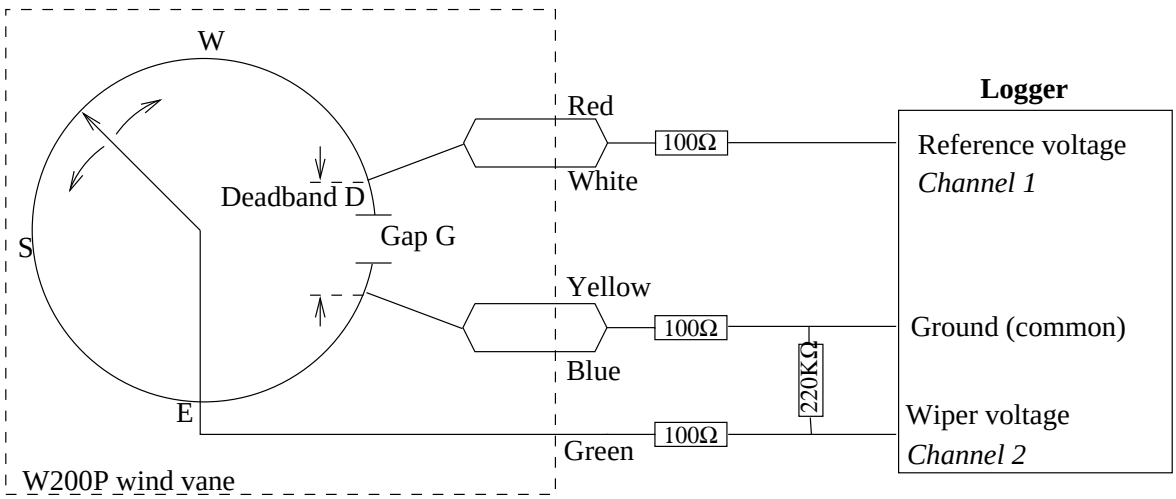

Figure 5.5: Wind vane connections

The 100Ω resistor connected to the Red/White cables brings the output reference voltage to about 4.8V so it does not reach the maximum voltage readable by the PC-30D board (5V). The 220kΩ resistor prevents linearity degradation at low angles. The wind direction WD is then calculated from the output voltage of channels 1 and 2:

$$WD = (360 - D).(Channel2/Channel1) + D/2 \tag{5.2}$$

where D is the "deadband", i.e. the area where the potentiometer of the wind vane is opened in order to make the necessary connections. The outputs of the wind vane are read by the analogue channels of the PC-30D board and the corresponding wind direction is calculated for each cycle of the clock.

5.1.7 Power supply

A power generator powers the PC. Its autonomy with such a load is of the order of hours, which is sufficient for the purpose of wind data logging. The clock board, the DVA-PC interface board and the DVAs themselves, via the DVA-PC interface board, are powered by a 5V battery which is plugged to the power generator. Figure 5.6 shows the power generator, the computer, the 15-pin connector box and the cables used in the field conditions for wind data logging in the wheat field. It can be seen that the entire equipment is easily transportable in a car.

Figure 5.6: Computer, 15-pin connector interface box, cables and power generator used for the wind data measurements

5.2 Software description

5.2.1 Requirements and specifications

Software is necessary in order to read the data sent from the DVAs, via the different interfaces described in Section 5.1. Equation (5.1) shows that the wind speed is obtained from the pulse rate n in Hz, i.e. the number of square waves sent by the DVA in one second. For a given sampling frequency f_s, the pulse rate n is obtained

by counting the number N_{le} of leading edges of the square wave in a time interval $1/f_s$. Then the pulse rate is obtained by:

$$n = N_{le}.f_s \tag{5.3}$$

From Equation (5.3) it becomes clear that the main function of the software is to count the number of leading edges received from the DVAs. The count must be performed in real time, and stored at the desired sampling frequency. In addition to this the software reads the wind vane data and stores wind direction at the same sampling frequency. So the software requirements are to:

- Detect the leading edges of the square wave signal sent from the DVAs.
- Detect the leading edges of the clock signal in order to know the sampling frequency.
- Read the wind vane data and calculate the wind direction according to Equation (5.2).
- Store the number of leading edges counted in the past cycle, at each sampling interval $1/f_s$.
- Save the data in a convenient format (text file).

These tasks must be performed in real-time, i.e. the program must store wind data values from all DVAs and from the wind vane as they happen to be measured at the same instant, or more precisely as they are received from the past sampling interval. For this purpose, the processing time must be short enough to not miss one or more leading edges of the signals. The real-time capability of the program is tested in Section 5.4. The next chapters give an overview of the code.

5.2.2 Implementation

Detection of the PC-30D board

The library supplied with the board needs to be called by the C program in order to be able to use the PC-30D drivers. Once the base address defining the position of the board on one of the PC slots is defined in the program, the diagnostic routines of the board can be executed. These routines are essential to make sure that the board is recognised by the PC. They also find the type of board used (from the PC-30 series of I/O boards).

Digital channel reading

The digital I/O section of the PC-30D board consists of three 8-bits ports (A, B, and C). After initialisation, the ports can be configured to input or output mode. In the case of wind data logging they are used as input ports. Each bit of a port corresponds to a single digital channel which can consequently be either in a low (bit 0) or high (bit 1) state. The state of the bit is determined by the output voltage

received from the DVA. Therefore a change from bit 0 to bit 1 corresponds to a leading edge of the DVA output square wave.

The function which obtains the value of one of the input ports (function "din") returns an integer whose value ranges from 0 to 255. This value gives the state of each 8 DVA channels connected to the port.

The software is programmed to receive 12 DVA channels (4 triads). The outputs of the 12 Schmitt triggers related to the 12 DVAs are connected to the last 7 digital channels (last 7 bits) of port A, A1 to A7, and the first 5 channels (first 5 bits) of port C, C0 to C4. The first channel of port A (A0) is reserved to the clock board output.

Leading edge detection and count

The program runs in a loop which is stopped when the user presses a key of the keyboard. In each loop, the digital channels are read. For a given channel, a leading edge is found by detecting a change from bit 0 to bit 1. This is done for the channels connected to the DVAs but also for channel A0, in order to detect a full cycle of the clock and consequently determine when to sample the data collected in the past time interval $1/f_s$ (s).

When a leading edge is detected for a given DVA channel, a counter associated with this channel is incremented by 1. In parallel to this counter increment, the code checks at each cycle of the loop if the clock has reached a new leading edge. If so, the integer number in the counter variable is the number of leading edges in the past clock cycle. It is stored in a variable, and the counter is re-initialised. This counting operation is performed simultaneously for the 12 channels.

Analogue channel reading

The analogue part of the board accepts 15 channels. For the purpose of wind vane reading, 3 channels are required, connected respectively to the ground (0V, read on the analogue channel 3), channel 1 (output voltage, read on the analogue channel 1), and channel 2 (reference voltage, read on the analogue channel 0) of the wind vane. Each channel returns a 16-bit integer (range from 0 to 4095) which is linearly related to the voltage. The board can operate with three voltage ranges. With the wind vane, whose expected voltage varies between 0 and +5V, the most adapted functional voltage range for the board is -5/+5V. In this case, the analogue voltage V relates to the output 16-bit integer (digital code D) by the relation:

$$V = (D - 2048) * 5/2048 \tag{5.4}$$

When a leading edge of the clock signal is detected the voltages from the three analogue channels are read and the wind vane angle is calculated according to Equation (5.2). The value obtained is stored in a floating point variable.

The analogue channel $n°5$ of the board is connected to the clock signal. It is also stored in a variable which provides a convenient time log of the experiment and is also used for synchronisation of the wind measurements with the video data (see Chapter 6). The time variable is updated every 4 seconds.

Memory efficient data storage

The data outputs of the code and their default storage requirements from the MS-DOS C compiler are:

- The number of pulses from 12 DVAs. They are integers and the MS-DOS C compiler allocates by default 4 bytes of data for each reading.
- The wind vane angle, which is a floating point number. By default each reading is allocated 4 bytes by the compiler.
- The time counter from the L.E.D. circuit. As an integer, it requires 4 bytes per reading.

With the C compiler used in its large memory model configuration, the maximum size of a single variable is limited to 64 Kbytes. So if one variable was to contain all 12 output number of pulses from the DVAs, the maximum number of readings would be 64/(4*12)=1333. This value, at a sampling frequency of 5Hz, corresponds to about 4.5 minutes of data, which is too short to work conveniently in field conditions. For that reason, a more efficient way to store the data is required.

It is possible to decrease the memory requirements imposed by the C compiler in different ways. First the obvious way is to attribute a different variable for each DVA outputs. This will clearly increase the maximum data collection time. At 5Hz, the total time available for data collection becomes approximately 53 minutes, which is sufficient for the purposes of the experiment here.

There is however a way to increase this value even more, to allow measurements to be taken on longer time scales if necessary. In practice the number of pulses counted in a single clock cycle never exceeds values of about 50. So it is possible to store these values in a single byte, rather than the default 4 bytes. In theory only 6 or 7 bits are even sufficient, but the C compiler does not allow to store data in packets of less than 1 byte. A convenient way to convert the 4 byte integers to a single byte variable is to store it in a variable of character type ("char" type). The default allocation for a char type variable is 1 byte.

Similarly, the clock counter values (representing seconds) can be stored in 2 bytes instead of the default 4 bytes. Using 2 bytes allows the storage of values up to 65535. This maximum value translates into a possible record time of about 18 hours. This obviously exceeds the requirements but using a single byte (i.e. up to 255 seconds) is not enough here. Finally the floating point values given for the wind vane angles can be stored in 2 bytes only instead of the default 4 bytes, by multiplying the floating point value by 100, and storing the integer part of the result. Then, when needed, the value can be divided back by 100. This method is a standard way to store real data in a more compact way.

With this data storage strategy, the maximum time of the field measurements now exceeds the requirements. In the code the data from the DVA channels is gathered by groups of 3 (one variable per triad). Each of these four variables is a character array of 60000 values. So in this configuration the maximum number of readings is 20000. It represents more than 1 hour of data at a sampling frequency of 5Hz.

Data saving

The data are saved every 1500 readings, i.e. every 5 minutes at 5 Hz. This value is chosen to represent the maximum amount of data allowed to be lost in case of a computer problem during the recording phase. The data are not saved line by line because saving operations, although they take a short amount of time, could nonetheless result in a loss of one or more leading edges detected in each cycle.

The data are written in a series of text files of a user-specified name. Each packet of 1500 data lines is stored in a separate file because a single data file could exceed in memory size the capacity of a floppy disk (1.44 Mbytes) and would complicate the data transfers. The program prompts the user for a base file name before starting the recording (e.g 'datalog') and each 1500 is saved in a filename having the base filename followed by a number iterated each time ('datalog1.txt', 'datalog2.txt', etc...). Each line of the data files contains, in the following order, the wind vane angle, the number of pulses read from the 12 DVAs, and the time counter. Each line corresponds to a cycle of $1/f_s$ second.

On-screen display

As well as being stored in text files, the data are displayed on the screen in order to control visually that no error occurs during the recording.

5.3 Hardware testing

The tests were performed indoors initially, and then outdoors in order to assess the practicalities of the field experiment.

5.3.1 DVAs and cabling

The DVAs were individually tested, together with the 15 pin connections of the interface box and the 5-way cables connecting them. Particular attention is to be paid to the centering of the rotating hub of the anemometer. If not accurately centred, some friction between the hub and its case can occur, therefore limiting the rotation and resulting in underestimated wind speed measurements. After testing some hubs were changed and re-centred. The 50m long cables are in a good operational state. The connectors used are Binder type connectors, well suited for field use as they are waterproof. The base of the DVA supporting poles are hammered in the soil. They should be placed deep enough so that they do not move during the measurements.

5.3.2 DVA-PC interface board

Test of the board for the entire wind data logging and processing

As explained in Section 5.1.2, the board contains the current loop circuit components and the Schmitt triggers. It also contains a data logging circuitry which can be software driven as described in [64]. This software outputs in a text file the time at which the sample was taken and the wind speed derived from the connected

anemometers. As it is readily available, the possible use of this entire board and associated software needs to be investigated. If the results of the tests show reliability and accuracy for the board, then it should be used. As the next sections will show, this is not the case and explains why an external clock board and an external analogue/digital I/O board were used, as well as a separate data logging software.

Testing of the sampling time intervals

Table 5.2 shows an example of the output text file given by the software. It contains the time data as well as wind speed data from 6 different anemometers.

Sample	Time				f_s	Wind speed (m/s)					
n°	h	mn	s	$\frac{1}{100}$ s		0	1	2	3	4	5
0	15	52	40	90	5	2.04	1.44	1.92	1.68	1.19	2.04
1	15	52	57	32	5	1.80	1.19	1.92	1.68	0.95	1.56
2	15	52	57	54	5	1.68	1.19	1.80	1.31	0.95	1.68
3	15	52	57	76	5	1.92	1.07	1.68	1.80	1.07	1.68
4	15	52	57	93	5	1.80	0.95	1.56	2.53	1.19	1.80
5	15	52	58	15	5	1.56	0.83	1.56	2.04	0.83	2.04
6	15	52	58	37	5	1.56	0.71	1.56	1.31	0.71	1.80
7	15	52	58	59	5	1.44	0.71	2.04	1.07	0.59	1.92
8	15	52	58	75	5	1.31	0.83	2.04	0.95	0.71	2.04
⋮	⋮	⋮	⋮	⋮	⋮	⋮	⋮	⋮	⋮	⋮	⋮

Table 5.2: Example of the output file given by the software

Table 5.2 shows that the time displayed is not regularly spaced as it should be. With a sampling frequency of 5 Hz the time between two readings should be 0.2 s and this is not the case. Apart from the first sampling time which differs from the second by about 17 s and should not be taken into account, the time difference between two samples is never exactly 0.2 s as expected. Taking the sampling time of the sample $n^\circ 1$ as a reference, the difference between the time given in the output text file and a regular time calculated by adding 0.2 s between the samples is plotted in Figure 5.7.

In addition to the irregularity in the time given by the computer clock and responsible for a "time band" of about 0.06 s, there is a slow time drift between the time given by the software and the expected regular time. From Figure 5.7, it appears that the time difference between the displayed time and the expected time is about 0.1 s after 300 s. This slow time drift can be explained by some rounding errors made by the computer, and most probably because each loop of the software does not take exactly the same time depending on the amount of data processing required. The software code driving the board and processing its data throughput was not available to state precisely on this point.

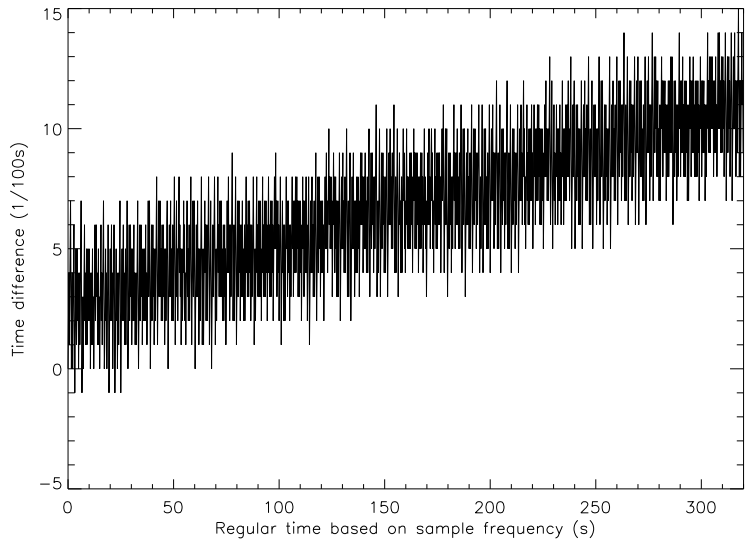

Figure 5.7: Difference between the time given by the software and a regular time calculated from the sampling frequency

Quality of the wind speed data recorded by the board

Ignoring for one moment the time drift, a DVA output wind speed obtained after processing by the board and associated software is plotted in Figure 5.8.

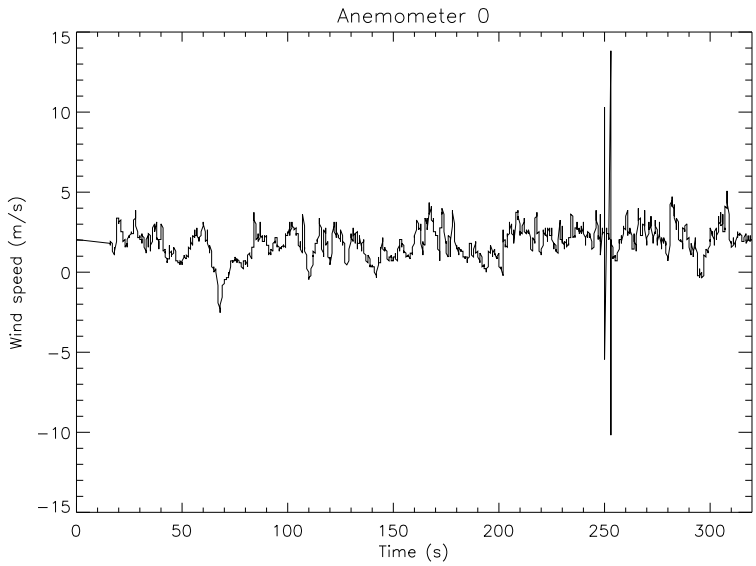

Figure 5.8: Wind speed measured by a DVA and processed only through the DVA-PC interface board and associated software

The two main features of Figure 5.8 are:

- The existence of negative values of the wind speed, which emphasises the fact that the mean wind direction is difficult to find in low wind speed conditions. The fact that the wind can sometimes have negatives values means that it can come at a high incidence angle from the normal axis of the DVA, and in this case the DVA readings are not accurate [63].

- The presence of some "overflow" readings at t≈255 s. In fact it is found that these overflow readings are more frequent when a higher number of DVAs are connected to the board. They also appear more frequently when its central processor is manually moved or touched, which tends to support the existence of a loose connection in the circuit. The number of overflow readings when all 12 DVAs are connected is so high that the is unacceptably corrupted.

Conclusion on the potential use of the DVA-PC interface board for data logging

Both the existence of a slow time drift and the presence of overflow readings from the board make it an unreliable system for direct wind data logging. For that reason, the only part of the board used in all further measurements is for the implementation of the current loop circuit. It explains the need for an external clock signal (to generate steady sampling intervals) and an external data logging board (to avoid erroneous readings).

5.3.3 PC-30D board

The board was first tested with the demonstration programs supplied with it. These programs are used to perform some simple operations such as access to the board via its base address, initialisation, reading and writing on the analogue and digital channels. The DAC and ADC parts of the board are not tested here since they are not required for the measurements. The preliminary tests yielded the results expected. They are not detailed here as they are very basic tests and it will be shown later that the PC-30D board is operational, when the software tests are described.

5.3.4 Clock board

Each element of the clock board was tested individually. Particular attention was paid to the output lines of the crystal oscillator, which can generate interferences. The thick insulation cables used to limit the interferences are well adapted as no interference noise was detected on the oscilloscope traces. It is worth mentioning here that the first design of the board did not include thick cables and some interferences were observed. The use of well insulated cables is therefore necessary and provides a significant improvement.

The output frequencies from the different frequency dividers were measured with an oscilloscope. They are equal to their expected value. The accuracy is here very good and there is no detectable difference between expected and measured values. This is due to the excellent precision of the crystal oscillator.

5.3.5 Wind vane

The wind vane output voltages agree with their expected values. For an input voltage of 5V and with the resistor shown in Figure 5.5, the reference voltage (channel 1) is 4.86V and remains constant. The channel 2 voltage is linearly to the vane angle as

expected. Angle values collected around the 0-360° boundary are more unstable and should therefore be interpreted with care. They correspond to the region of the gap at the ends of the potentiometer track. For accurate measurements, the orientation of the wind vane should be such that the potentiometer is not in the region of the deadband, so it should be oriented so that the angle 180° (the "south" direction on the vane, see Figure 5.5) faces the mean wind direction. No absolute reading of the wind direction is obtained in this way, but it is not a problem in the case of the measurements described here, since the wind vane is only used as a means to check the wind direction given by the anemometers.

5.4 Software testing

5.4.1 Test requirements

The software in its final version described in Section 5.2 is required to log and save wind data in real-time. For that reason the main purpose of the tests presented here is to quantitatively assess the real-time capability of the program. More precisely, the tests will answer the following questions:

- In normal wind conditions, is there a miscount of pulses due to too long processing time in each cycle?
- Can the software count reliably the number of pulses from the DVAs in all wind conditions (low to very strong wind)?
- How much data is lost during the saving phase and, in that respect, is it appropriate to save data every 1500 readings?
- Can the software work reliably at all sampling frequencies?

These four questions are answered in the remainder of this section.

5.4.2 Electronic simulation of steady wind conditions

The test requirements listed above can be answered by simulating artificially a perfectly steady wind, i.e. a constant number of pulses per time interval. In [63], this is done in a wind tunnel, but for the purpose of the software tests described here, a much more convenient way is to connect one input of the 15-pin connector interface box to a steady square wave signal of known input frequency f_i. The input frequency is equivalent to the pulse rate n introduced in Equation (5.1)Therefore the number of leading edges counted in a time interval $1/f_s$ can be re-written as:

$$N_{l.e.} = \frac{n}{f_s} = \frac{f_i}{f_s} \tag{5.5}$$

The electronic circuit used to simulate these steady wind conditions is built on the clock board. It is sketched in Figure 5.9.

The transistor simulates the phototransistor inside the DVA and the input square wave generator simulates the regularly illuminated photodiode. The voltage V_{BE} is a

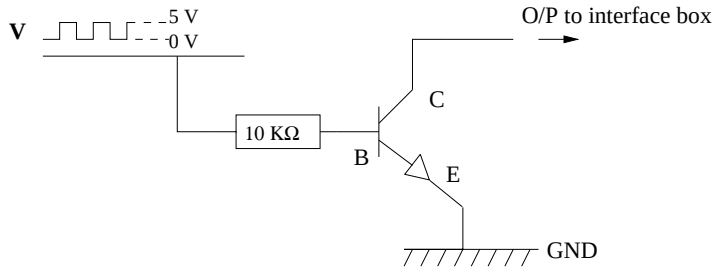

Figure 5.9: Electronic circuit for simulation of steady wind conditions

square wave of frequency f_i and amplitude ≈ 0.55 V (working Base-Emitter voltage of the transistor). At the output of the circuit (collector of the transistor), the voltage V_{CE} is a square wave of frequency f_i and measured amplitude ≈ 4 V. The output is connected to the pin of the interface box which carries the wind speed signal.

Program test in normal wind conditions

With the electronic test circuit above, several simulations were carried out for a whole set of input frequencies (from 10 Hz to 900 Hz) and of sampling frequencies (5, 10, 20, and 40 Hz). Table 5.3 is an example of the data collected, for an input frequency of 100 Hz and all 4 sampling frequencies. $f_i = 100$ Hz corresponds to a simulated wind speed of about $2.5 m.s^{-1}$, i.e. normal wind conditions. Only the first 10 data lines of the program output text file are presented.

Sample	Sampling frequency f_s			
$n°$	f_s=5 Hz	f_s=10 Hz	f_s=20 Hz	f_s=40 Hz
0	19	10	5	2
1	19	10	6	2
2	20	9	5	2
3	20	9	6	2
4	20	9	5	3
5	19	10	5	2
6	19	10	5	2
7	19	10	5	2
8	20	10	6	3
9	20	10	5	3
10	20	10	6	3
⋮	⋮	⋮	⋮	⋮

Table 5.3: Example of the number of pulses detected for f_i=100 Hz and f_s=5, 10, 20, 40 Hz

The number of pulses per sampling interval expected from Equation (5.5) is N_{le}=20, 10, 5, and 2.5 for f_s=5, 10, 20, and 40 Hz respectively. In practice, this number is an integer and oscillates by one count. For input frequencies which are not a multiple of the sampling frequency, the output number of pulses N_{le} will vary

between the two integers directly superior and inferior to the ratio f_i/f_s. Even when f_i is a multiple of f_s, the number of pulses is not strictly constant. This is due to the fact that in practice the two frequencies f_i and f_s are not exactly proportional and the slight shift between the nominal and actual values is enough to result in a variation of one counted pulse.

From these first results, two conclusions can be drawn. First, it appears that, in normal wind conditions, there is no miscount of the number of pulses originating from too long processing time in each loop of the program. In normal wind conditions, the software counts correctly the number of pulses from the DVAs, and consequently the wind speed is accurately recorded in real time.

However, the second conclusion is that, even for a perfectly steady wind the number of pulses counted in one clock cycle will regularly vary by one count due to the digital nature of the counting operation. The main practical implication of the oscillation of the number of pulses per sampling interval is that it translates into an oscillation of the wind speed recorded by the system. This oscillation gives the precision of the whole system in the retrieval of wind speed by the DVAs. If ΔN_{le} is the accuracy for the number of pulses counted by the system (here ΔN_{le}=1), then the accuracy Δv in the wind speed retrieval is, from Equations (5.1) and (5.5):

$$\Delta v = 0.0243.f_s \Delta N_{l.e.} \tag{5.6}$$

For the four sampling frequencies introduced above, the associated wind speed accuracies are given in Table 5.4.

Sampling frequency f_s (Hz)	Wind speed accuracy Δv (m.s^{-1})
5	0.1215
10	0.243
20	0.486
40	0.972

Table 5.4: Accuracy of the wind measurement system for the different sampling frequencies

From Table 5.4 one can see the advantage of working at a lower sampling frequency. However this is to be traded-off against the necessity to measure the wind velocity vector at a high enough rate in order to follow the crop motion measurements which are performed by the video system at 25 Hz.

Reliability of the software in high wind conditions

The input frequency f_i of the simulation circuit is now varied from low frequencies of the order of the sampling frequency f_s to high frequencies (900 Hz). The number of pulses collected for each clock cycle is averaged over 100 cycles and Figure 5.10(a) shows the variation with f_i of this average number of pulses counted by the software. The expected number of pulses is equal to the ratio f_i/f_s. Figure 5.10(b) shows the difference between the average number of pulses counted at each input frequency f_i and the corresponding expected value f_i/f_s. For comparison between the 4 sampling

frequencies f_s, this difference is expressed as a percentage of the expected number of pulses in each case.

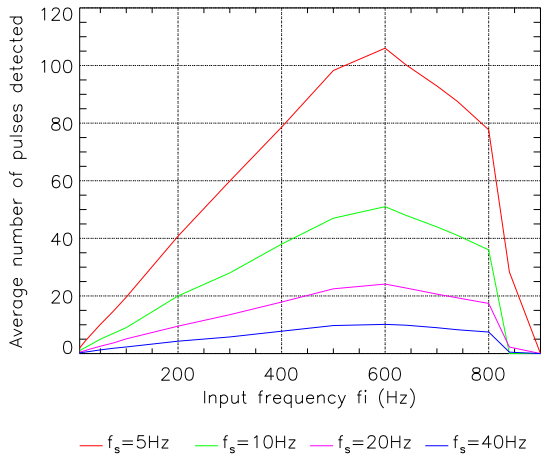

(a) Average number of pulses counted for different input frequencies

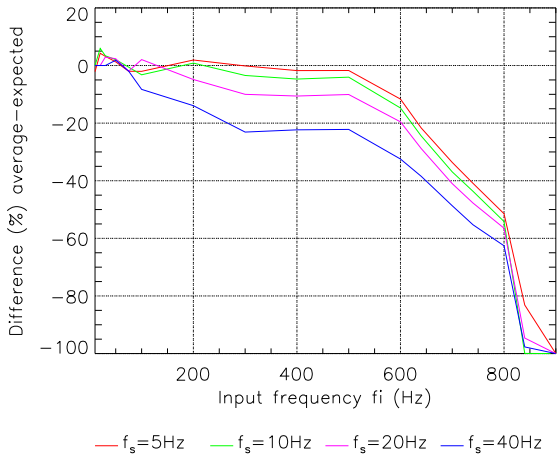

(b) Difference between the expected number of pulses and the actual average number counted

Figure 5.10: Variation of the number of pulses counted by the program as a function of the input frequency f_i of the simulated steady wind

At low input frequencies (f_i <500 Hz), Figure 5.10(a) shows that the number of pulses counted by the software increases with the input frequency f_i. For a given input frequency, the number of pulses being counted in a sampling interval $1/f_s$ is higher for lower values of f_s. At input frequencies higher than 400 to 500 Hz, the number of pulses counted by the software decreases. This is due to the fact that the software starts missing some pulses due to its own processing time: at higher frequencies the software is no longer capable of counting the pulses in real time. Figure 5.10(b) helps to quantitatively assess the real time capability of the software. For sampling frequencies of 5 to 10 Hz, the number of pulses counted corresponds to its expected value for f_i <500 Hz. For f_i >500 Hz, the software yields errors of more than 5%. For f_s=20 Hz and 40 Hz, the 5% error bound is reached at $f_s \approx$200 Hz and 80 Hz respectively. This error bound of 5% is practical here because it corresponds to the accuracy of the wind speed retrieval with the DVAs, as detailed in the pulse rate to true air speed calibration presented in [63]. So from Figure 5.10, the maximum input frequencies at which the software can be used is estimated and translated into maximum wind speeds from Equation (5.1). These wind speeds are given in Table 5.5. The figures show that the software will work in most wind conditions at f_s=5 Hz and 10 Hz. However, its use at higher sampling frequencies is restricted to mild wind speeds.

Data loss during the saving phase

By saving the data every 1500 lines only, it is accepted that a small amount of cycles will be missed but the reliability of the data collected at any other time is improved

Sampling frequency f_s (Hz)	Maximum pulse rate (Hz)	Maximum wind speed (m.s^{-1})
5	500	12.2
10	500	12.2
20	200	5.0
40	80	2.0

Table 5.5: Maximum measurable wind speed with the software (5% error bound)

(see section 5.2.2). Saving 1500 lines of data takes approximately 1 second with the computer used for the measurements (486 DX2 66 MHz). This represents a data loss of 0.33 % at f_s=5 Hz, which is acceptable for the statistical analyses to be made. At the other sampling frequency extreme (f_s=40 Hz), 2.67% of data is lost during the saving phase. It is also a small amount, which is set to be acceptable for the measurements. However, the data loss can be reduced by saving data less frequently, at the risk of losing more in case of a computer problem during the recording phase. Less data is lost when saving procedures are less frequent because the saving time required by the computer is not linearly proportional to the amount of data lines present in the file.

Relation between software capability and sampling frequency

Table 5.5 shows that the software can be used in all wind conditions up to maximum wind speeds of about 12 $m.s^{-1}$ for sampling frequencies up to 10 Hz. At frequencies higher than 40 Hz, the software in its current form cannot be used reliably as the maximum wind speed it can measure is too low in most wind conditions in the area of measurement site. For $f_s \in$ [10Hz;40Hhz], the software can be used reliably, provided the maximum wind speed values are not exceeded. In low wind speed conditions, all sampling frequencies can be used, as there is no other apparent constraints on the software.

5.4.3 Conclusion on the software tests

The different tests of the software provided answers to the questions raised in section 5.4.1. In normal wind conditions, the software will count accurately the number of pulses sent by the DVAs. The maximum usable sampling frequency is 40 Hz, with maximum wind speed restrictions applying between 10 and 40 Hz. In practice, a sampling frequency of 5 Hz will prove sufficient for the analyses to be made on the wind speeds and their correlation to crop motion. The conclusion on the software is that it can be used reliably for the purpose of the wind speed measurements necessary to the present study.

5.5 Conversion from the DVA wind speed readings into a wind velocity vector

The DVAs of a triad give wind speeds in three different directions defined in Figure 5.2 and Table 5.1. With the knowledge of the orientation of the DVAs in the triad reference system, it is possible to retrieve a wind velocity vector.

Let (w_x, w_y, w_z) be the coordinates of the wind velocity vector in the triad coordinate system (x,y,z), and (w_1, w_2, w_3) be the wind speed readings from the 3 DVAs of the triad. Equation (5.7) relates the two coordinates:

$$\begin{pmatrix} w_x \\ w_y \\ w_z \end{pmatrix} = \mathbf{D^{-1}}. \begin{pmatrix} w_1 \\ w_2 \\ w_3 \end{pmatrix} \tag{5.7}$$

Here, **D** is a transformation matrix derived from the direction cosines presented in Table 5.1. The detailed derivation of matrix **D** is presented in Appendix E. The calculation of the wind velocity vector components for each triad of readings is performed numerically with IDL.

5.6 Conclusion

5.6.1 Practical use of the system

A detailed list of the practical use of the wind data measurement system is given in the next chapter, section 6.1.1, where the wind data measurement procedure is given and related to the video data recording. To give a brief overview here, the DVAs are connected to the long cables, themselves connected to the interface box . The interface box is constantly connected to the DVA-PC board, whose outputs are plugged into the PC-30D board. The clock board is also connected to the PC-30D, and all the equipment is powered by the generator.

From the experience gained during the measurements of 2000, it is advised to clearly label each cable so that each DVA channel is easily associated with the correct DVA of a given triad. Before starting the useful measurements, it is worth checking that all DVAs are functioning perfectly. In practice, it is not rare to experience a broken connection or a loose contact along the connection chain. In fact, bad connections are at the origin of the fact that the wind data could not be collected by all four DVA triads at all times during the measurement campaign. The implications of missing some wind data are not dramatic for the purposes of the research, as long as at least one DVA triad is operational during the video data recording.

5.6.2 Building the wind database

The wind data is collected just above canopy height, so a direct comparative analysis of the wheat motion and the wind velocity can show the relation between the two. In addition to this, it is useful to have some measurements of the wind velocity at a higher altitude of about 2 m. A height of 2 metres corresponds to the height at which

the wind speed is recorded by the Automatic Weather Station (AWS) available on the Cranfield airfield. The availability of this independent source of wind data is useful because it will be used to derive some wind statistics throughout the year. By linking it with the wind data recorded at 2 m high, some probabilities of having a certain set of wind conditions at a given time in the year will be derived (see Chapter 6). They will be related to a probability of obtaining a certain coherence value from SAR data.

The wheat motion measurements were made in the growth season 2000 on 6 occasions from May 1^{st} to August 15^{th}. Unfortunately, wind data at 2m is not available for all the measurement dates due to the connection problems mentioned earlier. Details on the completeness of the data sets are given in Chapter 6.

5.6.3 System real-time capabilities and sampling frequency

This chapter presented the anemometry equipment to be used to measure real-time wind velocities in conjunction with crop motion measurements. The system proved to be working correctly, and the artificial steady wind conditions which were electronically simulated enable the assessment of the accuracy of the whole system. Wind velocities up to 12 $m.s^{-1}$ can be recorded accurately in real time at sampling frequencies of 10 Hz or less. At higher sampling frequencies, only low wind conditions can be accurately measured.

It is decided to make the wind data measurements at a sampling frequency of 5 Hz. The first reason for this choice is that it allows all wind conditions to be measured with a good accuracy (only limited by the measurement error of the DVAs themselves). The second reason is that a 5 Hz sampling frequency is a divider of the video sampling frequency (25 Hz), so it facilitates the numerical analysis of the two data sets. Finally the third reason is linked to the anemometer distance constant.

The distance constant is a direct consequence of the inertial properties of vane anemometers. Assuming that the anemometer is at rest at a time t=0 and that a unit step change of air speed (1 $m.s^{-1}$) runs though it, the distance constant is the distance the air travels before the difference between the true airspeed and the measured airspeed is inferior to $1/e m.s^{-1}$. The shorter the distance constant, the faster the anemometer reacts to a change of air speed. For anemometers it is more appropriate to define a distance constant rather than a time constant, since the distance constant is independent of the wind speed. For the MICA vane anemometers used in the measurements here, it is shown in [63] that the distance constant equals approximately 0.3 m. Assuming an average wind speed of 2 $m.s^{-1}$ (low wind conditions), the time after which an independent wind measurement can be made with the anemometer is 0.3/2=0.15s. Using a sampling frequency such that the wind measurements are made at a period shorter than 0.15 s means that the data samples will be correlated, i.e. they are not independent. Therefore a sampling frequency of 5 Hz (period: 0.2 s) is well suited since it provides independent wind data samples for wind speeds of 2 $m.s^{-1}$ or higher. In fact the minimum wind speed at which a 5 Hz sampling frequency provides independent samples is 0.3*5=1.5 $m.s^{-1}$. Such a low wind speed is reached in most cases, under normal meteorological conditions.

Chapter 6

Data acquisition and analysis

This chapter presents the wind and motion data measured in the summer 2000. Section 6.1 presents the acquisition procedure and gives an overview of the data. The methods of analysis introduced in section 6.2 are applied to the wind data in section 6.4 and the motion data in section 6.5, separately. Then section 6.6 focuses on the relation between the two data sets, i.e. on the direct analysis of the effect of the measured wind on the motion of the wheat. Since the analysis will require some preliminary knowledge of the state of the wheat at the different recording dates, section 6.3 gives an overview of the main characteristics of the wheat phenotype throughout the growth season. It will become clear as the analysis progresses in the chapter that the wind at the crop canopy level is turbulent and relates to the wheat motion through various complex processes. Therefore the emphasis here is not placed on the detailed explanation of these processes as an end product, but rather on the characteristics most relevant to the initial problem raised in this report, namely the understanding of the coherence. The concluding section of this chapter (section 6.7) will relate the data presented here to the initial objectives of the research raised in section 2.5.2.

6.1 Presentation of the data set

6.1.1 Data acquisition and recording

This section details the experimental procedures followed to collect the video and wind data. Should similar measurements be repeated in the future, it is intended here to provide as much useful information as possible on the practicalities of the experiment to make it reproducible. It is felt that this is a very important part, as the aim of this report is not only to provide useful data sets and data analysis, but also to communicate the experience acquired during the practical field work. Table 6.1 is a list of all the equipment used for the measurements.

The individual tasks of the measurement procedure are described below.

1. Fix the 3 supporting poles on the ground with the hammer. Note their relative distance. The poles should be oriented so that two of them are aligned perpendicular to the mean wind direction, and the third pole downwind, at about equal distance from the two other poles (see Figure 6.1). If only one

	Description	**Quantity**
Wind data measurement system	Power generator	1
	Computer+Screen	1
	Digital Vane Anemometer (DVA)	12
	Triad mount	4
	Triad mount fixings	8
	Vertical supporting pole	3
	PC-30D Digital/Analogue I/O board	1
	Clock board	1
	DVA-PC board	1
	Set of 3 50 m long 5-way cable	4
	Wind vane 50 m long 5-way cable	1
	Connector box cable	12
	15-pin connector box	1
	5V power supply	1
	Wind vane+LED	1
	Hammer	1
	Multi power socket	1
Motion measurement system	Video camera	2
	Video camera tripod	2
	Camera (flash)	1
	Red label	10
	Glue tube	1
Common	Reference frame	1
	Tape measure (5m)	1
	Watch	1
	Level	1
	Log book+pen	1

Table 6.1: Equipment required for the wind and video data measurements

triad is used instead of the full setup with the 12 DVAs, then it is placed on its vertical pole at about 1m downwind of the targets to measure.

2. Fix the DVA triads on the poles. Two triads are mounted on pole n°1, the bottom one at canopy level (triad 1B) and the top one higher on the pole (triad 1T). The two front triads (2 and 3) are also placed just above canopy level. Note the different heights of each triad. The 3 DVAs of a single triad are numbered as shown on Figure 5.2. The triads are oriented so their main axis (the x axis in Figure 5.2) points in the direction of the mean wind.

3. Fix the wind vane to the top of pole 1, with its south direction facing the wind in order to avoid the 0°-360° jumps in the wind vane readings.

4. Connect the DVAs to the 50 m long 5-way cables and the long cables to the 15-pin connector box. The connections on the box are numbered from 1 to 12

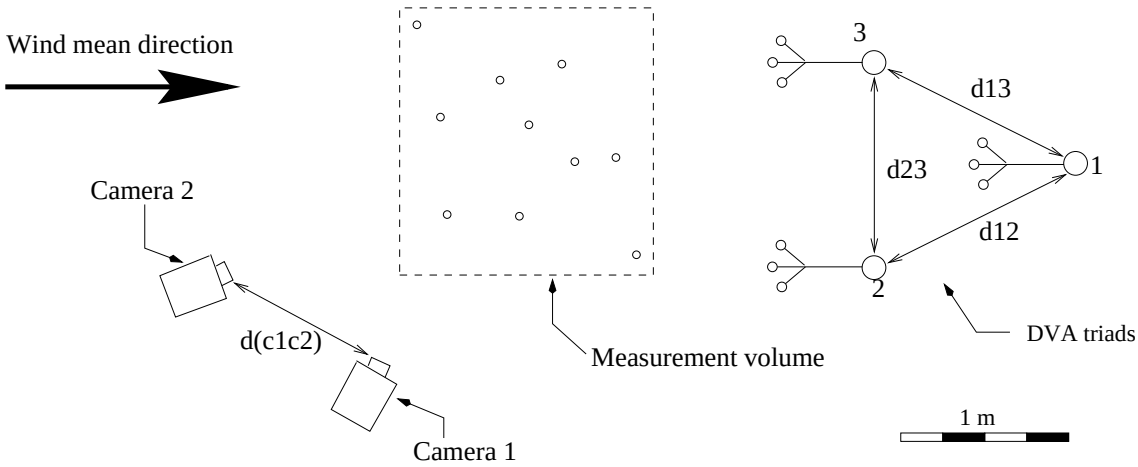

Figure 6.1: Schematics of the experimental setup

and connected to the DVAs according to Table 6.2.

5. Connect the wind vane to the clock board with its 50 m long 5 way cable.

6. Connect the 5V power supply to the clock board alimentation wires.

7. Connect the computer, the screen and the 5V power supply, and start the power generator.

8. Launch the wind data log program for preliminary testing. Check on the screen that all DVA channels function properly, and stop the power generator. It is recommended to keep the wind data collected during this testing phase as it could be of use for future analysis.

9. Glue the red round labels on crop elements. The labels should be spread in an area of about 1 m^2 so they cover the entirety of the field of view of the two cameras. The labels are placed upwind from the triads 2 and 3 (see Figure 6.1). It should be expected that the labels placed on the crop elements will not all be visible for accurate tracking. To limit the importance of this problem, approximately 6 to 8 red labels should be used. Experience shows that half of them or more are visible at all times and can be reliably used for analysis.

10. Place the cameras on their tripods and the tripods in the field. The cameras should point towards the red labels and try to encompass all red targets placed on the crop elements. It should be avoided to place the cameras directly

15-pin box connection	1	2	3	4	5	6	7	8	9	10	11	12
Triad number	1T	1T	1T	1B	1B	1B	2	2	2	3	3	3
DVA number	1	2	3	1	2	3	1	2	3	1	2	3

Table 6.2: Connection convention between the DVAs and the 15-pin connection box. The DVAs are numbered as shown on Figure 5.2

upwind from the triads to avoid contaminating the wind data. The distance between the two cameras is noted $d_{C_1C_2}$. In practice a distance of about 1 m is suitable.

11. Place the LED next to one of the cameras, ready for use.

12. Place the reference frame in the field of view of the cameras, so that one axis (preferably the x axis) is aligned with the x axis of the triads and therefore with the mean wind direction. The y axis should be such that the (x,y) plane is placed horizontally with the help of a level.

13. Record a few seconds of video data with the reference frame in the field of view. Then stop the recording and remove the reference frame. From now on, the video cameras should not be moved at any time in the measurements.

14. Restart the power generator and launch the DVA data log program. Simultaneously, start timing with the watch.

15. Start recording with the two video cameras.

16. Place the LED in the field of view of one of the two cameras to show a single off-on transition of its light. Note the time of this transition from the watch. This is the time synchronisation of the wind data with the video data. The LED starts its 0.25 Hz flashes when the wind data log program is launched and therefore represents the wind data time. Noting the time of a single off-on LED transition recorded by a video camera enables to reference the wind data time with the video sequence.

17. Use the camera flash in front of the two video cameras. This is the time synchronisation of the two video cameras. It is recommended to use the camera flash twice, to make sure it is detected, and also several times during the recording sequence.

18. While the data are being recorded, measure the different relevant distances of the experiment (d_{12}, d_{13}, d_{23}, h_{1B}, h_{1T}, h_2, h_3, h_{crop}, $d_{C_1C_2}$). Check regularly that the wind and video data are being recorded properly.

19. The total recording time of the experiment should be between 20 and 30 minutes. When finished, stop the cameras, stop the wind data log program. Switch off the computer and stop the power generator.

20. Store the video cameras, then the DVA triads. The 3 supporting poles are removed last.

6.1.2 Overview of the data set

The data set is composed of wind data and wheat motion. Table 6.3 presents the recording dates, together with the number of targets tracked in each case, and the availability of the wind data.

Date (Year 2000)	**Video data**		**Wind data**	
	Tracking time	Targets tracked	Recording time	Available triad number
1^{st} May	1 mn	1	Not available	
6^{th} June	1 mn	5	29 mn	1T, 1B, 2, 3
21^{st} June	1 mn	3	33 mn	1T, 3
19^{th} July	1 mn	5	5 mn	3
25^{th} July	1 mn	6	27 mn	3
2^{nd} August	1 mn	8	19 mn	3
15^{th} August	1 mn	8	30 mn	3

Table 6.3: Available video and wind data acquired in 2000

The figures presented in Table 6.3 require a few explanations. Concerning the video data, the total recording time is approximately equivalent to the recording time of the wind data, since the two recordings are performed in parallel. One minute of this video data was extracted, as it corresponds to the 2 Gbyte size limit on the AVI files needed for processing. So there is much more video data available on the tapes which can still be processed and analysed. However, it is a decision made during the research to focus the analysis on these one minute sequences. First, it is more relevant to the project to analyse the simultaneous motion of several targets rather than a single plant for a longer time. The second reason, possibly more constraining, lies in the fact that extracting and processing all the data from a total of about 2h30mn, in sequences of one minute and for several targets, is a task that would be time consuming and would undermine the time required on data analysis. In fact, the project suffers here from the very tight schedule between the measurements and the end of the research. It is an aspect which will be commented again in future sections.

The measurements of May 1^{st} were the first of the series. They correspond to the first use of the cameras in field conditions. No wind data were recorded due to the dysfunctions of the original wind data acquisition board discussed in section 5.3.2, which required the building of the new data acquisition system presented in Chapter 5. The entire system was ready and used on June 6^{th}, for the second data acquisition date. On June 21^{st} and for the subsequent dates, only one or two DVA triads could be used due to bad connections in the cables. Although they were chosen for their robustness, the Binder connectors did not prove to be robust enough. Some of them gave bad contacts or even breakage at the soldering point. Due to time constraints, it was decided to keep one functioning triad to record reliable data that could be trusted for analysis. The early measurements at different points will provide the necessary statistics to relate the wind speeds at different heights and positions. In June, July and August the number of targets successfully tracked depends on the wind speed conditions. In particular, the high wind speeds on June 21^{st} made the tracking difficult, and only 3 targets can be reliably used for analysis. This is due not so much to the fast motion of the targets than to the fact that they were frequently obstructed by wheat leaves or other wheat heads in the image. In fact, the conditions

on June 21^{st} represent a good indication of the limits under which the measurement system can be used.

Measuring reliable wind and motion data proved to be more difficult than could be assumed from the description of the systems given in Chapters 4 and 5. The experience gained this year would certainly be profitable to a more complete campaign in the next growing season. Recommendations based on this experience are given later in this chapter.

6.1.3 Data storage

The video films are still kept on their original Digital 8 tape. It is the most convenient way to store them, as they would require vast amounts of memory if kept on a computer disk. The sequences of interest on the tapes can easily be transferred to a computer. The position of the targets on each of the recording dates is kept in text files which are available on request and also on the CD attached to this report. Appendix F gives details on the format of these files. The wind data are also stored on the attached CD. The entirety of the data is kept as it provides a useful source of measurements for meteorological studies, and also of course for further analysis with the rest of the video data. In addition to information on the format of the wind data files, Appendix F gives the necessary synchronisation information between the video data and the wind data. For the one minute video sequences treated, the line number in the wind data file corresponding to the first line of the target position files allows to reference the two data sets. In order to use the rest of the video data in conjunction with the wind data, Appendix F gives the time t_{LED} at which the LED appears in the video image. The time origin corresponds to the first line in the wind data files, so knowing t_{LED} and the sampling frequency (5 Hz), the two data sets can be cross-referenced.

6.2 Methods of analysis

Before presenting and commenting on the data sets, it is important to introduce here the parameters and definitions used in the remainder of this chapter. The wind and position data will be first analysed separately and then in conjunction with each other. In each case, the three points of analysis concern the study of mean values, of the time variation of the signals, and of their characteristics in the frequency domain. This section presents the relevant definitions related to these three points.

6.2.1 The coordinate systems

The coordinate system associated with the wind measurements is defined in section 5.1.2, and noted here $\mathcal{W}$. It is an orthogonal system with the x axis pointing towards the mean wind direction and the z axis pointing vertically. Finding the mean direction can only be done approximately since it is subject to changes. In practice, it was estimated from the Cranfield airfield windsock near the location of the measurements, and from the wind vane. The vertical axis of the coordinate system is aligned with a level.

The coordinate system associated with the position of the targets on the wheat heads is defined by the reference frame used for calibration (section 4.3), and noted here $\mathcal{P}$. The x axis points to the same direction as the wind x axis, and the z axis is also vertical upwards. In practice the x axis of the reference frame is aligned visually with the main axis of the DVA triad.

Several factors contribute to the non-ideal nature of $\mathcal{W}$ and $\mathcal{P}$. The potential sources of errors in the observational coordinate systems compared to the ideal systems are:

- The DVA triad supporting pole can be tilted with respect to the ideal vertical. The vertical alignment of the pole is checked with a level, and such a method is thought to be accurate within about 5 degrees. Similarly, the vertical alignment of $\mathcal{P}$ is subject to the same accuracy.

- There can be an alignment error of the x axis of $\mathcal{W}$ with respect to the mean wind direction. The alignment method is only accurate within a few degrees, and the mean wind direction can change during the total time of the measurements (20 to 30 minutes).

- Each DVA of a single triad can be rotated compared to its nominal position which defines the direction cosines given in Table 5.1. Since the triad mounts are precisely made, the rotations are only possible within the machine tolerances of the manufacturing process. It is probable that they result only in a very small rotation compared to the ideal position.

- The x axes of the two systems are not exactly parallel since they are only aligned visually. Although careful attention is paid to reduce this error during the calibration, it is probable that the two x axes make an angle of about 5 degrees at most.

The comparison of the wind direction with the direction of wheat motion requires to take into account the alignment error on the x axes of the coordinate systems. The non-verticality of the DVA triad supporting pole is of minor importance since the wind travels mainly horizontally. The rotation of the DVA axis is in principle a serious source of error in the wind velocity vector since it affects the direction cosine matrix and therefore the components of the wind vector. The manufacturing tolerances of the triad mounts are not known so it is assumed that they are small enough and do not affect the quality of the measurements. The calibration results presented in [63] did not detect any discrepancy due to the potential tilt of the DVAs.

No mention was made here of the video camera coordinate systems since they are only intermediate systems introduced to derive the coordinates of the targets in $\mathcal{P}$. They are not used directly for the analysis presented in this chapter.

6.2.2 Parameters derived from mean values

Wind parameters

If u, v, and w denote the 3 components of the instantaneous wind velocity vector along the x, y, and z axes of $\mathcal{W}$ respectively, then the mean and standard deviation have their usual definition and are noted $\bar{u}$, σ_u, $\bar{v}$, σ_v, and $\bar{w}$, σ_w. The mean wind direction η_{wind} is the angle between the mean wind vector projected on the horizontal plane and the wind x axis:

$$\tan(\eta_{wind}) = \frac{\bar{v}}{\bar{u}} \tag{6.1}$$

The wind turbulence is characterised by the turbulence intensities i_u, i_v, and i_w, which are the ratio between the standard deviation of the wind components and the mean longitudinal velocity:

$$i_u = \frac{\sigma_u}{\bar{u}} \qquad i_v = \frac{\sigma_v}{\bar{u}} \qquad i_w = \frac{\sigma_w}{\bar{u}} \tag{6.2}$$

Wheat motion parameters

The horizontal coordinates of the wheat heads (coordinates x and y in the reference system $\mathcal{P}$) define a cloud of points from which a linear regression line can be calculated. The spread of the points around the line is quantified by the correlation coefficient r^2_{xy}, and the angle between the regression line and the x axis defines the mean direction of displacement η_{disp}. The correlation coefficient and the equation of the regression line are calculated from standard procedures in the IDL language. The slope of the regression line is the tangent of η_{disp}.

6.2.3 Time analysis

The variation with time of the wind components and the motion components can be plotted directly, taking into account the two different sampling frequencies of the data sets (5 Hz for the wind data and 25 Hz for the motion data).

The autocorrelation function (ACF), $R_{xx}(\tau)$, is a measure of the relation between the signal x at time t and the same signal at time $t+\tau$. For N data values x_n ($n = 0, 1, 2, \ldots, N-1$), sampled at equally spaced time intervals Δt, the autocorrelation function is calculated at discrete time intervals $r\Delta t$ ($r = 0, 1, 2, \ldots, m$, with $m < N-1$) according to the following definition:

$$R_{xx}(r\Delta t) = \frac{\frac{1}{N-r}\sum_{n=0}^{N-r-1}(x_n - \bar{x})(x_{n+r} - \bar{x})}{\frac{1}{N}\sum_{n=0}^{N-1}(x_n - \bar{x})^2} \tag{6.3}$$

The autocorrelation function is a coefficient between 0 and 1 which quantifies the independence of the data points in the time series. By definition $R_{xx}(0) = 1$. Note that the denominator of Equation (6.3) is the variance σ_x^2 of the signal x.

The cross-correlation function (CCF), $R_{xy}(\tau)$, aims to represent a similar concept, but for two separate data sets. It is a measure of the relation between a signal x at time t and another signal y at time $t+\tau$. With a similar notation as above for the ACF, R_{xy} is defined as follows:

$$R_{xy}(r\Delta t) = \frac{\frac{1}{N-r}\sum_{n=0}^{N-r-1}(x_n-\bar{x})(y_{n+r}-\bar{y})}{\frac{1}{N}\sqrt{\sum_{n=0}^{N-1}(x_n-\bar{x})^2\sum_{n=0}^{N-1}(y_n-\bar{y})^2}} \tag{6.4}$$

In the case of wheat motion, the cross-correlation functions will be useful to indicate the relation between the motion of different wheat heads.

6.2.4 Frequency analysis

The Fourier transform of the autocorrelation function defined in Equation (6.3) gives the normalised power spectrum $S_{xx}(f)$ of a signal x.

$$S_{xx}(f) = \int_{-\infty}^{\infty} R_{xx}(\tau)e^{-j2\pi f\tau}d\tau \tag{6.5}$$

$S_{xx}(f)$ represents the fractional contribution to the total variance from frequencies ranging between f and f+df. The power spectrum $P_x(f)$ is the product of $S_{xx}(f)$ by the signal variance σ_x^2, and the following relation holds:

$$\int_{-\infty}^{+\infty} P_x(f)df = \sigma_x^2 \tag{6.6}$$

$P(f)$ can be viewed as the rate of change with frequency of the mean square value of the signal. So the area under $P_x(f)$ in a frequency band represents the mean square value (the energy) of the signal in that band. It is a representation allowing to easily spot periodic trends in a data set.

In the remainder of this chapter the discrete Fourier transforms of the different signals are calculated with the Fast Fourier Transform (FFT) algorithm available in the IDL language. A Hanning window is used during the calculation in order to suppress the errors inherent to the calculation of discrete Fourier transforms [65].

For graphical representation, the power spectra are multiplied by the frequency f and displayed on a logarithmic frequency scale, so equal areas under the curve represent equal energies.

6.3 Description of the wheat phenotype

The wheat phenotype is the set of its observable characteristics. The type of wheat in use is more precisely called winter wheat, as it is sowed in the winter months. The aim of this section is to give an overview of the different growth stages of the wheat as they were observed in fields around Cranfield. The description of the wheat will help to interpret specific features which will arise later in this chapter and in the next.

Qualitative description of the wheat growth

From past research at Cranfield University, some pictures of several wheat fields were taken at regular time intervals from 1996 to 1998, and the growth of wheat was also observed in the season 2000. From these observations, the following features were observed.

- In November, single leaves emerge from the soil. They are approximately 2 to 3 cm long in mid November, and are about 10 to 15 cm in December, when each plant is composed of 3 to 4 leaves. The field is then structured in rows, which are clearly visible until March or April.
- Very little growth is observed up to March. The soil is subject to changes linked to the weather conditions. Water ponds can be observed in very wet periods and the soil is cracked during the most dry conditions. In March the vegetation density is visibly increasing. There can be significant variability in the dates when this density increase arises, for different years, different fields and even within a single field at different locations.
- The wheat height starts increasing in March/April, and the leaf density is such that the initial row alignment disappears.
- In May the wheat heads emerge from the stalk and the maximum height is reached at the beginning of June, when the heads have completely emerged. Along each wheat stalk, only 3 to 4 leaves remain.
- In June and in the first half of July, the size of the wheat heads is increasing. Both the stalks and the heads remain vertical. The maximum size of the heads is reached in the first half of July.
- The wheat heads start drying from the second half of July. The drying of the leaves starts before that of the heads.
- In August the entire wheat plant is dry and the wheat heads start folding down. Harvest occurs in the second half of August. The wheat grains must contain less than 15% humidity before they can be used for processing. For that reason, small farming exploitations tend to harvest later because they do not place the grains in storage areas for final drying, in order to reduce their operating cost.

It should be noted that the dates given in the description above only concern wheat field typical of the South-East of England. The wheat cycle in more southern parts of Europe is certainly shifted by several weeks towards earlier dates. The wheat phenotype at the different growth stages affects the radar backscatter, and the contributions from the different wheat elements since they have specific variable characteristics in terms of density, moisture content, and orientation. This will be the subject of the next chapter, but it is worth mentioning that the qualitative description given here will be used later to explain the variation of the radar backscatter and of the coherence throughout the year.

Wheat height

Figure 6.2 shows the variation of the wheat height from March to harvest, measured in 1997 in two fields and in 2000 in one field. Heights in the same field (field 1) were measured in the two years. Field 1 is also the field where the wheat motion and wind measurements were made.

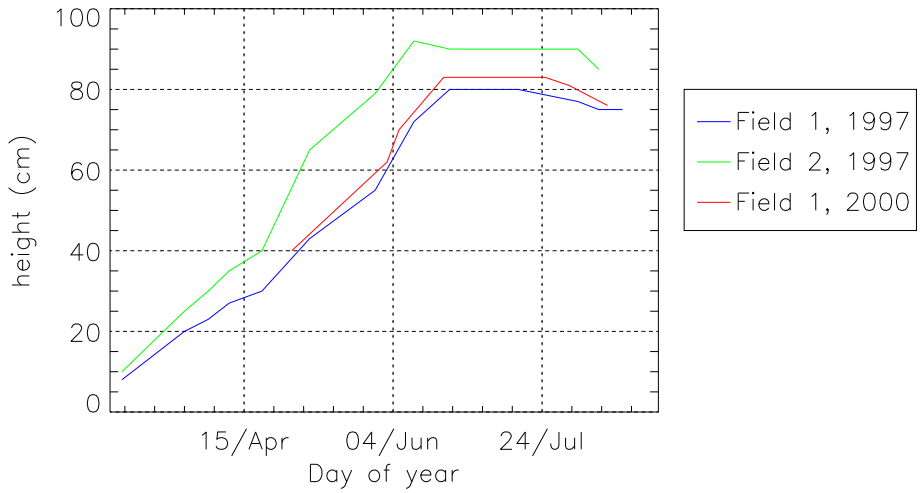

Figure 6.2: Variation of the wheat height with the day of year, in 2 fields in 1997 and one field in 2000

The uncertainty on the height measurements is about 5 cm. The height variations at the two different years in the same field are very comparable. Not only is the difference in the height values inferior to 5 cm at all times, but also the date at which full growth is reached differs only by a few days. The wheat in field 2 is higher than in field 1 and reaches its peak height earlier, about 10 days before. The wheat type in both fields is similar so the difference can only be explained by differences in soil properties or farming practice (irrigation, fertilisation). In any case, Figure 6.2 illustrates the fact that similar crops in different fields can have significantly different properties at a given date, especially during the growth period (March/April). The slight height decrease just before harvest is due to the folding of the wheat heads.

It should be noted that the wheat height values published in [66] for an agricultural area in Belgium, 1996, are similar to those of field 1. The values published in [13] concern a wheat field in the Netherlands in 1993 and are close to those of field 2. This seems to demonstrate that the conclusions to be made in this report from the measurements taken at Cranfield can be generalised to wheat fields in Northwest Europe.

Relevance to the understanding of the coherence

The description of the wheat growth given here is relevant to the understanding of the coherence in several respects. Although the influence of the growth state of the wheat on the coherence will be discussed in the next chapter, it is interesting to emphasise here several points. First, the variability in the wheat phenotype in different fields should translate into a variability in the observed coherence, and will

have implications for its potential to reliably classify wheat fields. Secondly, the wheat growth in two different years in the same field is similar, so it will be possible in Chapter 7 to compare coherence observations and simulations even though they originate from data collected at different dates, but from the same field. Finally, the descriptions presented in this section, even if they remain qualitative, will be useful when the variation of coherence with time is interpreted.

6.4 Wind data analysis

This section is divided in four parts: the presentation of average wind values from the different recording dates, the study of the variation with time of the wind velocity, the analysis in the frequency domain, and the comparison with standard wind conditions from the Cranfield automatic weather station. This section and the next do not attempt to relate the wind and motion data sets, as this will be the subject of section 6.6. The aim here is to present the characteristics of the turbulent wind at canopy level, and to relate these characteristics to standard wind conditions throughout the season.

It is beyond the scope of the research to present and analyse a full set of the turbulence characteristics of the wind above vegetation canopies, as this is a very complex subject deserving in itself years of dedicated research. It is however necessary to present the basic features of the turbulent wind as they are related to the underlying vegetation and consequently affect its motion. It is also valuable to check that the characteristics of the turbulence measured here are compatible with those of previously published works, to simply perform a quality check of the data.

6.4.1 Analysis of averages

Table 6.4 to 6.6 give the mean wind speed $\overline{w_t}$, the mean wind direction η_t, and the turbulence intensities $(i_{u_t}, i_{v_t}, i_{w_t})$ obtained from each triad (subscript t). The wind velocities are expressed in $m.s^{-1}$. The wind angles, in degrees, correspond to angle between the mean wind direction and the x axis of the DVA triads. According to the definition of Equation (6.2), the turbulence intensities are dimensionless. The values given here are calculated from the entire wind data measurements and not simply from the one minute corresponding to the motion data.

Mean values at canopy height

The mean wind speed at canopy height varies approximately between 0.5 $m.s^{-1}$ and 3 $m.s^{-1}$. These values are fairly low because they corresponds to measurements close to the surface. The DVA triads being oriented in the mean wind direction, it is expected that the wind angles η_t should have values close to 0°. The values obtained can differ from the 0° direction by as much as about 30°, showing that the wind can change of direction significantly during the 20 to 30 minutes of data collection. The calibration of the DVA triads presented in [63] shows that the error in the measurement of an incoming wind inclined by 30° with respect to the triad x axis is about 3%, both for the wind speed and the wind angle. This level of error

$\overline{w_{1T}}$ $(m.s^{-1})$	η_{1T} $(^\circ)$	$i_{u_{1T}}$	$i_{v_{1T}}$	$i_{w_{1T}}$
3.83	-9.9	0.30	0.28	0.19
$\overline{w_{1B}}$ $(m.s^{-1})$	η_{1B} $(^\circ)$	$i_{u_{1B}}$	$i_{v_{1B}}$	$i_{w_{1B}}$
1.98	2.6	0.36	0.36	0.22
$\overline{w_2}$ $(m.s^{-1})$	η_2 $(^\circ)$	i_{u_2}	i_{v_2}	i_{w_2}
1.94	-19.3	0.33	0.26	0.25
$\overline{w_3}$ $(m.s^{-1})$	η_3 $(^\circ)$	i_{u_3}	i_{v_3}	i_{w_3}
2.31	-12.0	0.35	0.35	0.48

Table 6.4: Average wind speed, wind direction, and turbulence intensities measured on June 6^{th} 2000 by the 4 DVA triads in the wheat field

$\overline{w_{1T}}$ $(m.s^{-1})$	η_{1T} $(^\circ)$	$i_{u_{1T}}$	$i_{v_{1T}}$	$i_{w_{1T}}$
5.30	15.0	0.30	0.29	0.14
$\overline{w_3}$ $(m.s^{-1})$	η_3 $(^\circ)$	i_{u_3}	i_{v_3}	i_{w_3}
2.95	11.2	0.41	0.40	0.18

Table 6.5: Average wind speed, wind direction, and turbulence intensities measured on June 21^{th} 2000 by triads 3 and 1T in the wheat field

is acceptable since it is inferior to the error limit set for the data logging software limits of use (5%, see section 5.4.2).

With the exception of July 25^{th}, the turbulence intensities at canopy height given in Table 6.6 have a value of about 0.4 for i_u and i_v. In [45], the values of i_u measured just above a wheat canopy are also equal to about 0.4, which indicates that the data measured during the project can be used with confidence. The high values obtained on July 25^{th} may be due to the fact that they correspond to very low wind speed conditions. In such conditions, even very light wind gusts would tend to increase the standard deviations of the velocity components in the x and y directions, and consequently increase the turbulence intensity. The vertical turbulence intensity i_w is more variable than i_u and i_v, between the different dates. Except on June 6^{th}, i_w is inferior to i_u and i_v, as it is also observed from the values presented in [45]. However, the higher value of i_w on June 6^{th} does not fit in that pattern. A possible explanation may be related to the fact that the measurement height on June 6^{th} is lower than for subsequent dates since the wheat is not yet at its full growth stage. At lower height there may be a stronger coupling with the surface which translates into more pronounced vertical fluctuations. However, this point cannot be further proved because of the lack of data at lower heights in other cases.

	$\overline{w_3}$ $(m.s^{-1})$	η_3 $(^\circ)$	i_{u_3}	i_{v_3}	i_{w_3}
June 6^{th}	2.31	-12.1	0.35	0.35	0.48
June 21^{st}	2.95	11.2	0.41	0.40	0.18
July 19^{th}	2.23	-33.0	0.44	0.47	0.36
July 25^{th}	0.55	-11.3	0.60	0.76	0.37
August 2^{nd}	2.60	8.6	0.44	0.39	0.26
August 15^{th}	1.99	-21.0	0.47	0.41	0.25

Table 6.6: Average wind speed, wind direction, and turbulence intensities measured by triads 3 at all recording dates in summer 2000

Variability of the wind data from triads at the same height

The wind averages presented in Table 6.4 are useful to assess the consistency of the data measured at approximately the same height by different triads. The mean wind speeds from triads 1B and 2 are approximately identical, but $\overline{w_3}$ is higher than $\overline{w_{1B}}$ and $\overline{w_2}$ by about 15%. The wind angles from the 3 low triads are also significantly different from each other, by a maximum of about 20°. The difference in mean wind direction may be due to alignment errors of the several triads. Another possible effect is linked to the fact that the measurements on June 6^{th} were made close to the edge of the wheat field ($\approx$ 2 m), and consequently the wind measurements by different triads may be subject to a significant spatial variation. In order to avoid this potential source of wind variability, subsequent measurements were made further away from the field edge (5 to 10 m). The wind turbulence intensities are consistent with those discussed above, but again the value of i_v from triad 2 is significantly different from i_{v_2} and $i_{v_{1B}}$.

The variability of the wind patterns means that the wind measured by the triads and the wind which acts directly on the tracked wheat heads about 1 m away from the triads can be different. This conclusion should be kept in mind during the analysis of the relationship between the motion and wind measurements. It will be further emphasised in the next section, when the autocorrelation analysis is presented.

A precise study of the structure of the wind field above the wheat is a potential area of further study, as it would give an idea of the spatial pattern of the wind velocity field. It would require a series of triads at several heights, covering a ground area dependent on the scale of interest.

Variation of the wind velocity with height

On June 6^{th} and June 21^{st}, the wind velocity was measured both at canopy height and higher. Tables 6.4 and 6.5 give the corresponding averages values. Figure 6.3 shows the height profile of the average wind speed from a triad, divided by the wind speed measured from the triad 1T. Normalising the wind speed by the value at the greater height allows to plot on the same graphs the data points from the two different dates.

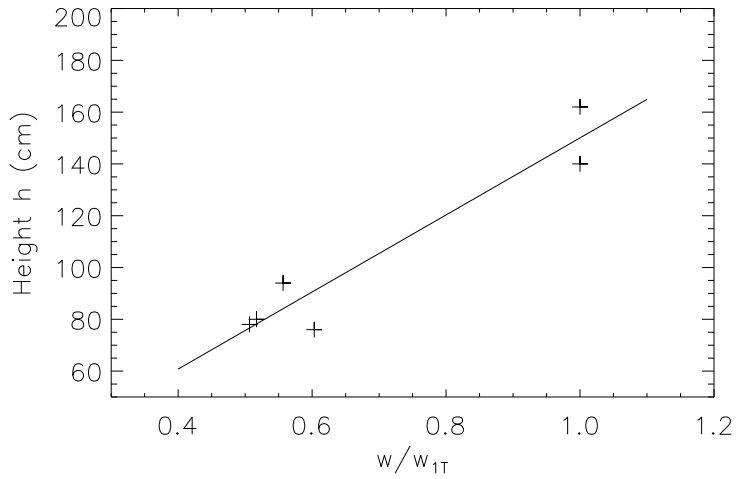

Figure 6.3: Normalised mean wind speed vs. height above ground, obtained from wind data measured on June 6^{th} and June 21^{st} 2000

There are not enough points on the graph for w/w_{1T} between 0.6 and 1 to be certain that the true wind profile can be approximated by the regression line plotted in Figure 6.3. However, results presented in [45] suggest a linear approximation is valid for heights of at most 2 m. The linear regression can be used to relate the wind speed at 2 heights. For that purpose, the equation of the regression line shown in Figure 6.3 is:

$$h[cm] = a\frac{w}{w_{1T}} + b \qquad \begin{array}{ll} a = 148.8 & [cm] \\ b = 1.3 & [cm] \end{array} \tag{6.7}$$

So the wind speed w_1 at height h_1 is related to another wind speed w_2 at height h_2 by:

$$w_1 = \frac{h_1 - b}{h_2 - b} w_2 \tag{6.8}$$

This relation is only an approximation valid for height ranging from 0.8 m (the wheat height) to about 2 m. The wind profile inside the canopy is not assumed to follow the same pattern, and above 2 m it will show an asymptotic behaviour.

6.4.2 Analysis in the time domain

The time traces

Figure 6.4 is an example of the time variation of the three components of the wind velocity vector and of the associated total wind speed. The time traces displayed are obtained from data collected on July 19^{th}. One minute of wind data is displayed on the graphs, corresponding to the one minute video sequence to be discussed later.

The longitudinal component w_{3x} is always positive because the triad points towards the mean wind direction. It also dominates the total wind speed, which explains why the patterns of Figure 6.4(a) and 6.4(d) are similar, both in shape and

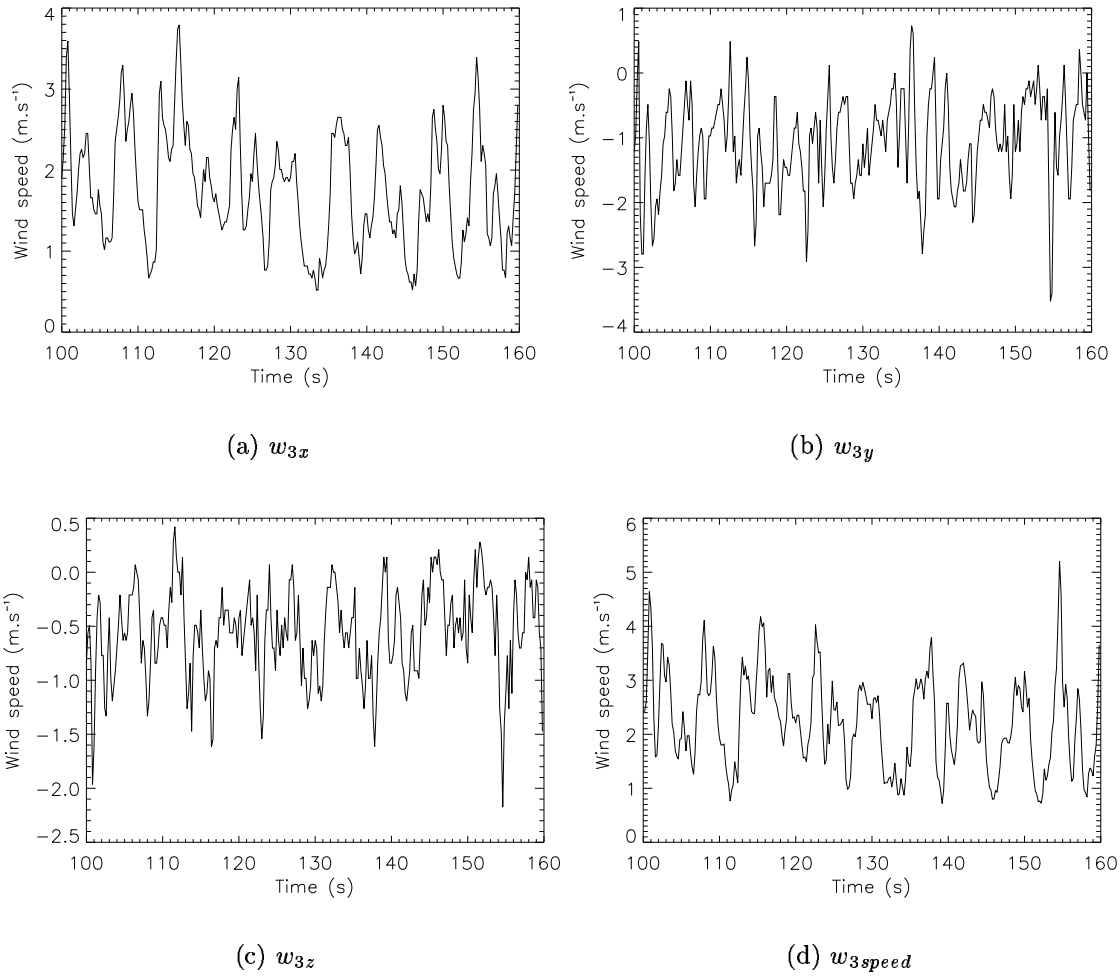

Figure 6.4: Time variation of the wind velocity components and total speed obtained from one minute of data collected on July 19^{th} 2000 just above the wheat canopy (time origin is at the start of the measurements)

amplitude. The two other components w_{3y} and w_{3z} can take both positive and negative values depending on the wind direction. Their variation does not clearly relate to the variation of the wind speed, showing their minor contribution compared to w_{3x}. The amplitude of w_{3z} is the smallest of the 3 components, which confirms that the air flow is mainly displaced horizontally. It should be noted however that the vertical component of the wind is not negligible, as for example at time $t \approx 154s$ on Figure 6.4(c), showing a significant negative spike.

The contribution of the vertical component is shown in Figure 6.5 at two different heights (triads 1T and 3), from data collected on June 6^{th}, together with time traces of the longitudinal components at these two heights. The longitudinal wind speed at greater height is more important than just above the canopy, as expected and shown with the time averages of section 6.4.1. But the interesting point is to note that the vertical wind component covers an amplitude range of about 5 $m.s^{-1}$ at canopy level (triad 3) and only 4 $m.s^{-1}$ at the height of triad 1T , even though at this height the total wind speed is higher. In other words, there is an increase,

with decreasing height, of the vertical wind component relative to the total wind speed. This is an indirect indicator of the interactions between the wind and the wheat, and that the presence of the vegetation canopy tends to increase the vertical component of the wind.

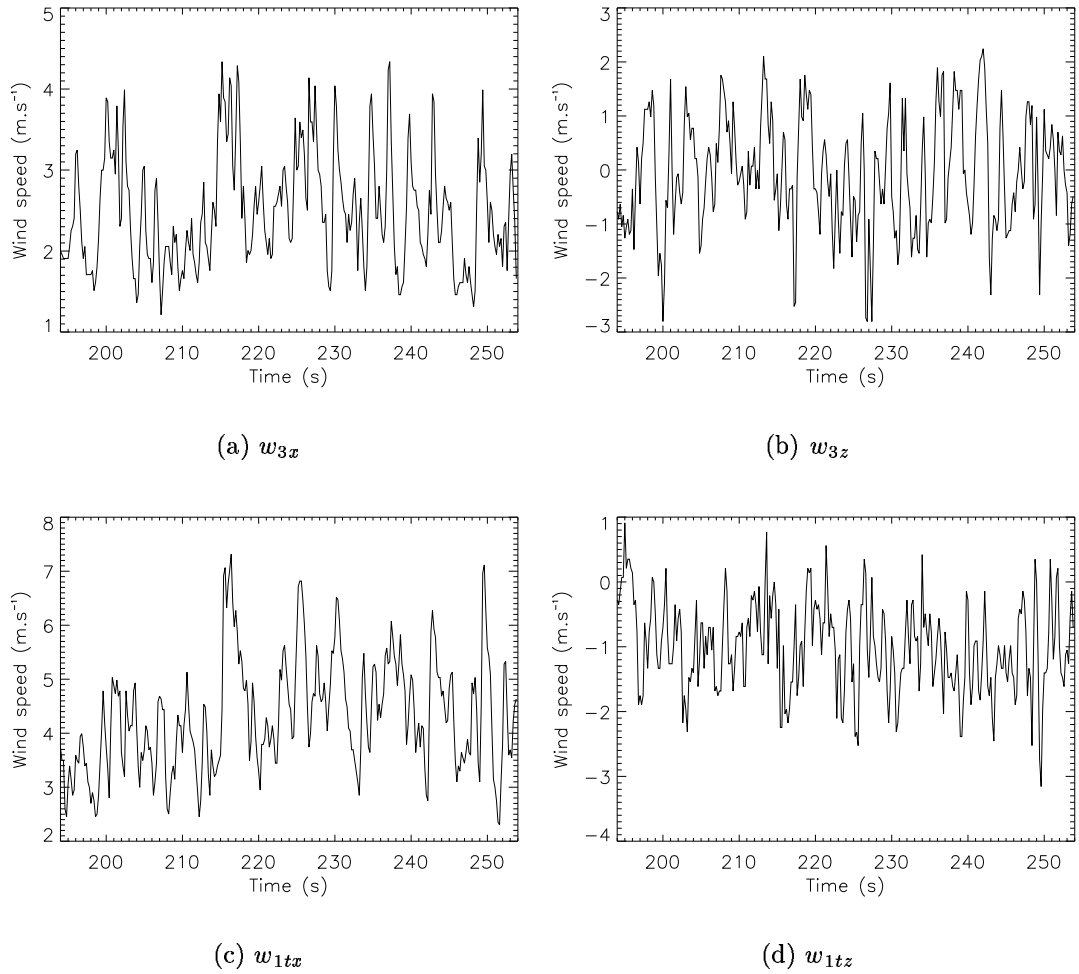

(a) w_{3x} (b) w_{3z}

(c) w_{1tx} (d) w_{1tz}

Figure 6.5: Time variation of the longitudinal and vertical wind components at two different heights, obtained from one minute of data collected by triads 3 and 1T on June 6^{th} 2000 (time origin is at the start of the measurements)

Figures 6.4 and 6.5 show that the time variation of the wind velocity is characterised by the presence of gusts. These gusts are sudden changes in the wind velocity from low to high values. They last between 1 and 5 seconds approximately, and their intensity is related to the wind conditions at the recording date. Direct comparison of the frequency of these gusts in the one minute time span displayed is possible from Figures 6.4(a) and 6.5(a). The frequency of gusts on June 6^{th} is visibly higher than on July 19^{th}, when the mean wind speed is lower. In fact, this is a trend which is common to all wind traces obtained from the different dates: the gust frequency increases with increasing mean wind speed. To illustrate this, Figure 6.6 shows the time trace of w_{3x} obtained in the low conditions of July 25^{th} (Figure 6.6(a)) and in the high wind conditions of June 21^{st} (Figure 6.6(b)). The

gust frequency has a direct effect on the motion of the wheat.

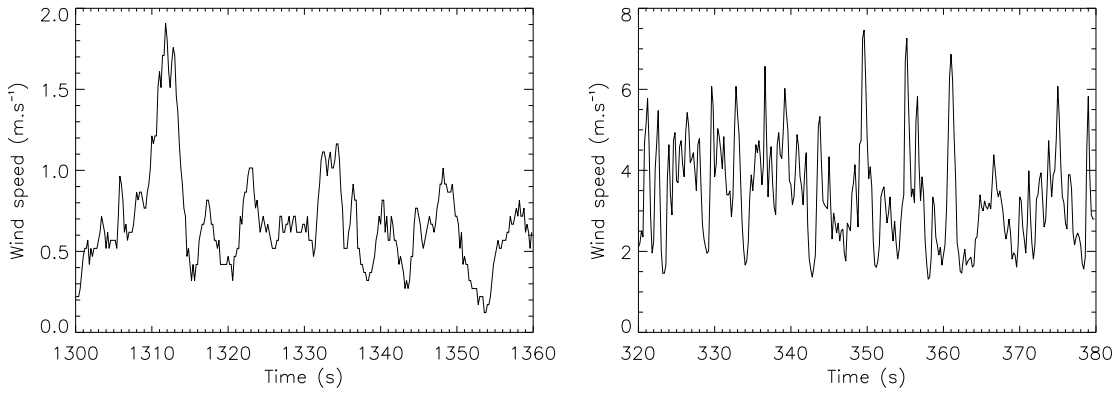

(a) w_{3x}, 25^{th} July

(b) w_{3x}, 21^{st} June

Figure 6.6: Time variation of the wind longitudinal component obtained from one minute of data collected just above the wheat canopy by triad 3 on July 25^{th} and June 21^{st} 2000, illustrating the difference in the gust frequency in low and high wind conditions (time origin is at the start of the measurements for each date)

Autocorrelation analysis

Figure 6.7 shows the autocorrelation functions obtained from the 3 wind velocity components and the total wind speed on June 6^{th}.

The general shape of the curves suggests that the autocorrelation functions can be approximated by an exponential function for a time lag inferior to a few seconds. So the correlation time is defined here as the time when the autocorrelation function reaches the value $1/e$. This correlation time t_c can be viewed as the time during which the wind measured by the DVA triad belongs to the same gust or, more precisely, to the same instantaneous wind pattern. Table 6.7 shows the average correlation time $\overline{t_c}$ obtained with the wind data collected at all dates, as well as the associated standard deviation σ_{t_c}. The value of $\overline{t_c}$ and σ_{t_c} is given independently for the 3 wind components and the total wind speed.

	w_x	w_y	w_z	w_{speed}
$\overline{t_c}$ (s)	1.12	0.72	0.56	0.96
σ_{t_c} (s)	0.17	0.07	0.03	0.15

Table 6.7: Average correlation time $\overline{t_c}$ and its standard deviation for the 3 wind velocity components and the wind speed, obtained from all wind data at canopy height recorded in summer 2000

Two factors influence the correlation time. First the inertial properties of the Mica vanes of the anemometers induce a correlation between readings at different times. These inertial properties are summarised in the distant constant introduced

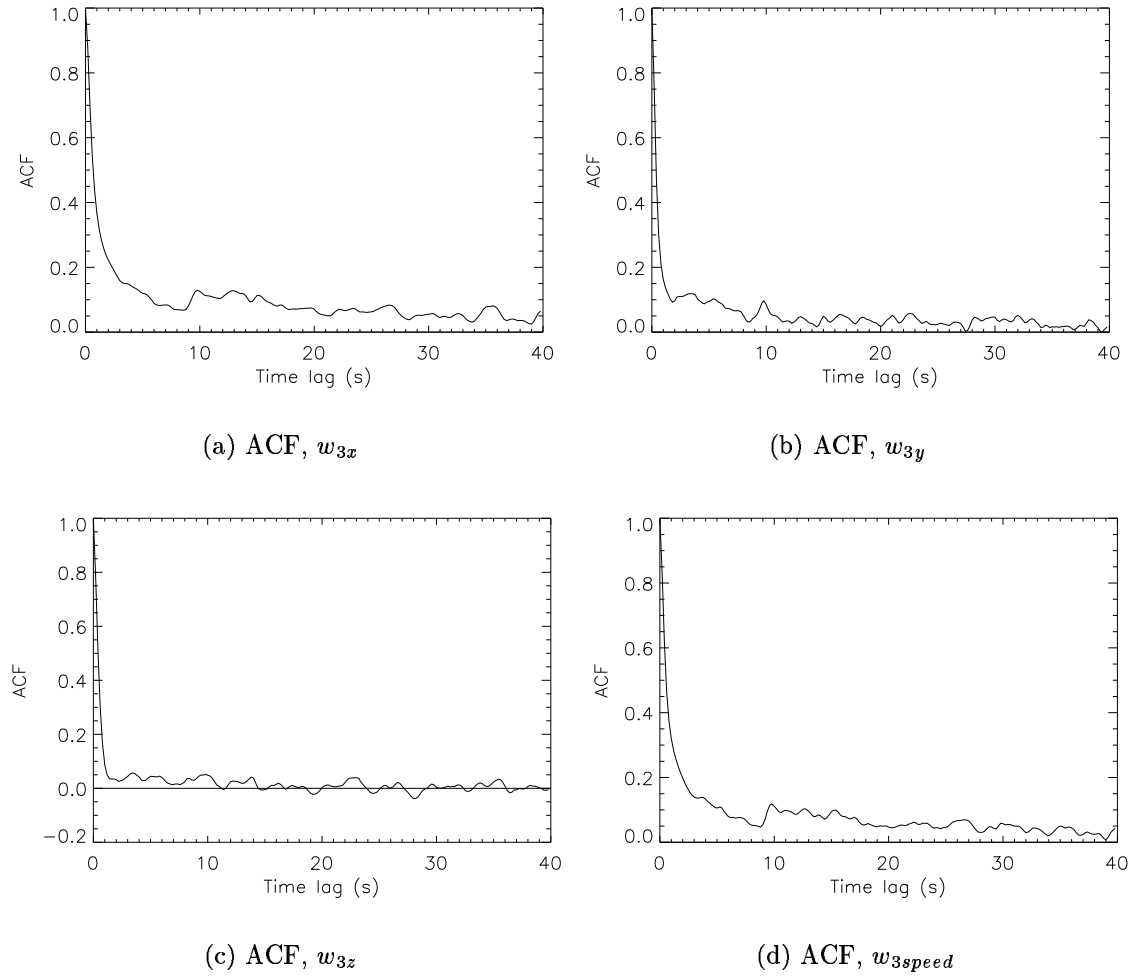

(a) ACF, w_{3x}

(b) ACF, w_{3y}

(c) ACF, w_{3z}

(d) ACF, w_{3speed}

Figure 6.7: Autocorrelation functions (ACF) of the wind velocity components and of the total wind speed obtained at wheat canopy height by triad 3 on June 6^{th} 2000

in section 5.6.3, where it was shown that wind readings are not independent when the run of air through the anemometer during one sampling interval is inferior to that distant constant. The minimum wind speed required to obtain independent reading at a 5Hz sampling frequency was calculated to be about 1.5 $m.s^{-1}$. Table 6.6 shows that the average wind speeds at the recording dates are above that limit, except in the very low wind case of July 25^{th}. In the more frequent case when the DVA readings are independent, correlation in the wind components and speed is directly related to the wind properties. Table 6.7 shows that the correlation time of the longitudinal wind component is higher than that of the two other components. Indeed the fluctuations of the wind shown in Figure 6.4 are more rapid for w_{3y} and w_{3z} than for w_{3x}. For that reason, and also because the main wind component is along the x axis of the DVA triads, the analysis below focuses on the longitudinal wind component.

The time traces of Figures 6.4 to 6.6 tend to show that a single gust of wind in high wind conditions spans over a shorter period than in lower wind conditions. This is proved by Figure 6.8, which shows the correlation time on the wind longitudinal

component as a function of the wind speed obtained from all recording dates in summer 2000, and from triad 3 (wheat canopy height).

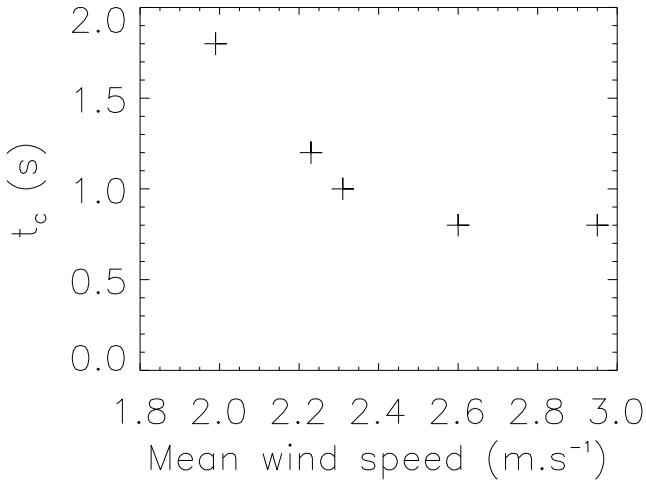

Figure 6.8: Correlation time t_c of the wind longitudinal component vs. mean wind speed $\overline{w}$, obtained from wind data collected in summer 2000 at wheat canopy height by triad 3

Figure 6.8 shows that the correlation time decreases with increasing mean wind speed. From the graph, there is an indication that the correlation takes an asymptotic value of 0.8 s when the average wind speed is superior to about 2.5 $m.s^{-1}$ (just above the canopy level). However, there are not enough data points on Figure 6.8 to make a definite judgement on this point.

Cross-correlation analysis

The cross-correlation between data sets from different triads can show the relation between wind events taken at locations separated by about 1 m. Four triads were available on June 6^{th}, so the analysis below focuses on this particular data set. The exact distance between the triads are in Appendix F, Table F.4. Figure 6.9 shows the cross correlation functions between the longitudinal components recorded by the four DVA triads on June 6^{th}.

The highest correlation is found with triads 1T and 1B. These are the two triads mounted on the same vertical pole, so the good correlation at time $t = 0$ means that similar wind events occur at their two different heights. However, the wind measured at the same height (canopy level) but at different locations in the field do not show a very high correlation, at the exception of the cross-correlation between w_{3x} and w_{1Bx}. In this particular case, the peak correlation is about 0.65, and occurs after a time lag of about 1 s. Indeed, if a correlation exists between wind components measured at different locations, it is expected to be after a certain time representing the time required by the coherent gust of air to move from one triad to the other. However, the result of Figure 6.9(c) is not confirmed in Figures 6.9(b) or 6.9(d). This means that the wind patterns at distance of at least 1 m are fairly independent. They are not totally independent, otherwise the cross-correlation functions would be consistently

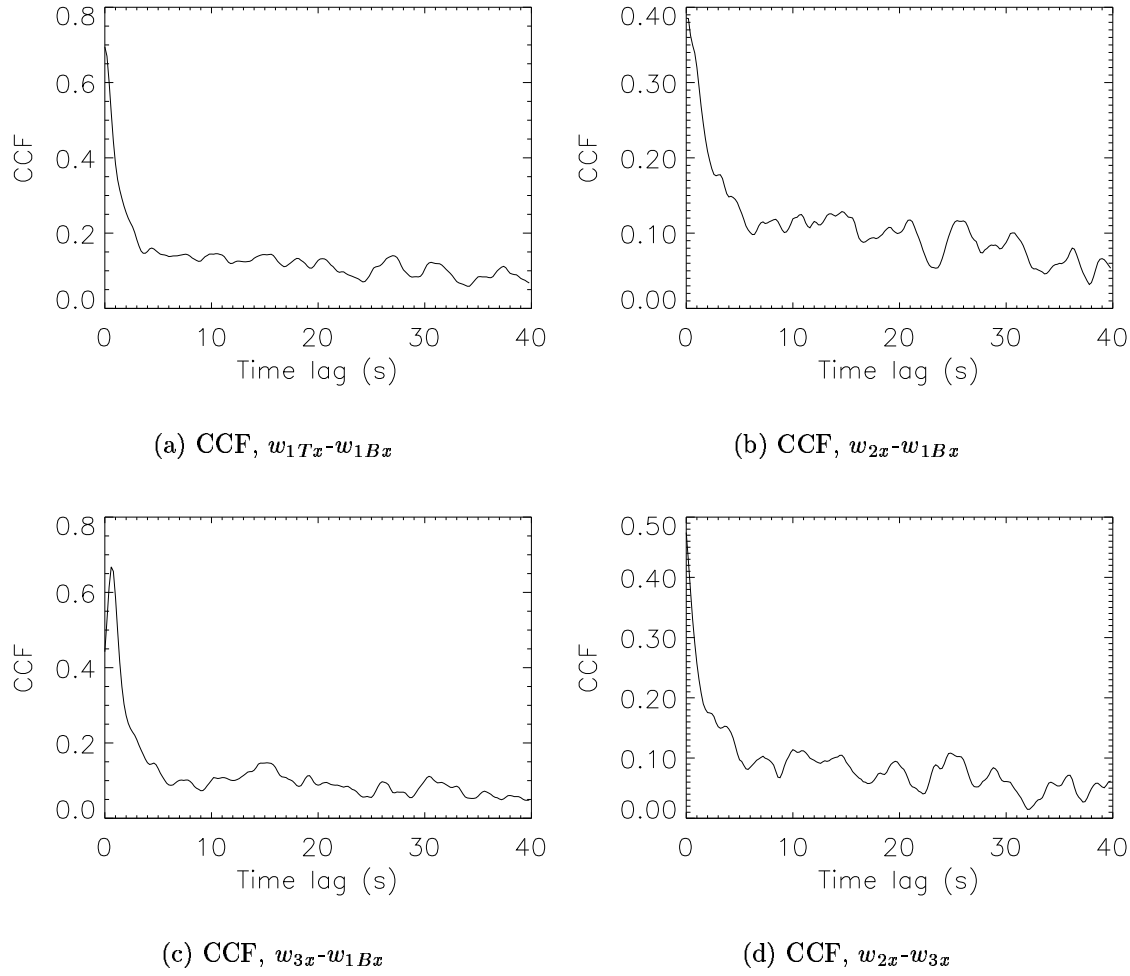

(a) CCF, w_{1Tx}-w_{1Bx}

(b) CCF, w_{2x}-w_{1Bx}

(c) CCF, w_{3x}-w_{1Bx}

(d) CCF, w_{2x}-w_{3x}

Figure 6.9: Cross correlation functions (CCF) between the longitudinal components of the wind recorded by the four DVA triads on June 6^{th} 2000

low. Figure 6.9 suggests that the correlation time between the longitudinal wind components recorded at different triads is of the order of 1 s.

Assuming that there is a distance of 1 m between a DVA triad recording data at canopy height and the tracked wheat elements, then an airflow moving at a speed w_x at the wheat targets takes a time $1/w_x$ to reach the DVA triad. If the time $1/w_x$ is superior to the correlation time, then the wind measured at the DVA triad carries no information about the wind responsible for the motion of the tracked targets 1 m away from the triad in the upwind direction. Assuming a correlation time of 1 s, the minimum wind speed required in order to be able to see a relation between the wheat motion and wind data sets is 1 $m.s^{-1}$. This value is met on average in the wind conditions recorded in summer 2000 (see Table 6.6), but the instantaneous wind speed can take lower values than the average. For low wind speeds, it can be expected that $1/w$ will occasionally be higher than the correlation time and no direct relation will be found between the wheat motion and the measured wind.

The conclusion here is that the wheat motion and the wind data are not expected to be related at all times. In particular, during periods of low wind, a direct

comparison of the wind data with the motion data will not necessarily show similar variations. It is important to be aware of this point when the joint analysis of the wind and the wheat motion is presented. In addition to this, the reasoning above only considered air displacements in the longitudinal direction, but it is likely that the y and z components of the wind will contribute to reduce further the decorrelation time, reducing in turn the strength of the motion/wind relationships. The implication is that the relations between the measured wheat motion and the wind data will be based on average values rather than instantaneous, detailed, time variations.

6.4.3 Analysis in the frequency domain

The two aspects of interest in the study in the frequency domain are to verify that the general shape of the wind power spectrum is characteristic of turbulent wind, and to see if the interaction between the wind and the wheat canopy are detectable from the power spectra. As in the previous analysis, the aim is to gain confidence that the measurements do correspond to real phenomena, and to get a more precise idea about the strength of the relationships between the wind and the wheat canopy.

Power spectrum of the longitudinal wind component

Since it is not the purpose of this chapter to report in detail the turbulence characteristics of the wind, only an example of the power spectra obtained from the wind data is presented here. Figure 6.10 shows the power spectrum of the longitudinal component of the wind measured by triad 3 on August 15^{th}.

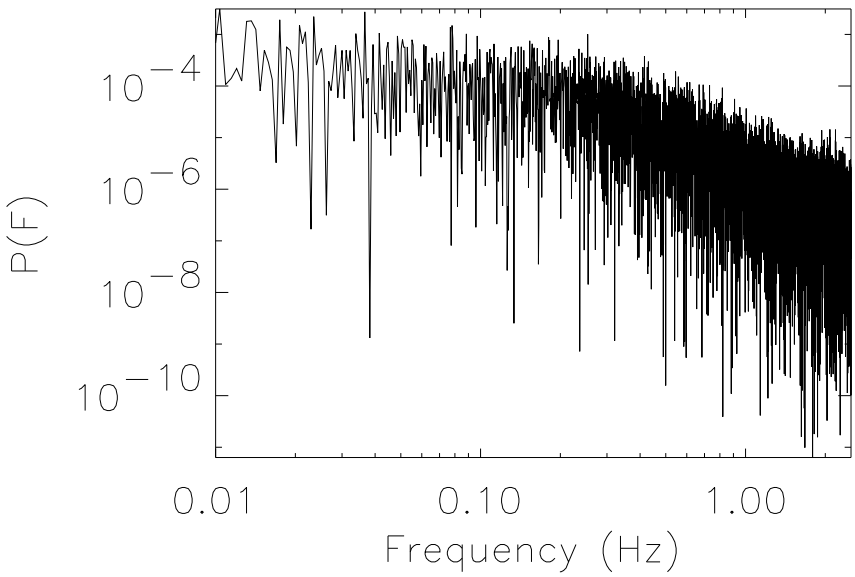

Figure 6.10: Power spectrum of the longitudinal component of the wind velocity, measured at wheat canopy level by triad 3 on August 15^{th} 2000 (corresponding measured mean wind speed: 2 $m.s^{-1}$)

Comparison of the general pattern of the spectrum with published results shows good agreement. In particular, the quasi-linear decrease, on a log-log scale, from

frequencies of about 0.2 Hz is identified in [42] as typical of small scale turbulence. This example indicates that the wind data measured for the purpose of the research comply with previous studies dedicated more specifically to the study of turbulence above and within vegetation canopies.

Effect of the vegetation canopy on the wind power spectra

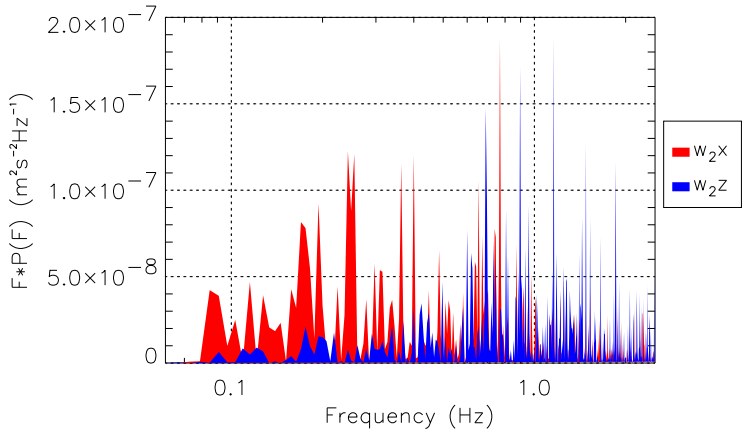

(a) Triad 2

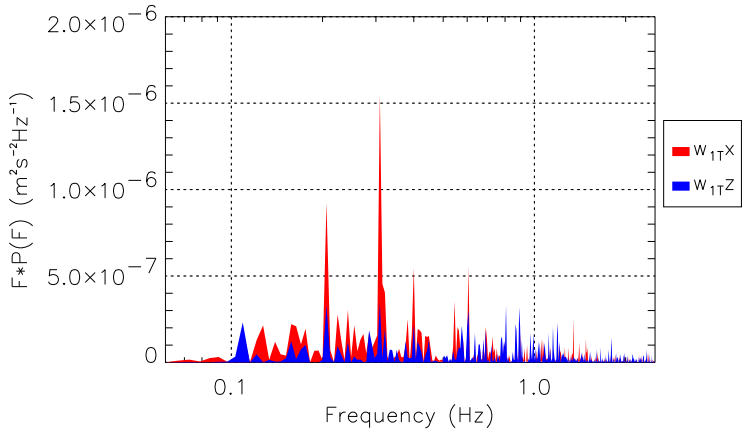

(b) Triad 1T

Figure 6.11: Power spectra from triads 2 (wheat canopy height) and 1T (0.6 m above the canopy) obtained on June 6^{th} 2000, Cranfield. Data recorded over a period of 30 mn, average wind speed is 1.9 $m.s^{-1}$ at wheat canopy height and 3.8 $m.s^{-1}$ 0.6 m above the canopy

The power spectra $P(f)$ displayed on Figure 6.11 are obtained from the longitudinal and vertical components of the wind measured by triads 2 (wheat canopy height) and 1T (0.6 m above the canopy) on June 6^{th}. The frequency axis is on a logarithmic scale, so with $fP(f)$ on the y axis, equal areas under the curves represent equal amounts of energy. It is for that reason that the area under each curve

is also highlighted, in order to see the dominant processes in each spectrum. The power spectrum of the wind component w is noted P_w in the discussion below.

The lower frequency peaks of the spectra are associated with the frequency of gusts for the recording periods. Since these gusts arrive at the triads in a nearly random manner, it is not possible to isolate a single gust frequency but the power spectra can certainly help to identify the dominant frequencies.

The data from the lowest triads are expected to be representative of the local interactions between the crop and the wind. For that reason it can be expected that these interactions have an effect on the power spectrum of the wind measured at wheat canopy height. Although the relationships between the wheat and the wind will be detailed later in this chapter, it is relevant to note here that the motion of wheat is characterised by frequencies centred around approximately 1 Hz. For that reason, the peaks in the wind spectra at these frequencies can be due to interactions with the canopy.

To illustrate this point, Figure 6.11(a) shows that the dominant peaks of $P_{w_{2x}}$ occur at lower frequencies characteristics of the wind gusts, whereas the peaks of $P_{w_{2z}}$ occur at higher frequencies centred around 1 Hz. It is probable that these high frequency peaks are related to interactions with the canopy, since they are expected to affect more significantly the vertical wind component [45]. The fact that the wheat affects the vertical component of the wind above the canopy is indirectly shown in Figure 6.11(b): the distinction between the power spectra of w_{1Tx} and w_{1Tz} is not as clear as in Figure 6.11(a), and the peaks of $P_{w_{1Tz}}$ are not stronger at frequencies centred around 1 Hz. The strength of the wind/canopy interactions being expected decrease with height, the difference in the characteristics of the wind power spectra at canopy height (triad 2) and 0.6 m above the canopy (triad 1T) reflect the role of the wheat in the modification of the wind characteristics. The waving plants act on the vertical wind component more than on its longitudinal component.

Although the discussion above shows that the wind at canopy level is directly affected by the motion of the underlying crop, it is difficult to use the information contained in the power spectra to quantify these interaction processes. For this reason, a more detailed analysis is not presented here, as it does not directly relate to the objectives of the research. The conclusion to draw from the analysis in the frequency domain is that not only does the wind have a direct effect on the motion of the wheat, but also the motion of wheat affects the wind in return. Saying more than that at this stage would require dedicated research on turbulence which does not fall into the main purposes of this report.

6.4.4 Wind data from the weather station

The Automatic Weather Station (AWS) available at Cranfield University records meteorological parameters since 1996. In addition to the wind speed, which is the parameter of prime interest here, the AWS records air temperature and pressure, rainfall, solar radiation and net radiation (difference between incoming and outgoing irradiance). The AWS contains a programmable data logger including a memory card on which the data are stored. Among the capabilities of the data logger, the

sampling frequency can be chosen. The data presented here were collected in 1996 and 1997 every 5 minutes. The height of the wind speed sensor (cup anemometer) is 1.85 m.

With the AWS data, wind statistics are generated for the entire year, at a particular season of the year, or at a particular time of the day. These statistics are later related to wheat motion statistics and for that reason the emphasis is placed here on the summer months, during the wheat growth. However, a brief overview of the wind speed throughout the year is first presented. From the wind speed data, it is possible to generate histograms showing the number of times that a given wind speed is measured. In this section, these histograms are used to plot cumulative probabilities. For a given point wind speed w, the cumulative probability $P_c(w)$ represents the probability that the wind speed in the entire population is inferior or equal to w. Using cumulative probabilities rather than probability density functions allows an easier visual interpretation of several curves on the same graph.

Yearly wind statistics and seasonal variations

Figures 6.12(a) and 6.12(b) show the cumulative probability of the wind speed calculated from all wind speed data points in the years 1996 and 1997. Figure 6.12(c) and 6.12(d) use data from 1996 and 1997 to show the difference between summer and winter winds: data from January, February and March are used to plot the winter curve, and the summer plot is based on winds recorded in June, July and August.

Figures 6.12(a) and 6.12(b) show that the wind is inferior to 7 $m.s^{-1}$ about 90% of the time. The wind data being measured at 1.85 m, the wind at the crop canopy height is lower: using the linear relation given in Equation (6.8), the wind speed at 80 cm (wheat canopy height) is about 3 $m.s^{-1}$ for the 90% mark. With reference to Table 6.6, the wind conditions at which the wind and motion data were collected in 2000 are therefore representative of normal conditions.

Figures 6.12(c) and 6.12(d) show that the wind in the summer is significantly lower than in the winter, due to more stable weather conditions in the summer. For that reason it is important to use statistics generated from summer data only, not only because these relate directly to the period when the crop is growing or is fully grown, but also because of the seasonal variation highlighted in Figure 6.12(c) and 6.12(d).

Daily variations

Figure 6.13 shows the cumulative probabilities calculated from data grouped in four categories related to the time of the day (all times being GMT):

- The "night" category is calculated from data recorded between 0am and 6am.
- The "morning" category is calculated from data recorded between 6am and 12am.
- The "afternoon" category is calculated from data recorded between 12am and 6pm.

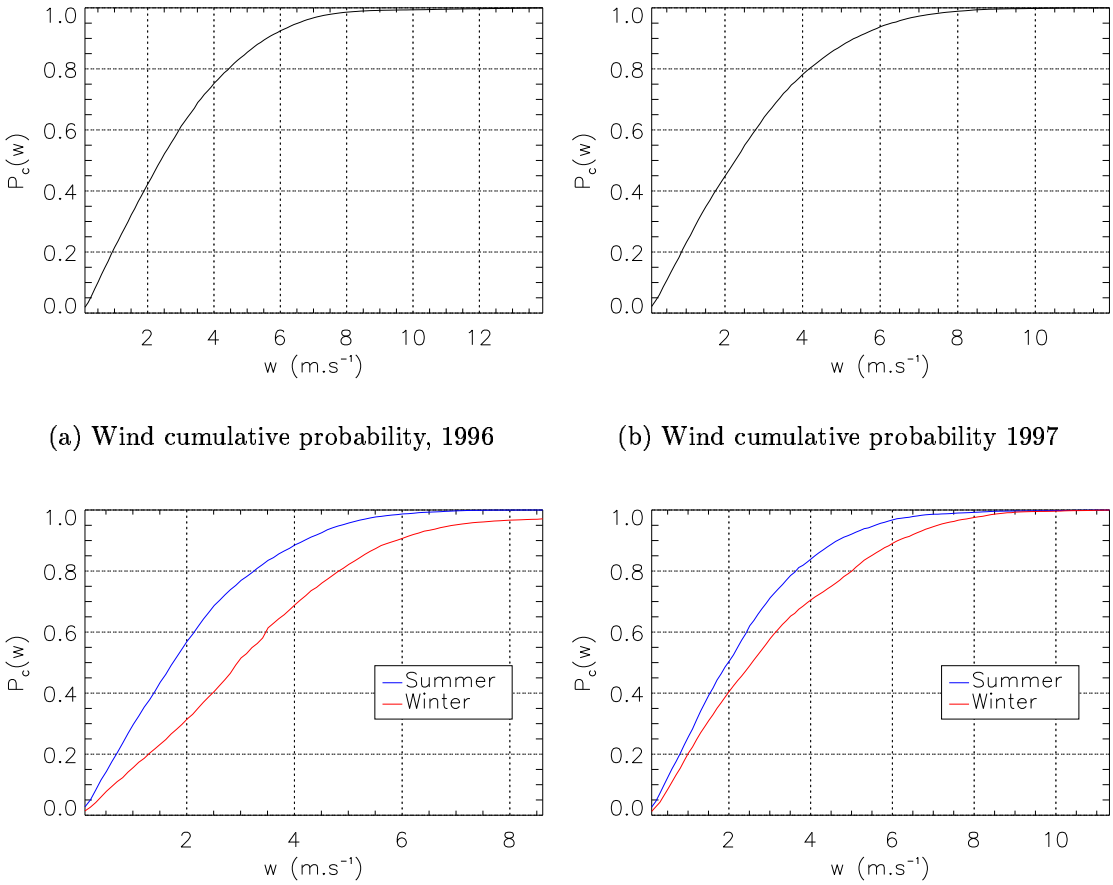

(a) Wind cumulative probability, 1996

(b) Wind cumulative probability 1997

(c) Wind cumulative probability in summer and winter, 1996

(d) Wind cumulative probability in summer and winter, 1997

Figure 6.12: Wind cumulative probability based on wind data collected by the Cranfield Automatic Weather Station in 1996 and 1997

- The "evening" category is calculated from data recorded between 6pm and 12pm.

Figure 6.13 shows that the wind speed at night and in the evening is on average lower than during the day. The highest average wind speed is found in the afternoon, because a given probability is reached by the afternoon curve at higher wind speeds. Differences in wind speeds between the night and afternoon categories at the 50 % probability are about 1 to 1.5 $m.s^{-1}$. Section 6.6.3 will show how the wind statistics presented above can be translated to wheat motion statistics.

6.5 Motion data analysis

This section moves on to describe the motion of the wheat plants measured by the camera system. As already stated in Chapter 4, the motion data represent the displacements of the top part of the canopy. The tracked targets were placed on the wheat heads at all dates except on May 1^{st} and June 6^{th}, when they were fixed to

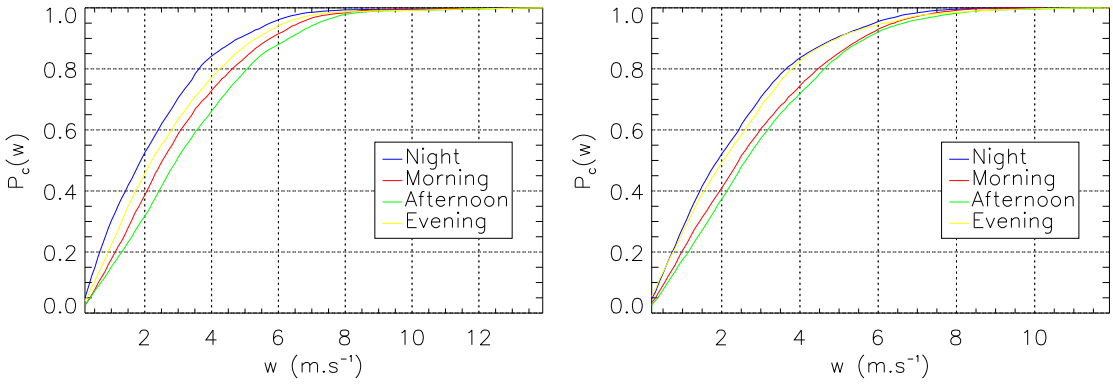

(a) Cumulative distributions, 1996

(b) Cumulative distributions, 1997

Figure 6.13: Cumulative probability of the wind speed, based on data collected by the Cranfield Automatic Weather Station and separated into 4 categories depending on the time of day (night, morning, afternoon, evening

the leaves because the heads had not yet clearly emerged. As for the wind data, the three analyses presented here concern the average displacement of the targets, i.e. their locus over the one minute sequence, then the analyses in the time and frequency domains. The aim of this section is to present the three-dimensional information to be used in Chapter 7 for the understanding of the coherence.

6.5.1 Three-dimensional locus of the targets

General aspect of the loci

Figure 6.14 shows the loci of wheat heads in the (x,y) and (x,z) planes, obtained on June 21st, August 15th, and July 25th. Similar traces are obtained for the other targets and dates, but these three dates are chosen here because they are representative of wheat motion in high, medium, and low wind conditions.

The traces presented in Figure 6.14 are the coordinates of the target (x, y, z) relative to a position P_0 (x_0, y_0, z_0) introduced in Chapter 4. The knowledge of P_0 is irrelevant here since the parameter of interest is the motion of the target rather than its absolute position. Focusing for the moment on Figures 6.14(a) to 6.14(d), the loci of the wheat heads show that the amplitude of the motion in the horizontal (x,y) plane is more important than in the vertical direction. This is due to the fact that the wheat head is fixed to its stalk and therefore has a limited degree of freedom in the z direction. In fact, the point tracked on the wheat head is at a fixed distance from the surface, and for that reason it describes approximately a portion of a sphere whose centre is at the base of the wheat stalk, and whose radius is the height of the wheat head above the surface. This spherical locus can be seen on Figures 6.14(b) and 6.14(d). It tends to be approximately a straight segment because of the high ratio between the length of the wheat plant and the displacement of the wheat head. On these figures, the vertical coordinate of the wheat head decreases with increasing values of x because the longitudinal component of the wind moves from negative to

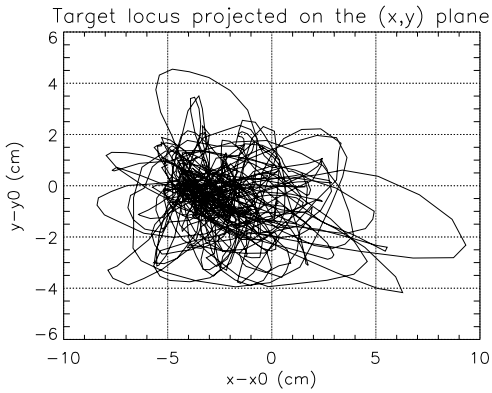

(a) (x,y) plane, June 21^{st}

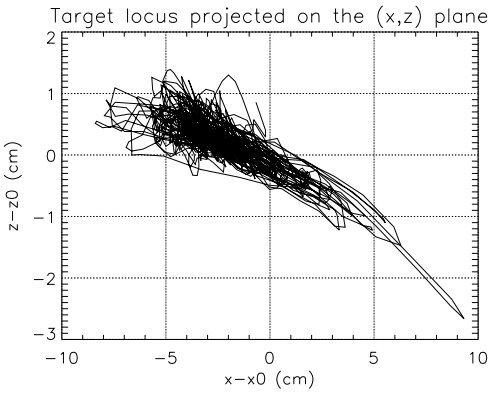

(b) (x,z) plane, June 21^{st}

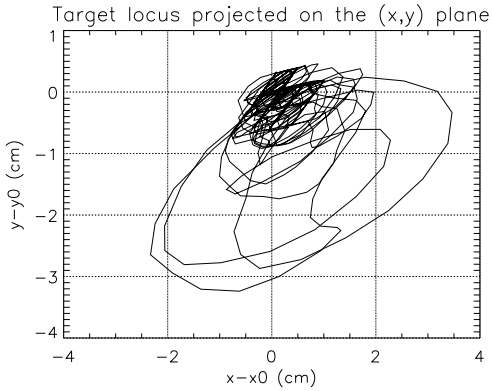

(c) (x,y) plane, August 15^{th}

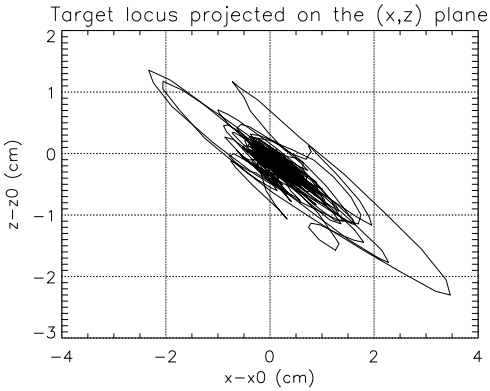

(d) (x,z) plane, August 15^{th}

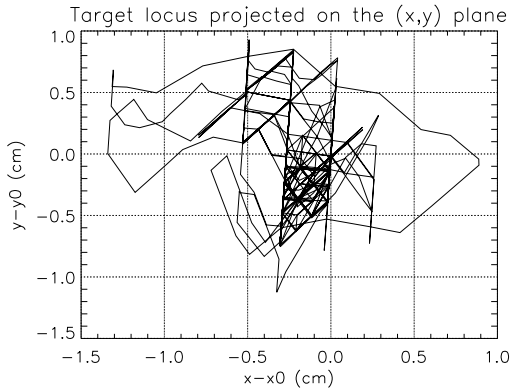

(e) (x,z) plane, July 25^{th}

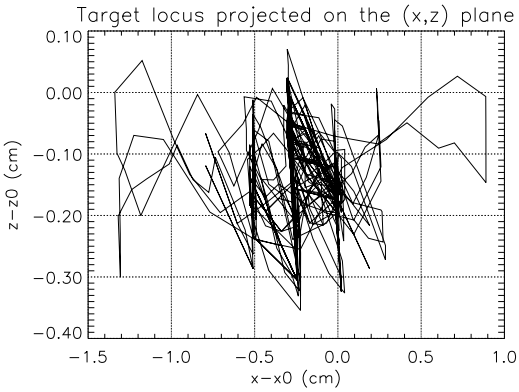

(f) (x,z) plane, July 25^{th}

Figure 6.14: Locus of wheat heads in the horizontal (x,y) plane and in the vertical (x,z) plane, obtained from one minute of video data collected on June 21^{st}, August 15^{th} and July 25^{th} 2000 in a wheat field at Cranfield. Coordinates of the wheat heads are given relative to a fixed position P_0 of coordinates (x_0,y_0,z_0)

positive abscissas in the x direction.

Figures 6.14(a) to 6.14(d) show that the wheat head locus does not strongly follow a particular direction. The motion amplitude in the x direction, which is the mean wind direction, is superior to the amplitude in the y direction but not by a significant amount. Figure 6.14(c) suggests that the wheat head describes an approximate ellipse in the (x,y) horizontal plane, whose size is attenuated by damping effects. This is not so clear on Figure 6.14(a) because the high wind conditions impose a continuous irregular loading on the wheat. In the medium wind conditions of August 15^{th}, the damped ellipse is probably due to a gust of wind acting on the wheat at a particular instant, followed by a period of no wind in which the natural movement of the wheat subject to an initial forcing approaches that of a classic mass-spring-damper system.

The low wind conditions of July 25^{th} are also interesting because they show the accuracy of the measurement system. The amplitudes of the motion shown in Figure 6.14(e) and 6.14(f) are very low, about 2 cm in the x and y directions and less than 0.5 cm in the z direction. With this limited amplitude, the loci have an irregular aspect where the motion seems to be marked by straight segments. These segments represent the accuracy of the system. They are the translation into position coordinates of the 2 pixel accuracy of the tracking algorithm (see section 4.6.7). Their length indicates the accuracy of the system for the particular target-to-camera distance used on July 25^{th}: it is about 3 mm, in all directions. This accuracy value is based on the use of the tracking algorithm in the form described in section 4.6, i.e. without the potential improvements identified in section 4.6.8.

Motion quantitative parameters

Table 6.8 presents the motion amplitudes averaged for all targets tracked at the same date. The amplitude is defined here as the difference between the maximum and the minimum of each coordinate of the tracked elements. The associated standard deviation is also shown in each case. Another parameter which will show its relevance in section 6.6 is the correlation coefficient r^2_{xy} calculated from each (x,y) coordinate of the tracked target. r^2_{xy} represents the spread of the wheat movement around its mean direction of motion. A linear regression trend is calculated from the (x, y) coordinates and the angle between the regression line and the x axis defines the mean direction of motion, η_{disp}. It is also given in Table 6.8.

No standard deviations are given on May 1^{st} since only one target is tracked at that date. The values of Table 6.8 will be discussed in conjunction with the wind parameters in section 6.6, since the different amplitudes, directions of motion, and correlation coefficients are a direct consequence of the wind conditions. The standard deviation on the parameters is high, which shows the variability of the motion from the different targets on the same date. This variability is a consequence of the changeable wind conditions at short spatial and temporal scales, highlighted in the previous section. But it does not necessarily mean that the motion of the wheat elements in the field is totally decorrelated at all times. Figure 6.14(c) shows that a single wind event on a wheat plant can significantly change the maximum amplitude of the motion, as well as the mean motion direction and r^2_{xy}. These isolated motion patterns are different for individual wheat plants and affect the standard deviations

Date	x_{amp}	$\sigma_{x_{amp}}$	y_{amp}	$\sigma_{y_{amp}}$	z_{amp}	$\sigma_{z_{amp}}$	η_{disp}	$\sigma_{\eta_{disp}}$	r^2_{xy}	$\sigma_{r_{xy}}$
	(cm)						(degrees)			
1/5	2.3		4		1.5		-31		0.71	
6/6	9.5	4.1	6.4	3.1	2.8	1.6	9.7	24.7	0.47	0.26
21/6	17.8	1.0	11.2	2.1	5.8	1.5	-10.2	6.8	0.23	0.12
19/7	9.5	3.7	8.2	2.0	1.8	0.8	-33.0	8.9	0.70	0.11
25/7	2.3	0.2	2.4	0.6	1.1	0.5	11.3	21.6	0.33	0.30
2/8	14.3	5.1	13.1	3.1	4.3	1.7	9.3	7.0	0.26	0.13
15/8	3.4	1.4	2.5	1.4	2.2	1.0	23.2	8.0	0.43	0.15

Table 6.8: Average amplitude (difference between maximum and minimum of the x, y, and z coordinates) of the tracked wheat elements, mean direction of displacement in the horizontal (x,y) plane with respect to the x direction, correlation coefficient between the x and y coordinates, and associated standard deviations. Values are based on the one minute of video data collected at each date from targets in a wheat field at Cranfield.

on the average values given in Table 6.8. The motion amplitudes also confirm that there is not a clear predominance of the displacement in the x direction.

Position distribution

The locus information presented above is useful because it can be translated into a slant range displacement along a look direction defined by an azimuth and an incidence angle. Section 3.4.2 gives the necessary transformation for that purpose, and shows how the slant range displacement is used for the statistical modelling of the coherence. The distribution of the target positions along the radar look direction helps to define a phase distribution for the dynamic components of the coherence model. The wheat head loci such as those displayed on Figure 6.14 provide the missing information about the position of the scatterers.

In order to calculate the position distributions, the coordinates of the target are shifted so the origin is at the mean position. From these coordinates, the positions along the slant range direction are calculated with Equation (3.7). Then a histogram is derived from these slant range positions by counting the number of points in successive intervals along the slant range coordinate axis. The size δs of the interval is set to 2 mm, the approximate resolution of the measurement system. From the division of the histogram values by the total number of points of the data set (1 minute at 25 frame/s contains 1500 data points), a slant range distribution is obtained. For a given slant range displacement s_{disp}, the associated value $p(s_{disp})$ of the distribution is in fact the probability that the scatterer is in a position seen as a displacement $s_{disp} + \delta s$ along the slant range direction. Figure 6.15 shows an example of the probability distribution obtained by the method above, from the target whose locus was presented in Figures 6.14(a) and 6.14(b) (June 21^{st}). In this particular example, the azimuth direction is set to 0° (i.e. along the x axis of the coordinate system) and the incidence angle is 25°.

$p(s_{disp})$ does not peak at $s_{disp} = 0$, due to some skewness introduced by motion

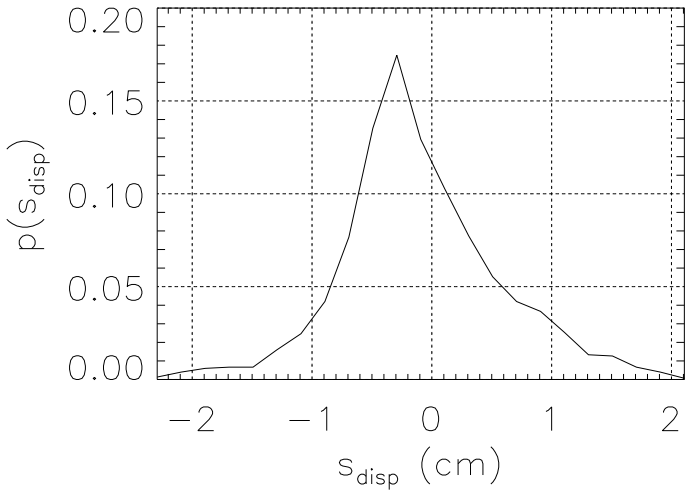

Figure 6.15: Probability distribution of the displacement in slant range of target 1 (wheat head) on June 21^{st} 2000: p(s_{disp}) is the probability that the target displacement in slant range is between s_{disp} and $s_{disp}+\delta s$. Here, δs = 2 mm. Radar parameters used for the calculation: incidence angle=25°, azimuth angle=0°

asymmetry. This asymmetry is also visible in the shape of the distribution function. The conclusion here is that the motion information obtained from *in situ* measurements can help to define more accurately the properties of the vegetation medium for modelling purposes. Distributions such as that of Figure 6.15 provide a more accurate statistical description of the position of the scatterers.

6.5.2 Time analysis

Example of time variation

Figure 6.16 is an example of the trace obtained for a 60 second sequence of video data. The target used here to illustrate the motion is the same as in Figure 6.14(a) and 6.14(b).

The oscillating motion of the wheat head in the x and y directions is initiated by wind forcing. In wind-free conditions, a damped oscillation would probably be observed, but it is difficult to discern it in the plots because the force caused by the wind is continuous and irregular in speed. A frequency peak is expected on the power spectra associated with these time traces at the oscillating frequency. From Figures 6.16(a) and 6.16(b), the estimated oscillated frequency is about 1 Hz.

A gust of wind at time $t \approx 31s$ is responsible for the peak displacement of the target in the x and z directions. This illustrates the point made earlier that a single wind event can cause the maximum amplitude of the motion to change significantly from it would be in the absence of that wind gust.

Autocorrelation analysis

The autocorrelation of $x(t)$, $y(t)$, and $z(t)$, represent how the positions of a single target at two different times relate. Since Figure 6.16 has shown that the wheat

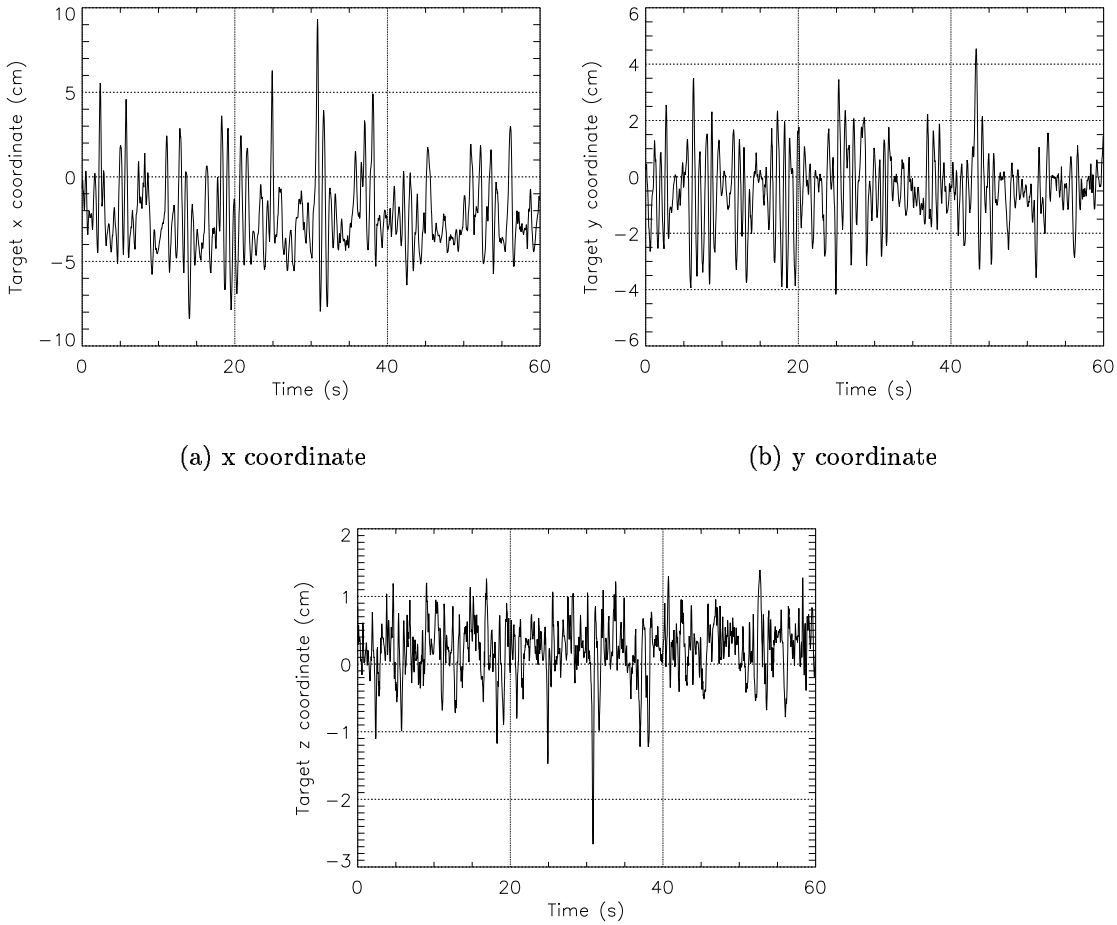

(a) x coordinate

(b) y coordinate

(c) z coordinate

Figure 6.16: Time variation of the coordinates of target 1 (wheat head) on June 21^{st}. Wheat height is 0.8 m

head follows an oscillating motion, it should be reflected on the autocorrelation functions. Figure 6.17 shows the autocorrelation functions calculated from the same coordinates shown in Figure 6.16 (June 21^{st}).

The autocorrelation functions displayed in Figures 6.17(a) and 6.17(b) can be approximated by exponential cosine functions typical of a damped oscillation motion. The period of the oscillation in the autocorrelation functions equals the period of oscillation of the corresponding coordinate ($\approx 0.8s$), and the amount of damping can be estimated by quantifying the exponential decay. After a time lag superior to about 2 seconds, there is no further decay and the autocorrelation functions still maintain a sinusoidal shape, but at much reduced amplitude. It shows that the oscillation is a consistent feature of the wheat motion for the entire minute of data, but is not correlated to the initial oscillation at time lag 0. This feature can also be observed in Figure 6.16, where the oscillations are grouped in "packets" rather than continuous. The autocorrelation function for the z coordinate does not follow the same pattern as for the x and y coordinates (Figure 6.17(c)). Indeed the po-

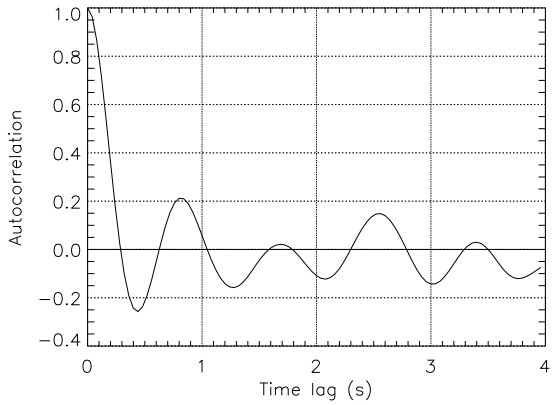

(a) ACF, x coordinate

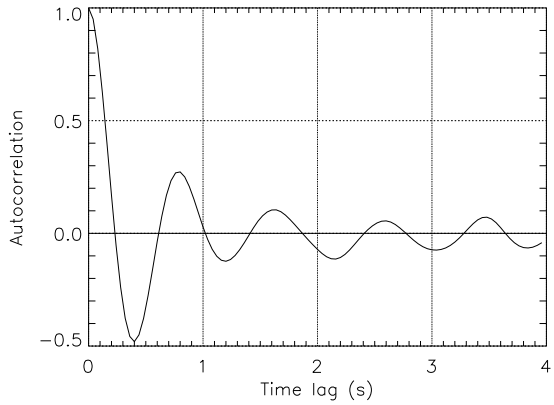

(b) ACF, y coordinate

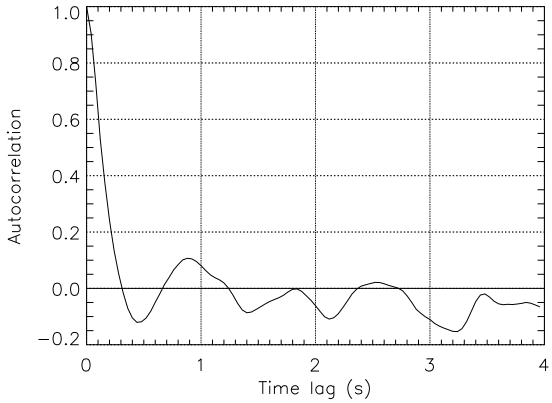

(c) ACF, z coordinate

Figure 6.17: Autocorrelation function of the 3 coordinates of target 1 (wheat head) on June 21^{st} 2000

sition variation in the vertical direction does not show in Figure 6.16(c) the same oscillations as for the two horizontal directions.

Obviously the exact variation of the autocorrelation functions as a function of time lag depends on the wind conditions, but it also depends on the growth state. Similar variations to those shown in Figures 6.17(a) and 6.17(b) were obtained for all targets at dates when the wheat head had emerged and was in its upright position. The two dates when the wheat does not have this phenological state are May 1^{st}, when only leaves are present in the field, and August 15^{st}, when the dry wheat head fold down. The autocorrelation functions in those two cases are shown in Figure 6.18. They show that the characteristic pattern of a damped oscillation is not present due to a specific motion behaviour.

On May 1^{st}, the tracked target is placed on a wheat leaf because the wheat heads have not emerged yet. Due to this absence of wheat heads, the plant does not behave like a mass-spring-damper system as it does in the subsequent dates because it has neither the rigidity of a full grown stalk, nor the extra mass at the top of the stalk.

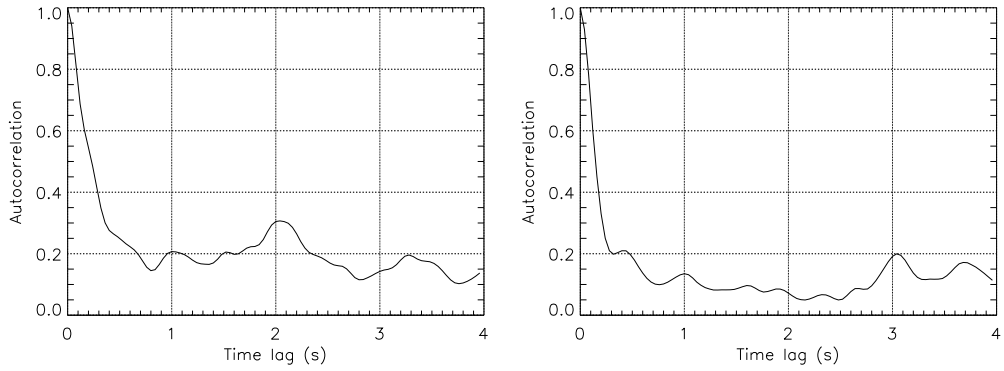

(a) ACF, x coordinate, May 1^{st} (b) ACF, x coordinate, August 15^{st}

Figure 6.18: Autocorrelation function of the x coordinate obtained from motion data on May 1^{st} (wheat leaf) and August 15^{st} (wheat heads in physical contact with neighbouring plants)

Consequently no oscillation appears in the movement. On August 15^{th}, the absence of oscillation is thought to be due to the folding of the wheat heads: the plants in close neighbourhood are more interrelated by direct contact, and do not behave as individual plants but move simultaneously in groups. For this reason, their natural oscillating motion is impeded and does not show on the autocorrelation function of Figure 6.18(b). For completeness here, it should be noted that autocorrelation functions from some of the other targets on August 15^{th} do have the sinusoidal shape shown in Figure 6.17. So the existence of oscillations in the motion depends on the degree of physical contact between the different elements.

Cross-correlation of the motion in the x direction

The cross-correlation between the coordinates of several targets gives a quantitative estimate of the motion similarity between spatially separated wheat elements. From observations by eye, it is clear that wheat elements in a field seem to have a common motion, at least at a short spatial scale. Since there seems to be some spatial patterns to the motion in a field, the cross-correlation functions should reflect it and help to determine its spatial extent. This is an important aspect of the observations, because the coherence model presented in section 3.4 uses the concept of an equivalent scatterer, i.e. a scatterer whose motion is representative of all the real scattering elements in the vegetation medium. The cross-correlation functions will help to determine at which spatial scale this concept is valid. For clarity, the analysis below will concentrate primarily on the x coordinate of the targets. Discussion about the y and z coordinates will be given later in the section.

To illustrate how the cross-correlation functions are used to analyse the relative motion of the wheat plants, the data obtained on August 2^{nd} are used in the following discussion. The results presented below are representative of the results found for other dates, except in specific cases which will be mentioned later. Figures 6.19(b) to 6.19(d) show the cross- correlation functions between 3 pairs of targets, and Figure

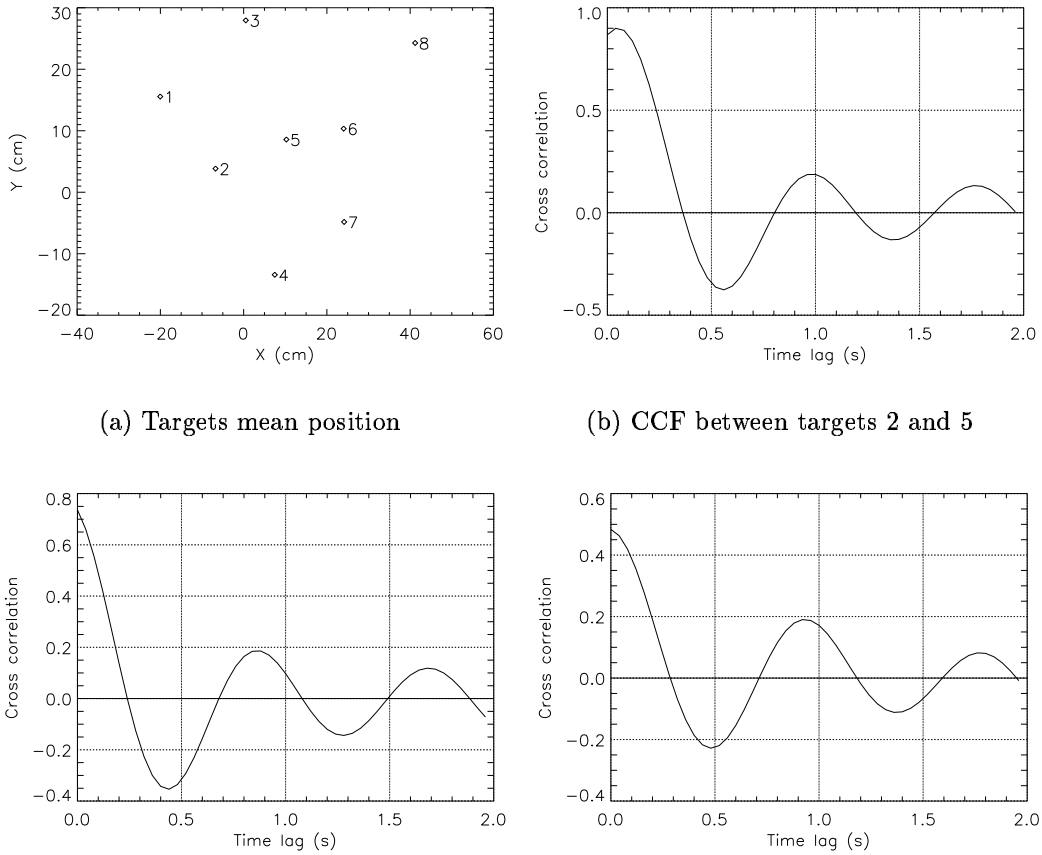

(a) Targets mean position

(b) CCF between targets 2 and 5

(c) CCF between targets 4 and 5

(d) CCF between targets 4 and 8

Figure 6.19: Mean position of the tracked targets on August 2^{nd} 2000 and cross-correlation functions (CCF) between the x coordinates of targets 2, 4, 5, and 8 (all wheat heads)

6.19(a) gives the average position of the targets in the reference coordinate system.

The first feature to note on the cross-correlation functions is the sinusoidal shape already observed in the autocorrelation function, and related to the oscillation of the wheat plants. Figure 6.19(b) shows that the maximum correlation between targets 2 and 5 occurs after a short time delay of about 0.05 s. This is the time required by the wind to travel the distance separating the two targets, consequently affecting them in a similar way. Targets 2 and 5 being aligned in the x direction, which is also approximately the mean wind direction, there is a delay between the similar motion of the two targets. The fact that this delay truly corresponds to the wind travelling time between the targets is confirmed by Figure 6.19(c). Targets 4 and 5 are nearly aligned in the y direction, i.e. perpendicular to the mean wind direction, and their peak cross correlation occurs at time $t = 0$ because they are subject to the same wind forcing at the same time. This conclusion is of course to be moderated by several factors. First, the wind does not consistently have the same direction, perpendicular to the y direction, and the same speed at different points, as shown in section 6.4. Secondly, the distance between the targets should be smaller than a

maximum distance for the same wind pattern to affect them in a same way. This is illustrated by Figure 6.19(d), where the cross-correlation between targets 4 and 8 peaks at $t = 0$, but the peak value is only 0.5, compared to the values of 0.9 and 0.75 of the two other figures. The peak is lower between targets 4 and 8 because Figure 6.19(a) shows that they are further apart.

Estimate of the motion correlation distance

The strength of the cross-correlation between the motion of two targets is quantified by the maximum value of the cross-correlation between these targets. With a set of several targets for a given date, it is possible to plot the peak cross-correlation between each pair of targets as a function of their distance. Such a plot is presented in Figure 6.20. It is obtained from the data collected on August 2^{nd}.

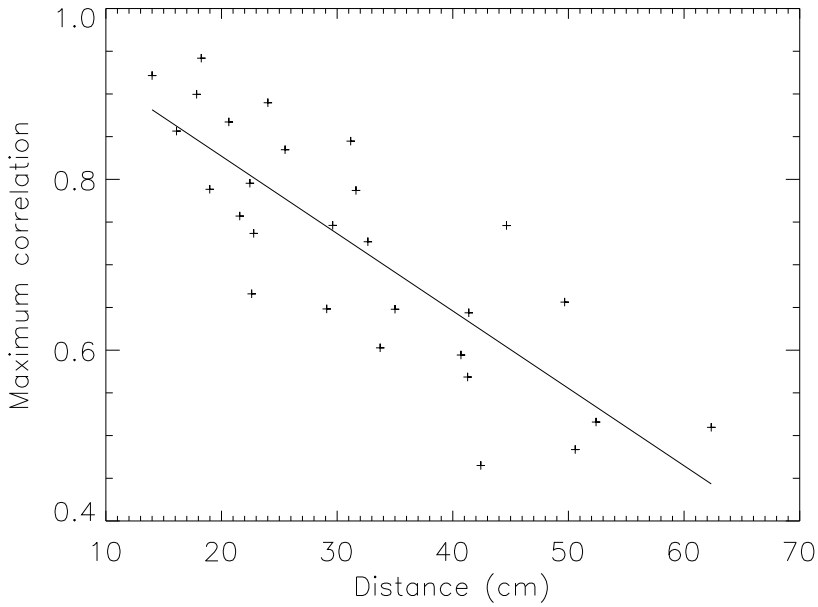

Figure 6.20: Maximum cross-correlation of the x coordinate for each target pair vs. distance between the targets tracked on August 2^{nd}. See Figure 6.19(a) for mean positions of the targets in the measurement volume.

It is clear from Figure 6.20 that the similarity in the motion of wheat plants decreases with increasing distance between them. When two wheat plants are close to each other, they are subject to a similar wind forcing and therefore their motion is highly correlated. For a fixed distance between the targets, the variability of the peak correlation is related to the relative position of the two targets with respect to the mean wind direction.

The correlation distance is defined here as the maximum distance which must separate two wheat plants for their motion to be correlated. Obviously there is not in reality a clear demarcation between correlated and decorrelated motion, as Figure 6.20 shows that the correlation decrease is progressive. However, it is useful to define a threshold for the minimum correlation under which the motion of wheat plants is said to be decorrelated. Since the definition of the threshold determines the value of the correlation distance, it is worth explaining here how its value was

chosen. For the entire range of distances displayed in Figure 6.20, the decrease of the cross-correlation can be approximated by a linear regression line. For long distances, say of the order of 1 m or more, the correlation is expected to be small, i.e. close to 0. An exponential decrease of the cross-correlation with increasing distance is a good approximation of this variation, in the entire distance range. Assuming that this exponential function describes the variation of the cross-correlation, a threshold value commonly used to define correlation lengths is the value $1/e$. For that reason, the correlation distance is defined here as the distance at which the regression line shown on Figure 6.20 reaches the value $1/e$ (≈ 0.368). With such a definition, the correlation distance d_{c_x} is calculated for all recording dates, and the values obtained are given in Table 6.9.

Date	6/6	21/6	19/7	25/7	2/8	15/8
d_{c_x} (cm)	47	94	54	130	71	35
Number of targets tracked	5	3	5	6	8	8

Table 6.9: Correlation distance d_{c_x} obtained from the cross-correlation functions between the targets' x coordinates, for all recording dates in summer 2000. The decorrelation threshold is set to $1/e$. The number of targets tracked at each date indicates the significance of the estimated correlation distance.

Note that the correlation distance on May 1^{st} is not estimated because only the position of a single target is available at that date. Even at the other dates, the total number of targets successfully tracked in the image is important because, with more available targets, more cross-correlation functions can be calculated and more points can be plotted on graphs similar to Figure 6.20. It follows that the significance and accuracy of the regression line is higher when more targets are available, and consequently the correlation distance can be assumed to be representative. It is for that reason that the value of d_{c_x} obtained on June 21^{st} ($d_{c_x} = 94cm$) should not be accounted for in the analysis because only 3 targets were available to derive it. For all other dates, at least 5 targets were available, so the correlation distances are meaningful.

The correlation distances of Table 6.9 cover a significant range of values which should be justified here. On July 25^{th}, the mean wind speed was very low for the minute of recorded video data ($\overline{w} \approx 0.88\ m.s^{-1}$) and therefore the motion of individual wheat plants were not correlated because the wind was too weak to affect their motion in the same way. In fact, the plot equivalent to Figure 6.20 obtained with the data of July 25^{th} shows that the cross-correlation at all distances is consistently low (≈ 0.4), and varies very little with increasing distance. This is the reason why the correlation distance on July 25^{th} is particularly high ($d_{c_x} = 130cm$), but it does not correspond to a true spatial correlation of the motion.

For all other dates, the values of d_{c_x} can be compared. The lowest value is obtained on August 15^{th} ($d_{c_x} = 35cm$). It was explained earlier that the motion at that date is affected by the strong interactions between adjacent plants due to their folded head which tends to link the plant together. $d_c = 35cm$ represents the

size of these packets. On June 6^{th}, the targets were still fixed on wheat leaves, so it is probable that they can have a higher degree of freedom than wheat heads and consequently have a shorter correlation distance ($d_{c_x} = 47cm$) than on July 19^{th} ($d_{c_x} = 54cm$) and August 2^{nd} ($d_{c_x} = 71cm$).

The important conclusion from the analysis above is that the motion of wheat elements in a field is not totally spatially decorrelated and it was possible to calculate the spatial extent of this correlation. From the coherence modelling point of view, the concept of an equivalent scatterer is valid within the area of coherent motion. The analysis presented here will be used in Chapter 7 to derive coherence estimates.

Cross-correlations in the y direction

The cross-correlations between the y coordinates of two targets yield similar results to those obtained above with the x coordinate, so the same comments apply. The only exception arises for data collected on June 6^{th}: the peak cross correlations from the y coordinates at that date are consistently low, even at short time lags. On June 6^{th}, the wheat is still in a leafy state and the motion of these leaves is correlated only in the mean wind direction.

The correlation distances calculated in a similar way as above, but using the y coordinates of the targets instead of the x coordinates, yield the following values:

Date	6/6	21/6	19/7	25/7	2/8	15/8
d_{c_y} (cm)		73	54		80	54

Table 6.10: Correlation distance obtained from the cross-correlation functions between the targets' y coordinates, for all recording dates in summer 2000. The decorrelation threshold is set to $1/e$.

On June 6^{th}, d_{c_y} is not calculated for the reasons explained above. On July 25^{th} the correlation distance is also not estimated, due to the low wind conditions, as already commented earlier. At the other dates, the correlation distances obtained are of the same order of magnitude as those obtained for d_{c_x}. The maximum difference between d_{c_x} and d_{c_y} is 21 cm, which is significant, but does not change the conclusion made earlier that the motion of wheat plants is correlated, and that the spatial extent of this correlation is of the order of 0.5 m on average.

No attempt was made to make a correlation analysis with the vertical coordinate of the targets because the extent of the displacements along the z axis is limited and is a function of the displacement in the x and y direction, and of the geometry of the wheat plant.

The "honami" phenomenon

The honami phenomenon is the wave-like motion of the surface of the wheat canopy which appears in some fields on windy days. The motion of the wheat in these conditions seems to be correlated over much longer distances than the half metre derived in the discussion above. For that reason it is worth mentioning it here, in order to complete the analysis of wheat motion.

The wave-like motion of the wheat was observed in the field on June 21^{st}, which was the most windy day. The cross-correlation function between targets 1 and 6 on that day is similar to that of Figure 6.19(b) and peaks after a time lag of about 0.12s. The two targets are separated by a distance of 50 cm. With these two values, it is possible to derive a simplified model of this honami. The displacement of the stalks in the canopy can be approximated by a travelling wave:

$$\xi = \xi_0 \exp\left[2\pi i \left(\frac{x}{\lambda} - ft\right)\right] \tag{6.9}$$

where ξ(x) is the displacement in the x direction of the stalk from its mean position, ξ_0 is the motion amplitude, λ is the wavelength of the travelling wave, and f the frequency of the stalk oscillation. The phase velocity $v = \lambda f$ is the velocity at which the wave seems to travel in the wheat field. It can be approximated using the wheat motion measurements:

$$v = \frac{\Delta x}{\Delta t} \tag{6.10}$$

where Δt is the time lag at which the cross correlation peaks (Δt=0.12 s), and Δx is the distance between the two targets (Δx=50 cm). The resulting phase velocity is 4.2 $m.s^{-1}$. This is the velocity at which the wave appears to travel, and it is higher than the mean wind speed measured for that date ($\approx$ 3.70 $m.s^{-1}$ during the minute of processed video data). This suggests that the wave shaped motion appearing in wheat fields is caused by gusts of high wind rather than weaker, constant, winds.

Figure 6.16(a) shows that a single oscillation pattern such as the one occurring at time $t \approx 31s$ lasts approximately 3 seconds. During this time of coherent motion, the wave pattern travels a distance of 4.2x3= 12.6 m. This length is an approximation of the length of a single waving patch in a wheat field. Although it is difficult to assess the accuracy of the approximate calculation above, a value of about 10 metres for a wave-like motion pattern at the surface of the field seems compatible with simple observations by eye.

It is difficult to define the conditions required for the honami phenomenon to appear in a wheat field. However it is quite common to see such motion on windy days, so the main condition seems to be related to the wind speed. Other possible parameters such as the wheat growth stage could not be assessed here since the phenomenon was only clearly observed on one occasion.

6.5.3 Frequency analysis

The analysis of the wheat motion in the frequency domain is expected to highlight the oscillating behaviour of the wheat plants, already pointed out in the previous sections. For that purpose, the power spectrum of time varying x coordinate of each target was calculated for each date. Figure 6.21(a) is an example, obtained from measurements on August 2^{nd}.

The peak frequency on the spectra is at $f \approx 1.2$ Hz. This frequency is the oscillating frequency for that particular wheat plant and date. Every target on each data set can be used to produce graphs similar to Figure 6.21. For each date, the peak frequencies obtained from all targets was used to calculate an average peak

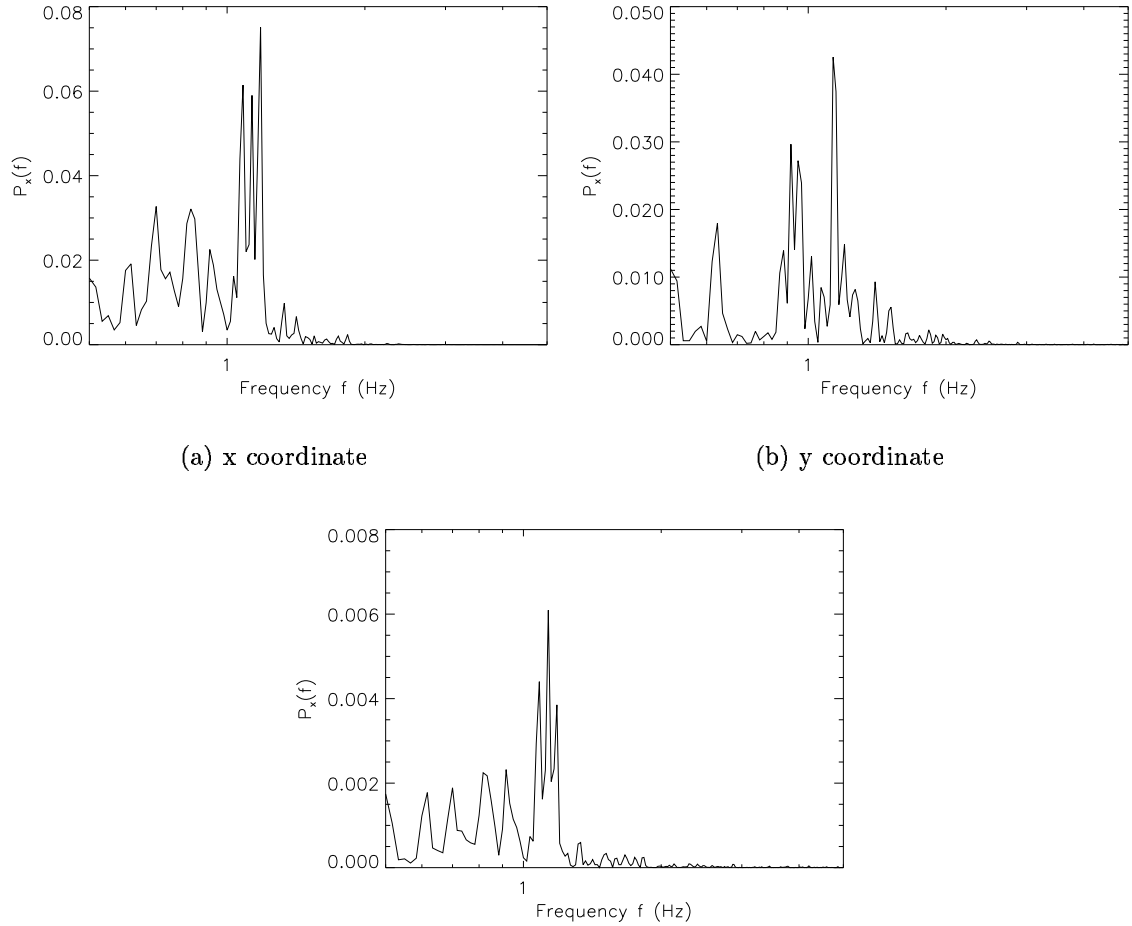

(a) x coordinate

(b) y coordinate

(c) z coordinate

Figure 6.21: Power spectra of the 3 coordinates of target 5 (wheat head) obtained from data collected on August 2^{nd} 2000, based on 1 minute of video data.

frequency $\overline{f_{peak}}$ and a standard deviation $\sigma_{f_{peak}}$. They are given in Table 6.11 for all recording dates.

The oscillation frequency varies from about 0.9 Hz to 1.4 Hz, but it is difficult from the values of Table 6.11 to discern a clear variation pattern which could for example be related to the wheat phenotype. It is probable that some coupling between the motion of the main stalk and that of the leaves influence the oscillation, but these complex interactions do not clearly appear in the spectra. Similarly, the motion of leaves at the early growth stage (May 1^{st} and June 6^{th}) does not yield spectra significantly different from those obtained at later dates. The secondary peaks in the power spectrum of Figure 6.21(a) can be associated with the frequency of wind gusts, rather than being representative of secondary motion effects.

The detailed interpretation of the power spectra, other than noting the peak frequency and relating it to the main oscillation frequency of the wheat plant, is subject to assumptions which are difficult to verify, and for that reason will not be investigated further here. It should noted however that the oscillation frequencies

Date	1/5	6/6	21/6	19/7	25/7	2/8	15/8
$\overline{f_{peak}}$ (Hz)	0.92	1.36	1.32	0.88	1.14	1.19	1.33
$\sigma_{f_{peak}}$ (Hz)		0.21	0.09	0.03	0.17	0.06	0.46

Table 6.11: Average peak frequency obtained from the power spectrum of the targets, for each recording date in summer 2000, and associated standard deviations

obtained for wheat here are higher than those published in [45], where f_{peak}=0.7 Hz. Such a difference can be due to a different wheat type. For comparison, the oscillation frequency of corn is about 1.5 Hz [67].

6.6 Relation between the wind velocity vector and the motion of wheat

In this section the motion of the wheat is studied in conjunction with the wind conditions at each date. So far the analysis has focused on presenting features of the two data sets separately. The wind being the direct cause of the motion of the wheat, some relations are bound to appear between the two. However, the presentation of the wind data and the motion data have shown that they are both complex and sometimes difficult to interpret. For that reason, the mechanisms which relate the two data sets are also expected to be complex. So the analysis to be presented here will go from the simplest approach (the analysis of 1 minute averages) to more complex attempts to relate the wind and the wheat motion.

6.6.1 Wheat motion locus and mean wind conditions

The mean parameters of the wheat motion were given in the previous section, Table 6.8. The mean wind conditions used for comparison are not those given in Tables 6.4 to 6.6 because they were calculated with the entire wind data sets. The mean wind speed, the mean wind direction, and the turbulence intensities required for comparison with the wheat motion should be calculated from the one minute sequence used to create the motion data set at each recording date. This is where the synchronisation of the wind data logger with the video cameras is useful. The average wind parameters for the one minute sequence synchronised with the motion data are given in Table 6.12. They correspond to wind data at the wheat height.

The values obtained for the entire wind data set (see Table 6.6) differ slightly from those given in Table 6.12. The average wind speeds in the 1 minute subset are higher than for the full set because the one minute of video and wind data processed was chosen to contain one or more peaks in wind speed, expected to have a significant impact on the motion. The wind speed directions differ from up to about 20° and the turbulence intensities from up to 20% of their value calculated with the full data sets. This shows that it is useful to calculate the wind parameters from the 1 minute subset for accurate comparison with the wind motion.

Date	$\overline{wind}$ $(m.s^{-1})$	η_{wind} (deg)	i_u	i_v
6/6	2.8	-10.5	0.28	0.32
21/6	3.7	-4.5	0.37	0.36
19/7	2.2	-31.4	0.40	0.41
25/7	0.9	-35.5	0.44	0.44
2/8	2.8	3.7	0.39	0.36
15/8	1.7	-24.0	0.54	0.43

Table 6.12: Mean wind speed, mean wind direction relative to the DVA triad x axis, and turbulence intensities along and across wind, obtained with the one minute period of wind data synchronised with the wheat motion data processed.

Mean wind speed and motion amplitude

The motion amplitudes in the x and y directions given in Table 6.8 are plotted against the mean wind speed for each date in Figure 6.22. The amplitudes x_{amp} and y_{amp} are defined as the difference between the maximum and the minimum of the target coordinates in the x and y directions respectively.

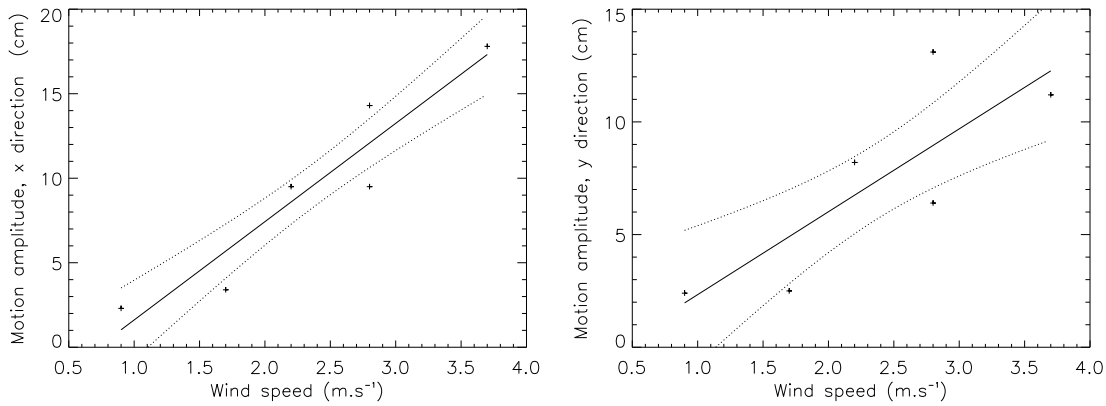

(a) Amplitude in the x direction

(b) Amplitude in the y direction

Figure 6.22: Average wheat amplitude in the x and y directions from all targets at a recording date vs. mean wind speed at the corresponding date, with regression line (solid line) and 80% confidence interval (dotted lines) on the linear estimates

The amplitude of the motion in the x direction is linearly correlated with the mean wind speed. The correlation is also good in the y direction. The equations of the regression lines shown in Figure 6.22 are:

$$x_{amp} = 5.81 * \bar{w} - 4.20 \quad (6.11)$$

$$y_{amp} = 3.68 * \bar{w} - 1.34 \quad (6.12)$$

where $\bar{w}$ is the wind speed and x_{amp}, y_{amp} the motion amplitudes in the x and y

directions. The correlation coefficients on the linear relations are 0.94 and 0.81 for the x and y amplitudes respectively. But if Equations (6.11) and (6.12) are to be used to make predictions of the expected motion amplitudes for a given wind speed, the derivation of confidence intervals for these predictions is a more useful parameter. The standard formula for the confidence interval associated with predictions from a linear regression is given in [68]. The 80% confidence intervals associated with the predictions by the linear fit are plotted on Figures 6.22(a) and 6.22(b). These intervals show that the amplitude of the wheat motion can be predicted from Equations (6.11) and (6.12) with 80% confidence with an accuracy of about 5 cm. This rather poor accuracy is due to the limited number of points used to calculated the linear regression. It is expected that the accuracy level would improve if more points were present in Figure 6.22. Obtaining more points can be achieved in two ways. Either by making more measurements in a variety of wind conditions, or by using the existing data and processing other 1 minute sequences. The former solution is left as a potential improvement on the results for future measurement campaigns. The latter solution is not ideal because the new points on Figure 6.22 would be derived from similar wind conditions to those already existing, and therefore the points along the wind speed axis would not be evenly spread. For the purpose of the research here, which is to demonstrate how the measurements can be used in the context of coherence understanding, the relations given in Equations (6.11) and (6.12) are assumed to be valid, but their limited accuracy is acknowledged.

Equations (6.11) and (6.12) are useful because they link the expected motion amplitude to the mean wind speed at canopy level. Since the wind speed at canopy level is related to the wind speed at higher heights by Equation (6.8), it is possible to translate the wind statistics obtained from the weather station data in section 6.4.4 into motion statistics of the wheat. These motion statistics can in turn be used to calculate the probability to obtain a certain coherence level from a wheat field. This last aspect will be presented in Chapter 7.

It should be noted that the linear fit described above is obtained with wheat in different growth stages, from the leafy state of June 6^{th} to the dry stage of August 15^{th}. For that reason, Equations (6.11) and (6.12) are empirical and do not take into account the fact that different motion mechanisms are at the origin of the points of Figure 6.22.

Variability on the motion amplitude

The standard deviation of the motion amplitude in the x and y directions originates from the fact that several targets are tracked in each video image and therefore each individual amplitude is different. The study above used the mean amplitude calculated from these several targets, and here the associated standard deviation is considered. Figure 6.23 shows the standard deviation of the motion amplitude in the x and y directions as a function of the mean wind speed.

The regression lines shown in Figure 6.23 are calculated with the 5 points for which the average wind speed in inferior to 3 $m.s^{-1}$. For these 5 points there is a good linear fit, showing that the variability of the amplitude increases with increasing wind conditions. Standard deviations of about 5 cm and 3 cm are found on the x and y amplitudes respectively at $\bar{w} = 3m.s^{-1}$. So using Equations (6.11)

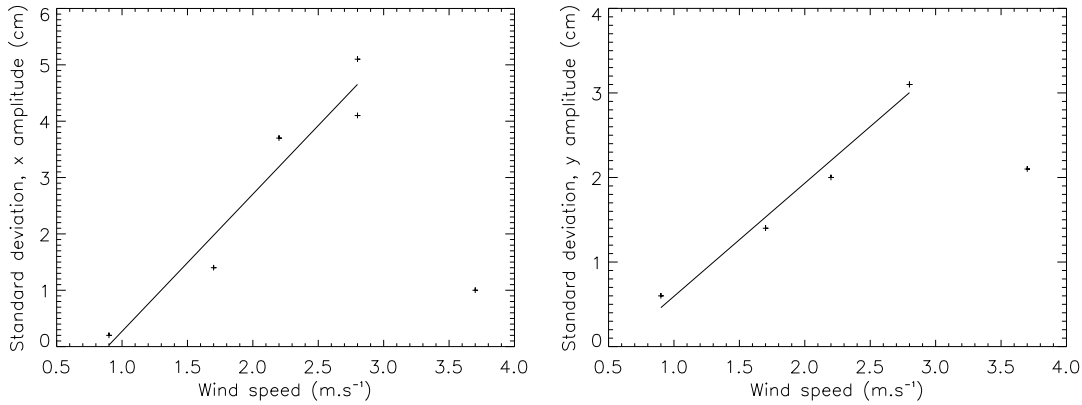

(a) x direction (b) y direction

Figure 6.23: Standard deviation on the estimated wheat amplitude in the x and y directions from all target at each recording date vs. mean wind speed at the corresponding date. The regression line is based on mean wind speeds inferior to 3 $m.s^{-1}$.

and (6.12) to predict the wheat motion amplitude from the wind speed is limited by these accuracy bounds.

The point obtained for $\bar{w}$=3.7 $m.s^{-1}$ in Figure 6.23(a) shows a low standard deviation ($\sigma_{x_{amp}} = 1cm$), which means that the motion of the several targets at that date (June 21^{th}) is consistent in the x direction. There are two explanations for this particular feature. First, it can be due to the fact that only three targets were successfully tracked on June 21^{st} and their motion can be consistent by simple coincidence. The second reason is that the honami phenomenon on June 21^{st}, which was particularly clear at that date, infers a high motion coherence between individual wheat elements. However, this was not observed from the motion cross-correlation analysis presented earlier, so it is likely that the low standard deviation is simply due to a coincidence. The same reasoning applies to the y coordinate. It highlights the importance of having a representative number of targets in the field of view, in order to increase statistical significance.

Mean wind direction, mean motion displacement angle, and correlation coefficients

The wind being the direct cause of the wheat motion, one should expect to obtain similar angular values for the mean wind direction η_{wind} and the mean direction of motion η_{disp}. These values have already been given in previous tables, but are repeated here in Table 6.13 for easier comparison, together with the correlation coefficients of the (x,y) coordinates (r^2_{xy}).

There is a good agreement between the wind direction and the mean motion direction on June 21^{st}, July 19^{th}, and August 2^{nd}: η_{wind} and η_{disp} differ only from a few degrees which can be explained by alignment errors between the triad reference system and the wheat motion reference system. However the low correlation

Date	6/6	21/6	19/7	25/7	2/8	15/8
η_{wind} (°)	-10.5	-4.5	-31.4	-35.5	3.7	-24.0
η_{disp} (°)	9.7	-10.2	-33.0	11.3	9.3	23.2
r^2_{xy}	0.47	0.23	0.70	0.33	0.26	0.43

Table 6.13: Mean wind direction relative to the DVA triad x axis and mean motion direction of the tracked targets relative to the x axis of motion reference system, obtained for all recording dates in summer 2000, in a wheat field at Cranfield. The wind and motion reference systems being aligned, the angular values are directly comparable.

coefficients for these motion data points on June 21^{st} and August 2^{nd} indicate that the motion is widely spread around the mean line of displacement. It follows that the apparent good agreement between η_{wind} and η_{disp} could simply be the result of a fortunate coincidence rather than the expression of a causal relation between the wind forcing and the wheat motion. The angular values obtained for η_{wind} and η_{disp} on July 19^{th} are similar and r^2_{xy} is high. There seems to be here a good direct relation between the wind direction and the motion direction at that date. Angular values obtained on June 6^{th}, July 25^{th} and August 15^{th} show large discrepancies of up to about 50°. The low correlation coefficients in the 3 cases can explain the high differences between η_{wind} and η_{disp}. Figure 6.24 shows that the difference between the wind direction and the direction of motion is more important in low wind conditions.

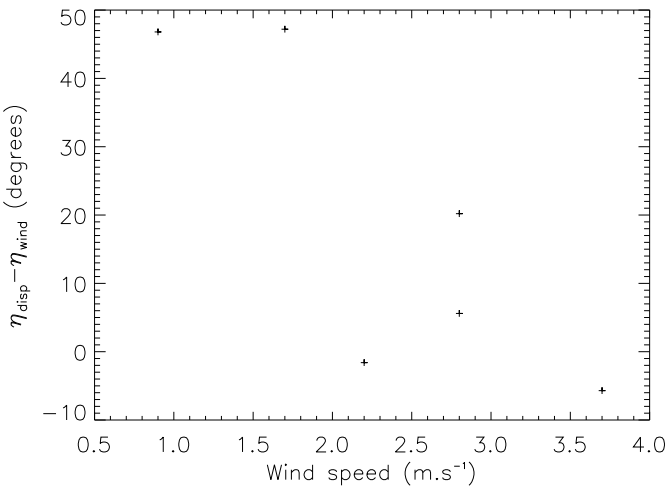

Figure 6.24: Difference $\eta_{disp} - \eta_{wind}$ vs. mean wind speed, obtained from all recording dates in summer 2000.

From this direct comparison of the mean wind angle and the mean wheat displacement angle, a few preliminary conclusions can be drawn. There is no universal easy relation between η_{wind} and η_{disp}. The close proximity of some of the angular values can effectively be interpreted as the direct result of wind forcing on the wheat. However, the motion is in some cases too widely spread about the mean displacement direction to simply be interpreted by the mean wind angle value. In

addition to this, some other angle values clearly show significant differences. The poor correlation between the two parameters shows that the interaction between the wind and the wheat is complex and not appropriately represented by average values. This result could have been expected since the separate study of the wind and of the wheat motion have shown that processes along the mean wind direction and perpendicular to it both have a significant amplitude.

Apart from the good correlation coefficient obtained on July 19^{th}, the values obtained on the other dates are low, showing once more that the motion of wheat is significant both in the x and y direction. The wheat loci of Figure 6.14 constitute a graphic representation of this conclusion. The high correlation obtained on July 19^{th} cannot be explained by exceptional wind conditions since the average wind speed at that date and the turbulence intensities are not significantly different from the other dates. It can only be assumed that the unique combination of the wind conditions on July 19^{th} with the wheat phenological state at that date lead to this specific behaviour of the wheat. It is difficult to make a definite judgement on this point due to the lack of data in similar conditions. Analysis of another 1 minute subset at the same date would be useful, but was not conducted here since it would not change the main conclusions presented below.

Variation of the turbulence intensities does not have a significant impact on the mean wheat displacement. This does not mean that the turbulent nature of the wind is not responsible for the spread in wheat motion. i_u and i_v are by definition equal respectively to the standard deviations of the longitudinal and transversal components of the wind, normalised by the mean longitudinal wind speed. So for an approximately constant value of i_u and i_u, a higher value of the longitudinal wind component is related to a higher standard deviation of the wind components. And this higher spread in the longitudinal and transversal wind components translates into a higher spread in the wheat displacement. So it is because the wind is turbulent at the wheat height that the wheat moves in a widely spread manner.

Conclusions on the study of the relation between mean values of the wind and the wheat motion

The total amplitude of the wheat motion is clearly related to the wind speed, and this relation was used to express the expected wheat total amplitude as a function of the wind speed. It was pointed out that the confidence attributed to the linear relation would be significantly increased by a higher number of independent measurements. The good relation between motion amplitude and wind speed is simply a translation of the direct causal relationship between the two parameters. However, this section also showed that the wind direction and the wheat direction of displacement are not closely related, especially in low wind conditions. Other parameters, such as the correlation coefficient of the (x,y) wheat coordinates, are not clearly related to the wind speed.

The main conclusion here is that it is difficult to derive clear relationships between the wind and the wheat motion, other than between the mean wheat amplitude and the mean wind speed. This shows the complexity of the relations at the canopy level, which will be further highlighted in the next section.

6.6.2 Simultaneous time variations

Figure 6.25 shows the simultaneous variation with time of the wind measured at wheat canopy height and of the wheat head motion, for target 1 on July 19^{th}. Figure 6.25(a) and 6.25(b) respectively show the variation of the wheat x and y coordinates relative to their mean value, in parallel with the wind velocity x and y components (w_x and w_y). Figure 6.25(c) shows the time variation of the total wheat amplitude and of the total wind speed w_{speed}.

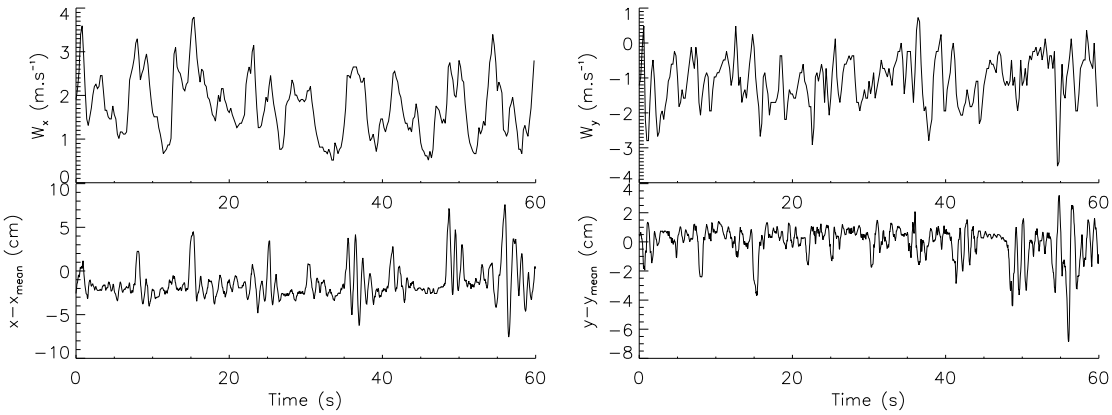

(a) $x - x_{mean}$ and w_x

(b) $y - y_{mean}$ and w_y

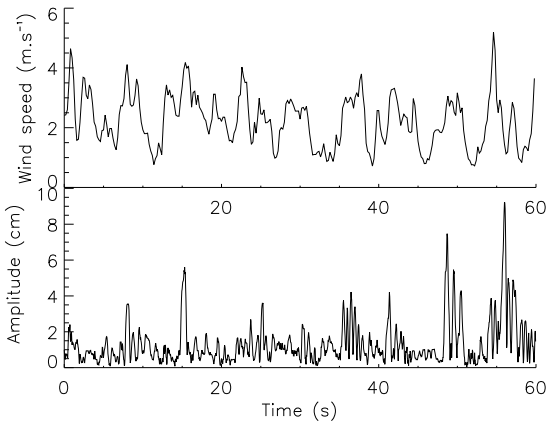

(c) Total amplitude and w_{speed}

Figure 6.25: Time variation of the wind longitudinal and transversal components and of the wind speed obtained from triad 3 at wheat canopy height on July 19^{th} 2000. Simultaneous time variation of the x and y coordinates and of the total displacement relative to the mean of target 1 (wheat head) at the same date and time.

Some peaks of high wind measured at the triad occur simultaneously with peaks of motion. For example, at time $t = 15s$, a wind gust is responsible for the displacement of the wheat head in both the x and y directions, and appears in the total amplitude. So, at least qualitatively, the causal relation between wind and wheat

motion is directly observed in some cases. However, the speed of the displacements does not always comply with the speed of the wind at the same time. A good illustration of this feature is present on Figure 6.25(a): the wind gust at time $t = 15s$ is stronger than at time $t = 37s$, but the oscillation of the target in the x direction is bigger in the latter case. The case above is derived from data collected on July 19^{th}, but the analysis of similar time variations for other targets and other dates lead to the same conclusions.

The analyses of the previous sections can give some useful indications about the apparent poor agreement described above. In particular, it was shown in the autocorrelation analysis of the wind data (section 6.4.2) that, in the case of low wind, the velocity recorded at the DVA triad is not correlated to the wind which influenced directly the wheat elements. This can explain why the time variations in quiet wind period do not correspond well. However this does not explain why the highest wind peaks are not better related to the wheat motion. Table 6.12 showed that the mean wind direction on July 19^{th} is about 30° offset from the x direction. In the experimental procedure, the wheat targets being placed directly in line with the triad x axis, there is a strong possibility that the wind acting on the wheat elements "missed" the triad and was therefore not recorded. So the high variability of the wind direction is probably the main cause of discrepancy between the time variation of the wind and wheat motion data.

A possible way to reduce this effect would be to place the DVA triads closer to the tracked targets, without impeding their free motion or modifying the natural wind conditions they are subject to. This is a suggestion left for future measurement campaigns. The main conclusion from the analysis here is that any relation between the wind variation and the wheat motion should be treated with care because the two data sets, although carefully synchronised, do not necessarily yield the solid relationships that could be expected *a priori*.

6.6.3 Relation between the wind statistics from the weather station and the wheat motion

Section 6.4.4 presented wind speed statistics generated from the weather station data collected in 1996 and 1997. The main conclusions were that the wind conditions are significantly different in the winter and in the summer, as well as during the time of day. These different conditions translate into different wheat motion conditions. The wheat being at its full growth stage in the summer, it is necessary to use summer wind statistics in the following discussion. The aim of this section is to translate the cumulative wind speed probabilities of section 6.4.4 into motion probabilities.

It was shown in section 6.6.1 that the wheat motion amplitude can be linearly related to the mean wind speed. The accuracy of the linear relation given in Equations (6.11) and (6.12), estimated by 80% confidence intervals, is limited to about 5 cm due to the restricted number of points available to generate them. However, Equations (6.11) and (6.12) are used here despite their limited accuracy. The aim of this section is to show the potential of the method which aims to derive motion amplitude statistics from annual wind data.

Equations (6.11) and (6.12) require the average wind speed at canopy height,

and the wind statistics in section 6.4.4 are obtained at 1.85m. The link between the two is provided by Equation (6.8), which relates the expected wind speed at two different heights. The height of the weather station anemometer falls into the limit of validity of Equation (6.8) (inferior to 2 m). The wheat motion probability distributions are generated by first translating the weather station wind speeds into wheat height speeds with Equation (6.8), then by calculating the wheat motion amplitudes associated to these wind conditions from Equations (6.11) and (6.12), and finally by generating the cumulative probability functions of wheat amplitude in the x and y directions. The weather station wind data used for that purpose corresponds to the summer months, and is divided into four categories depending on the time of day (similarly to the analysis already presented in section 6.4.4). The results are plotted in Figure 6.26.

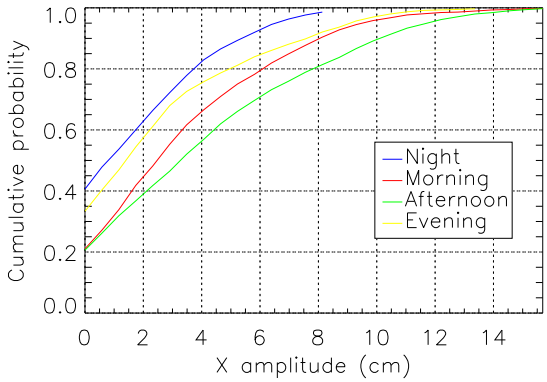

(a) Wheat amplitude in the x direction, based on 1996 wind data

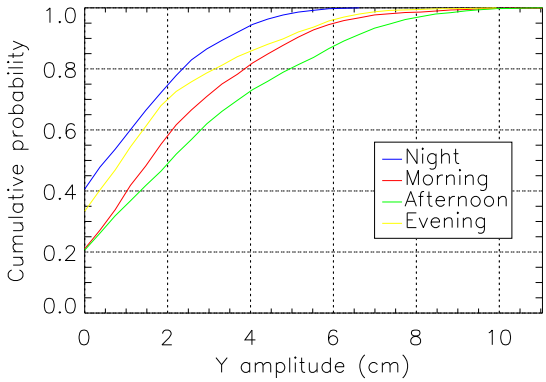

(b) Wheat amplitude in the y direction, based on 1996 wind data

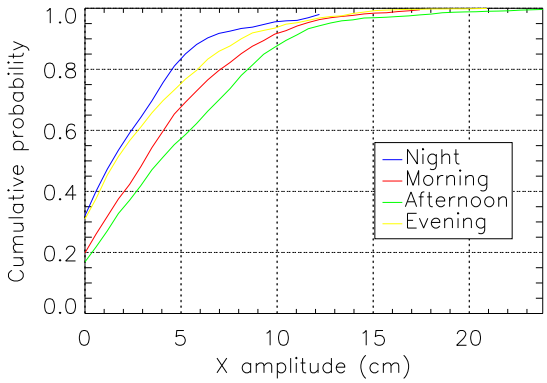

(c) Wheat amplitude in the x direction, based on 1997 wind data

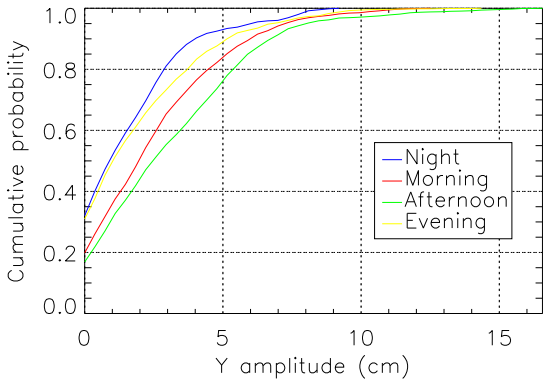

(d) Wheat amplitude in the y direction, based on 1997 wind data

Figure 6.26: Cumulative probability functions of the wheat amplitude in the x and y directions, calculated from the summer 1996 and 1997 weather station data, and divided into night, morning, afternoon, evening categories

The first feature to notice on the graphs is that there is a non-zero probability that the wheat does not move. This is due to the fact that the linear relations

between wind speed and wheat amplitude infer a non-zero velocity at which the amplitudes in the x and y directions are null. Physically, it is understandable that there is a minimum velocity required to actuate the wheat plants.

In Figure 6.26(a), the probability that the wheat amplitude is inferior to 8 cm in the afternoon is about 80%. The same probability in the night is reached at only 4 cm, showing that the wheat is expected to move significantly less in the night compared to the afternoon. The morning and evening cases are intermediate between these two extremes. A similar difference of about 4 cm between the night and afternoon cases at the 80% probability is also found on Figure 6.26(c), showing the consistency of the analysis between different years. The equivalent amplitude difference in the y direction is about 2.5 cm, which points out that the wheat motion in the mean cross-wind direction is less affected than in the mean wind direction.

The value $x_{amp-max}$ at which there is a 100% probability that the wheat amplitude is inferior to $x_{amp-max}$ is about 15 cm on Figure 6.26(a) and 20 cm on Figure 6.26(c). These values set the limits of the motion amplitude to expect from a wheat crop.

The analysis presented in this section is interesting because it can be used to relate the average weather conditions in a particular region to the coherence which can be expected from a wheat field in that region. In weather conditions typical of South-East England, it was shown that the motion of wheat to expect at night is inferior to that of the afternoon, and consequently sets some different expected coherence levels, depending on the time of day the SAR data are recorded. A quantitative analysis based on this conclusion will be presented in the next chapter, but it is acknowledged in this section that weather data recorded independently over long time periods provides valuable information about crop motion statistics and therefore about the coherence.

6.6.4 Calculation of the wheat deflection under a static load

It was pointed out in section 4.9 that the motion measurement system can only retrieve the position of the top part of the wheat canopy, and not inside the vegetation. The wheat leaves within the canopy are not directly in view of the video cameras, so their motion cannot be precisely measured, except at an early growth stage, when the wheat is in a leafy state. However, the motion of the wheat stalk can be directly linked to that of the head by a simple model presented in Appendix G and outlined here. The wheat is considered as a vertical cylindrical beam (in its initial position), fixed at its base and subject to a distributed force along the beam, representing the wind load. The force applied to the beam is considered constant here, since the parameter of interest here is the shape of the deflected wheat. The parameters entering in the calculation are:

- The geometrical parameters of the wheat, namely the stalk and wheat head lengths and radii.
- The mass of the wheat stalk and head.
- The modulus of elasticity of the stalk and the head, which represents the bending properties of the plant.

- The wind force distribution associated with the wind velocity along the beam.

The geometry and mass of the wheat elements can be directly measured on plants. The modulus of elasticity E depends on the properties of the wheat material. For common materials, there are published tables of E which can be used directly. However, no such table exists for wheat, as the theory of structural dynamics is usually applied to civil engineering applications. Appendix G shows how a value of E is chosen by comparing wheat to other materials. The wind force is calculated from basic aerodynamics theory. The drag acting on a cylinder is used to represent the force on the wheat plant as a function of the velocity. The distribution of the force long the beam is related to the distribution of the wind velocity within the wheat canopy. Such a wind distribution was published in [45] and shown to increase approximately linearly with height.

The knowledge of the wheat deflection allows to relate the displacement of the wheat head obtained from the measurements to that of the wheat stalk, which is not directly observed. This is important because the motion of the stalk is also required in the coherence model. With the numerical parameters given and justified in Appendix G, the deflection of the stalk due to a constant wind speed of 2 $m.s^{-1}$ is shown in Figure 6.27.

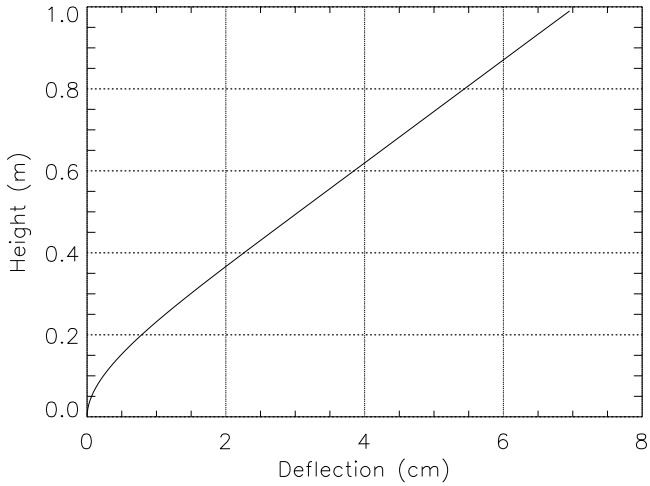

Figure 6.27: Modelled deflection of the wheat stalk subject to a wind speed of 2 $m.s^{-1}$ at the wheat height (0.8 m).

The model predicts a stalk deflection of about 5.3 cm at a height of 0.8 m. This value is to compare to the linear relation given in Equation (6.11), relating the average wind speed to the total wheat amplitude. At 2 $m.s^{-1}$, the linear relation predicts a total amplitude of 7.4 cm. The values are in good agreement, bearing in mind that the 5.3 cm deflection is not exactly the total wheat amplitude: in the real case, the wheat moves along the x direction mainly in the positive direction, but also occasionally in the negative direction when the wind load is decreases or approaches zero. The analytic expression of the stalk deflection can be used in conjunction with the wheat head motion measurements to provide a quantitative estimate of the positions of the stalk. Such information will be used in Chapter 7 for coherence modelling purposes.

Finally, Figure 6.27 shows that most of the strain inside the wheat stalk occurs at its basis, i.e. at heights inferior to 0.2 m. Above this limit, the stalk keeps a nearly linear shape. The strain being concentrated at the basis of the stalk, it explains the problem of lodging, which is the breakage of the wheat stalk in high wind conditions. Breakage usually occurs at the basis of the wheat plant, and this naturally observed features relates well to the fact that most of the stalk deformation predicted by the model is found at the foot of the plant.

6.7 Conclusion

6.7.1 Summary of the data analysis

The analysis of the wind and wheat motion data covered a wide range of issues which need to be summarised here. The wind velocity components were measured at canopy height and above, and round red labels placed on the upper part of the wheat canopy were filmed with the two video cameras, giving their three-dimensional position. The analysis of the wind data alone showed the high variability of the wind conditions, both on spatial and temporal scales. The motion of wheat, which results directly from the wind, is in turn highly variable in time and spatially. The analysis presented in this chapter has shown the complexity of the relation between the two parameters, linked to the complexity of the turbulent wind at canopy level and of its interactions with the wheat.

Because of this complexity, the strongest relations between wind and wheat motion were found through the use of average values derived from the one minute sequences of processed video data. The mean wind speed is well correlated to the motion amplitude. It is also because of the complexity of the detailed relations between the two data sets that it is chosen to use the statistical approach to describe the motion of wheat and its amplitude. The measured wheat loci are transformed to probability functions defining the position of a scatterer along the radar look direction, and the probability of the wheat amplitude during the growth season is obtained from summer wind statistics. As much as one would like to have a more detailed knowledge of the wheat motion and its direct dependence on wind, the data measured do not provide such information and therefore should not be used for that purpose. However, the measurements presented in this section answered the objectives of the research stated in section 2.5.2:

- *Objective 1*: a database of wheat motion and wind velocity was created and is made available on the CD attached to this report. Objective 1 in section 2.5.2 referred to motion of crops in general and the present study focused on wheat. However, the methodology defined here can in principle be applied to other crops.

- *Objective 2*: the measurement system described in Chapters 4 and 5 was applied and shown to function satisfactorily.

- *Objective 3*: The measurements were used in this chapter to quantify the relationships between wheat motion and wind velocity.

The last objective defined in section 2.5.2 is the subject of the next chapter. It will be based on the properties described in this chapter, in particular on the wheat motion amplitudes, the motion distribution along the radar look direction, and on the spatial correlation of the wheat movement within an area defined in section 6.5.2.

6.7.2 Potential developments of the data acquisition and analysis

The acquisition and analysis of the data presented here are not at a final stage of their development, and have opened several areas for improvements or further studies which are discussed in this section.

Wind data acquisition and analysis

It was shown that more detailed relations between the wheat motion and the wind data could be obtained by reducing the distance between the DVAs and the measured wheat elements. Further measurements should take this into account and try to place the anemometers closer to the measured targets, without impeding their motion or changing the natural wind conditions they are subject to. It is expected that the interactions between the wheat motion and the wind would appears more strongly. With such a knowledge, the data sets could be used to study more accurately the reciprocal effects of turbulent wind and wheat motion. A wheat transfer function could be calculated, which would give a better idea of the mechanical properties of the wheat. It should be noted in passing that such a transfer function was calculated from the current data sets, but is not presented here because it did not yield results easily interpretable or providing new insights into the relationships between wind and wheat motion.

Measuring the wind velocity at different heights and different positions would allow to derive a simplified wind field structure which could be used to estimate wind conditions within a certain volume above the wheat canopy. With an initial set of 4 triads, this aspect was planned to be studied but the failure of some cable connectors did not allow it. Wind data collected on June 6^{th} with a full set of 4 triads suggests that the correlation of the different wind components remains significantly high on short spatial scales. A more complete data set would help to quantify this qualitative statement.

From the point of view of the wind data acquisition, several improvements can be suggested. The first obvious one is to use reliable hardware which is unlikely to be altered or broken in field use. This concerns primarily the Binder connectors, which appear to be the weak point of the wind data measurement hardware. From the experience gained this year, it is suggested that measurements should be made as often as possible, in order to limit the impact of unexpected hardware problems which can cause the data to be partially or totally lost. Another potential improvement is to integrate the wind data acquisition system into a more portable format, for example by using a portable computer and more compact interface cards. At the moment, the system requires a power generator and a desktop computer, which

is therefore fairly heavy to transport and fragile to manipulate.

Wheat motion data acquisition and analysis

Tracking the red labels placed on the wheat elements can be fairly difficult in some cases, especially in high wind conditions and by direct obstruction of the target by another object in the foreground. There is no direct way to solve the obstruction problem, other than choosing carefully the relative position of the labels to track and the cameras. The occasional blurring in the image of fast-moving targets causes the tracking to be more difficult. This difficulty can be significantly overcome by using the un-interleaving and filtering techniques presented in section 4.6.8. Tested have been conducted with these techniques and have shown to significantly improve the tracking. In fact, some targets which could not be tracked accurately prior to the use of the image processing techniques of section 4.6.8 could be successfully followed after application of the different filters. For that reason, it is suggested that future measurement campaigns use more systematically these image pre-processing techniques.

The drawback of this suggestion, however, is that it is time consuming and impinges on the short processing time requirement set for the system. In fact, it was pointed out earlier that processing the entirety of the video tapes for all recording dates would require a long time which was not available in the stringent schedule of the project. In that respect, a potential further development of the measurement system is to use a direct 'real-time' transfer from the video cameras to a computer, without the 2 Gbyte limit on the maximum file size. The Digital 8 format is not suitable to achieve this, but new digital video formats such as DV have opened this possibility. The hardware is still relatively new and therefore expensive, but its price is likely to decrease in the future. The direct video transfer of the video data to the computer would reduce significantly the pre-processing time: in its current configuration the data download from the Digital 8 tapes to the computer, in blocks of 2 Gbytes, is a significant lengthy task which would be obsolete with a direct video data transfer system.

On the data analysis side, it is suggested that more measurements should be made during the growth period, from March to June. It is interesting to assess the effect of the wheat phenological state on the motion of wheat, as it may yield specific behaviours which affect the coherence.

The measurements on wheat have shown that the methodology applied in the research can be used successfully, but the system should be applicable to other crops. The wind data measurements system is not affected by the crop type, so it can be used in its current form for different crops. For high crops like corn, placing the DVA triads above the plant tops may cause practical difficulties but these do not constitute major problems. The labels to track on other crops should be placed on all visible parts of the canopy. The analysis of the motion of other crops could lead to some valuable insights potentially useful to assess the potential of crop classification from SAR data.

Chapter 7

Discussion

The measurements of wind data and wheat motion provide some quantitative insights into the mechanisms which affect the coherence magnitude. This chapter moves on to use these insights to estimate the coherence expected from a wheat field. The impact of several parameters is assessed, based on the measurements presented in the previous chapter and on the model introduced in Chapter 3. Section 7.1 shows how the measurements of wheat motion are taken into account to modify the initial coherence model. Then sections 7.2 to 7.5 use the model to study the impact of a number of parameters on the expected coherence from a wheat field. The parameters are the radar resolution, the wavelength, the angles defining the radar look direction, the repeat-time between the two radar passes. The variability of the coherence due to the variability of the wind conditions is assessed in section 7.6. Finally the variation of coherence through the entire growth season is modelled and compared to coherence estimates from ERS data in section 7.7. Conclusions on the use of coherence for wheat monitoring and a critical discussion of the strengths and weaknesses of the approach presented in this report follow, in sections 7.8 and 7.9.

7.1 Lessons learned from the measurements: improvements on the initial coherence model

The measurements presented in Chapter 6 have shown that the wheat heads can be considered to move coherently over a certain area defined by the correlation distances d_{c_x} and d_{c_y} (see section 6.5.2). This area of coherent motion defines the extent over which the concept of "equivalent scatterer", at the basis of the coherence model of Chapter 3, is valid. The correlation distances were shown to be of the order of 0.5 m, so a single equivalent scatterer cannot be used to represent the motion of a given type of scatterer over the entire radar ground resolution cell, which extends over several metres. For this reason, the initial coherence model needs to be modified accordingly, to account for the existence of several sub-areas of coherent motion in each radar pixel.

In addition to this, it was shown in section 6.5 how the loci of wheat motion are translated into a probability of displacement along the radar look direction. The

inclusion of these probability distributions is also discussed in this section. Finally, the assumptions at the basis of the coherence model outputs to be presented in the remainder of the chapter are also summarised.

7.1.1 Inclusion of several equivalent scatterers representing the cells of coherent motion

From the analysis of section 6.5.2, the area of coherent wheat motion is assumed here to be $d_c^2 = 0.5^2 = 0.25m^2 = A_c$. It is approximately the value obtained on average from the measurements. The area A_c in the ground resolution cell contains scatterers which are assumed to move coherently, and therefore can be represented by the motion of an equivalent scatterer. Within one of these cells of coherent motion there can be several types of scatterers (e.g. leaves, stalks, ...) having a specific motion, but all scatterers of the same type inside a single cell of size A_c are assumed to move as a single equivalent scatterer.

For a ground resolution cell of size $r_g.r_a$, where r_g and r_a are the ground range and azimuth resolutions respectively, the number of coherent motion cells is:

$$N = \frac{r_g.r_a}{A_c} = \frac{r_g.r_a}{d_c^2} \tag{7.1}$$

The electric field from the static part of the scene is unchanged and remains:

$$V_s = a.\exp(j\varphi_s) \tag{7.2}$$

where a is the amplitude of the static component, obtained from the backscatter contribution of the surface. In the case of a single equivalent scatterer described in section 3.4, the dynamic contribution was assumed to have an amplitude proportional to the backscatter intensity from the vegetation and a phase related to the motion of the scatterers. With N cells of coherent motion, the contribution of the dynamic component is here modelled as the phasor addition of N independent contributions, each of them adding to the total phase deviation due to the motion of the scatterers. The phase deviation from each cell k is noted θ_k.

Let P_v be the total power backscattered from the vegetation. All cells of coherent motion are assumed to be independent from each other and to be defined with the same type, density, and orientation of scattering elements. Therefore the contribution to the total power from each of them is identical and equals P_v/N. So the amplitude of the electric field from a single cell is proportional to $\sqrt{P_v/N}$. The constant of proportionality κ depends on the radar parameters introduced in the radar equation (Equation(2.1)). In the remainder of this discussion, it is ignored because the coherence to be calculated is a normalised coefficient, and consequently the value of κ does not influence the estimates. If b denotes the amplitude of the dynamic component when a single equivalent scatterer is used (as originally described in section 3.4), then the dynamic component with N cells of coherent motion is written:

$$V_d = \sum_{i=1}^{N} \frac{b}{\sqrt{N}} \exp\left[j\left(\varphi_s + \sum_{k=1}^{i} \theta_k\right)\right] \tag{7.3}$$

Note that Equation (7.3) shows that each contribution from a cell k is added to the phase resulting from the addition of the first $k-1$ elements, to account for the fact that each cell is responsible for an increase of the phase noise due to the independent motion of its scatterers. The complex value V_d represents the weather dependence of a single type of scatterer in the ground resolution cell. In the case of vegetation, there are several types of scatterers, so more than one dynamic component needs to be added to the total electric field. Their definition is identical to that of Equation (7.3).

The description here is not fundamentally different from that of section 3.4, where the entire radar ground resolution cell was represented by a single equivalent scatterer. It is simply an extension to the case where the vegetation elements are grouped into smaller areas of coherent motion, each of them being represented by an equivalent scatterer. The concept of an equivalent scatterer is more valid on an area of smaller dimensions than on the entire radar resolution cell, where the motion of vegetation elements separated by several metres is clearly decorrelated. So the approach here is an important extension to the model because it relates more closely to the case of real vegetation. In addition to this, it allows to study the influence of the resolution of the SAR on the coherence (see section 7.2).

The price to pay for this division into N individual contributions for each type of scatterer in the vegetation is on the computation time required by the model. For a ground resolution of 25x5 metres (typical of the ERS satellites) and an area $A_c = 0.25m^2$, there are 500 individual cells of coherent motion in a single pixel. With 1000 pixels being simulated for a single pass of the radar, and typically 2 to 3 independent dynamic components to account for the motion of the different scatterer types in the vegetation layer, the total number of iterations required by the simulation increases rapidly. The most significant task in terms of computing time in each iteration of the simulation is the generation of the 1000 values of slant range displacement following the true distribution obtained from the measurements (an example of this true distribution is shown in Figure 6.15). The slant range values are obtained by using an algorithm based on the rejection method presented in [56]. There is not a direct way to reduce the computing time significantly without risking to compromise the quality of the result. However, a possible alternative is to assume that the distribution of the slant range displacements can be approximated by a Gaussian distribution. This would reduce significantly the computing time required for the simulations, since the normally distributed sets of points are easily generated in the IDL language.

However, the use of a normal distribution was identified in Chapter 2 as one of the possible limitations of the current coherent models. It is necessary to assess the impact of replacing the true slant range distribution by a Gaussian distribution, before using it with confidence. This assessment is the subject of the following section.

7.1.2 Distribution of the slant range displacement

Figure 7.1 shows the distribution of the displacement in the slant range direction obtained from the measurements of the wheat head motion on August 2^{nd}, for 4

different targets. The procedure used to generate these distributions was detailed in section 6.5.1. On the graphs, the dotted lines represent the Gaussian distribution whose mean μ_g and standard deviation σ_g are adjusted to best fit the true distribution. The radar incidence angle used to generate the true distribution is 25°.

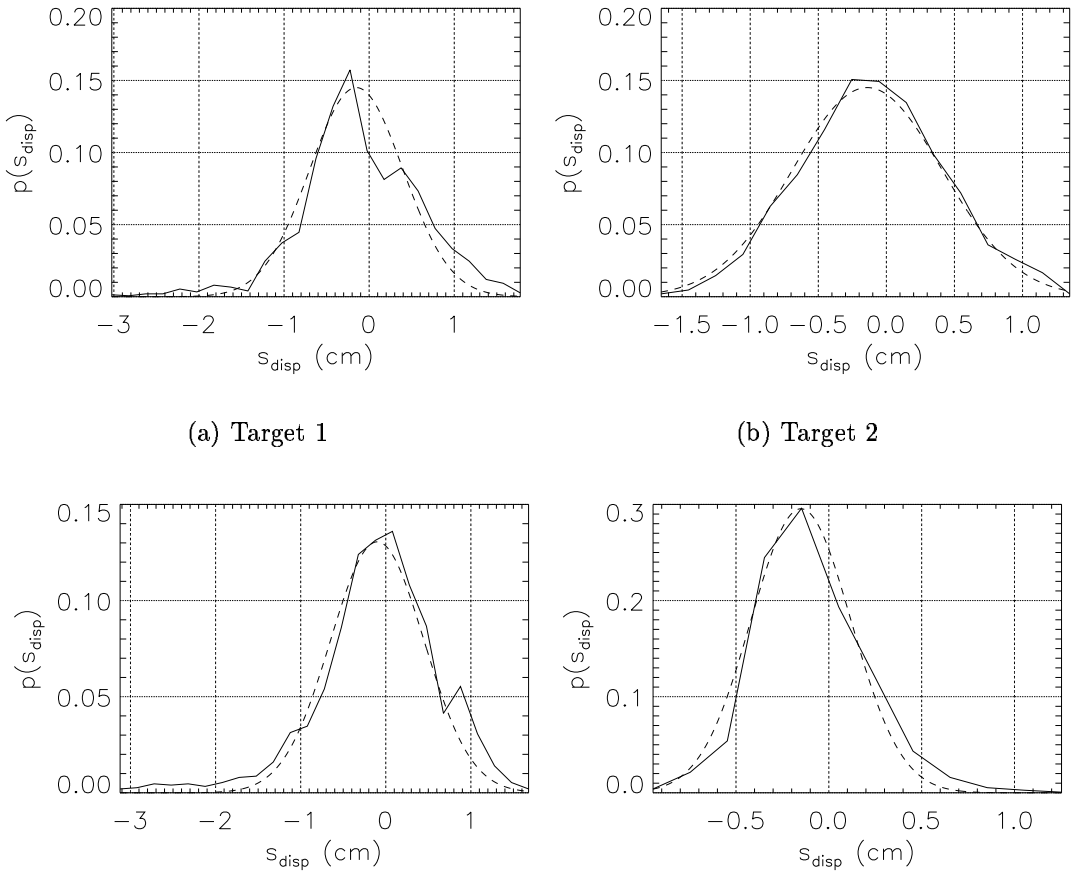

(a) Target 1

(b) Target 2

(c) Target 3

(d) Target 4

Figure 7.1: Probability distribution of the displacement in slant range direction of the wheat head, calculated from 4 targets with data collected on August 2^{nd} (solid line), and Gaussian distribution (dotted line) providing best fit.

The shape of the distributions is variable between targets because each wheat plant experiences a specific motion. It is also worth mentioning that distributions obtained from data collected on other dates are similar in shape to those presented here. Their magnitude and spread about the mean is variable, depending on the wind conditions at the recording date. The mean and standard deviation of the Gaussian distribution are determined numerically with a standard data fitting algorithm available in the IDL language, which minimises the root mean square error ε between the Gaussian and true distributions. For the 4 distributions shown in Figure 7.1, the mean and standard deviation of the fitted Gaussian distributions are given in Table 7.1.

Target number	σ_g (cm)	μ_g (cm)	ε
1	0.61	-0.13	$1.3\ 10^{-2}$
2	0.53	-0.11	$4.1\ 10^{-3}$
3	0.58	-0.03	$7.6\ 10^{-3}$
4	0.26	-0.14	$1.9\ 10^{-2}$

Table 7.1: Mean and standard deviation of the Gaussian distribution fitting the true distributions shown in Figure 7.1, and root mean square error of the fit

Figures 7.1(a) and 7.1(c) in particular show that the true distributions (i.e. the distributions derived from the measurements) can contain some occasional fluctuations which are not accounted for in the Gaussian distribution. Therefore the value of ε cannot be used as a reliable goodness of fit indicator and, in order to really assess if the Gaussian distribution is suitable to represent the true wheat motion, the estimates from the coherence model using the true and Gaussian distributions were calculated in a simplified case. The electric field in the coherence model was defined with a single dynamic component of amplitude equal to the amplitude of the static component, and with a single equivalent scatterer representing the motion of the entire ground resolution cell. The wavelength is $\lambda = 5.66$ cm (ERS value). The mean and standard deviation in slant range of the Gaussian distributions are translated into their equivalent values in phase ($\varphi = (4\pi/\lambda)s$). Table 7.2 shows the coherence estimates obtained from this simplified case, with the 4 true distributions shown in Figure 7.1 and with their associated Gaussian distribution.

Target number	γ_{true}	γ_g
1	0.69	0.72
2	0.74	0.77
3	0.71	0.74
4	0.89	0.93

Table 7.2: Coherence model outputs with the phase of the dynamic component based on the true slant range distributions of Figure 7.1 and the fitted Gaussian distributions defined in Table 7.1

The estimates obtained with the Gaussian distributions are consistently higher than their corresponding values computed from the true distributions. However, the difference between the two estimates is small (≈ 0.03 on average). This shows that the Gaussian approximation of the true distribution can be used in the coherence model and will yield reliable estimates. Using the Gaussian approximation significantly reduces the computation time, and is therefore very valuable in this respect. The analysis presented here focused on four targets only, but similar results with data collected at other dates were obtained. They are not presented here because the main purpose of the comparison above is to show the validity of Gaussian approximation, rather than making a detailed comparative analysis in every single

case. The results shown here are representative of the other data sets.

The result presented above is important because the possible difference between the true displacement distribution and the normal distribution is one of the reasons given in Chapter 2 to justify the need for motion measurements. The Gaussian distribution is a good approximation of the distribution of the wheat head displacement in the slant range direction. This does not mean that the motion measurements were not useful because they are still required to determine the extent of the displacement, i.e. the mean and standard deviation of the Gaussian distribution.

7.1.3 Inputs to the coherence models used in the remainder of the chapter

RT2 estimates

The coherence estimates to be presented in the following sections of the chapter require the estimation of the contributions to the total backscattered power from the different scattering mechanisms. Chapter 3 showed how the RT2 backscatter model can be used for this purpose, but it also showed that RT2 requires a precise definition of the vegetation in terms of the geometry, orientation and density of its scatterers. It was explained in section 3.6 that no wheat phenotypic data were collected during the research, so external sources of data will be used:

- Inputs to the MIMICS backscatter model are given in [1]. They represent a full grown wheat crop and can be used in the RT2 model. These inputs were already used in section 3.3 to simulate the backscatter from a wheat field. The numerical values of the different parameters derived from [1] and used here in RT2 are given in Appendix A.4. However, the wheat simulated with the parameters given in [1] does not include the presence of wheat heads.

- In [51], the RT2 model is used to simulate the backscatter from a wheat field at different growth stages. The results are based on phenotypic data collected in The Netherlands between 1993 and 1996. Although the wheat data are not given in [51], there is a graph showing the time variation, from April to August, of the total backscatter and of the several contributions from the different scattering mechanisms. Numerical values taken from this graph are reproduced in Table 7.3.

The empty cells in Table 7.3 correspond to values below -30 dB, which do not explicitly appear on the graph shown in [51]. Their exact value is not required because they correspond to cases of very low backscatter contributions which therefore do not affect the coherence outputs.

The two data sources used in this chapter are complementary because the first one does not include the presence of wheat heads in its modelling but allows any parameter of interest to be varied, whereas the second data source does include wheat heads but corresponds to a fixed radar configuration (wavelength $\lambda = 5.67cm$ and incidence angle $\theta = 23°$, the ERS values). Depending on which particular aspect is the focus of attention in the discussion to follow, the most suitable of the two data sources will be chosen.

Point number	Date	σ^0_{total} (dB)	$\sigma^0_{stalks+leaves}$ (dB)	$\sigma^0_{stalk/ground}$ (dB)	σ^0_{heads} (dB)	σ^0_{ground} (dB)
1	10^{th} April	-8.3				-8.3
2	20^{th} April	-8.6				-8.6
3	1^{st} May	-8.9	-18.0	-11.1		-14.4
4	10^{th} May	-9.1	-18.6	-11.0		-16.2
5	20^{th} May	-10.3	-18.1	-12.0		-19.2
6	1^{st} June	-11.7	-19.4	-13.8		-22.9
7	10^{th} June	-14.5	-23.5	-20.5	-23.1	
8	20^{th} June	-19.2	-29.2	-25.4	-21.5	
9	1^{st} July	-18.9	-29.8	-24.4	-21.5	
10	10^{th} July	-18.2	-29.5	-23.5	-21.5	
11	20^{th} July	-17.0	-29.5	-20.0	-22.0	-27.9
12	1^{st} August	-14.3	-24.9	-16.6	-23.8	-23.2
13	10^{th} August	-11.7	-30.0	-14.7	-26.6	-16.0

Table 7.3: Time variation of the backscatter coefficient and of the contributions from the different scattering mechanisms obtained from a wheat field in the Netherlands (values read from a figure given in [51])

Phase distributions

In the coherence model outputs, four contributions are used to simulate the total electric field from a given pixel. The backscatter contribution from the surface relates to the static component of the electric field, and the three dynamic components of the model are identified as the backscatter contributions from the leaves+stalks (direct scattering), the wheat heads (direct scattering), and the stalk/ground "double bounce" scattering. The motion measurements made on the wheat heads are directly translated to a phase distribution as detailed previously, by multiplying the slant range displacements by $4\pi/\lambda$. However, the motion of the stalks and of the leaves has not been directly measured and therefore needs to be estimated. For that purpose, it is convenient to use the wheat deflection model introduced in section 6.6.4 and fully derived in Appendix G.

The wheat stalk does not move at all at its base and, at its upper part, has the same motion as the wheat head. It is chosen to represent its motion by the value of its average displacement along the stalk. The shape of the stalk deflection is represented by a function $\psi_s(x)$ which is the displacement of the stalk from the initial rest (vertical) position at a certain height x. The expression of $\psi_s(x)$ is derived in Appendix G and reproduced here:

$$\psi_s(x) = \frac{q_{0s}}{120 E_s I_s L_s^2} \left[(L_s - x)^6 + 6 L_s^5 x - L_s^6 \right] \tag{7.4}$$

L_s is the total length of the stalk, and q_{0s}, E_s and I_s relate to the wind forcing and the mechanical and geometrical properties of the stalk. The average displacement D_s of the stalk is:

$$D_s = \frac{1}{L_s}\int_0^{L_s} \psi_s(x)dx = \frac{q_{0s}}{120E_sI_s}\frac{15L_s^4}{7} \tag{7.5}$$

where the term on the right is obtained from direct integration of $\psi_s(x)$. The ratio between the average position D_s and the displacement at the top of the stalk is:

$$\frac{D_s}{\psi_s(L_s)} = \frac{D_s}{\frac{q_{0s}}{120E_sI_s}5L_s^4} = \frac{3}{7} \approx 0.43 \tag{7.6}$$

The displacement at the top of the stalk is that of the wheat head to a good approximation because the latter is physically related to the former. Consequently the motion of the stalk is assumed to be a scaled version of the measured motion of the wheat head, the scaling factor being the value 3/7 derived above from the mean stalk position. The distribution of the stalk position in the slant range direction is therefore based the wheat head distribution, with the standard deviation σ_{stalk} taking the value $(3/7)\sigma_{heads}$. For double scattering, a slant range displacement of the stalk dr modifies the travel path of the radar wave by the same displacement dr, so the phase of the radar signal is affected by the quantity $(2\pi/\lambda)dr$. So in the coherence model, the distribution assumed for the phase of the dynamic component representing the double scattering from the stalks is:

$$\sigma_{\varphi_{stalks}} = \frac{2\pi}{\lambda}\sigma_{stalk} = \frac{3}{7}\frac{2\pi}{\lambda}\sigma_{heads} = 0.5 * \frac{3}{7}\sigma_{\varphi_{heads}} \tag{7.7}$$

The direct scattering originates from the stalks, but also the leaves. They lie within the wheat canopy and for that reason their motion was not directly recorded. Because the leaves are physically attached to the stalk, their motion is assumed to be identical. In reality, it is likely that the leaves follow the motion of the stalk they are attached to, but also have their own motion adding to it. It is this additional motion which is ignored here. From visual observations, the main motion of the leaves seems to be the motion of their stalk, and the extra motion they experience is in rotation about their principle axis, and sometimes in folding in two in high wind conditions. The standard deviation of the slant range displacement of the wheat leaves, σ_{leaves}, is assumed here to be identical to σ_{stalks}. A displacement dr of the leaves modifies the travel path of the directly scattered radar wave by an amount $2dr$, so the phase of the dynamic component of the coherence model related to the direct scattering from the leaves and stalks is assumed here to have standard deviation:

$$\sigma_{\varphi_{leaves}} = (4\pi/\lambda)\sigma_{leaves} = \frac{3}{7}\frac{4\pi}{\lambda}\sigma_{heads} = \frac{3}{7}\sigma_{\varphi_{heads}} \tag{7.8}$$

The definition of the phase distributions of the stalk/ground double scattering and stalks+leaves direct scattering contributions requires some assumptions which are difficult to check quantitatively. However, the representation of the stalk motion as a scaled version of the head motion is based on the wheat deflection function and seems to be a reasonable approximation. Visual observations support the assumption that the leaves' motion is close to that of the stalk, but the impact of ignoring

their additional motion is difficult to assess. It is decided to make no attempt to guess the exact nature of this extra motion by adding extra terms in the phase distribution. This would add an error equivalent to the inaccuracy already introduced by simply ignoring the extra leaf motion.

In the coherence model, the phase of the 3 dynamic components is generated from the distributions specified above. For each pixel simulated, the 3 phase values are generated independently, which means that the motion of the stalks, the leaves, and the heads is assumed to be independent. In reality, the motion of the 3 elements of the wheat is directly related so it can be expected that there is some dependence between the 3 phases of the dynamic components. The case of real vegetation is likely to yield phase values which are intermediate between total independence (case chosen for the simulation here) and full dependence (the phase of one component determines the phase of the other two). It is decided to simulate the case of total independence in order to make estimates in the worst case, i.e. simulating the lowest coherence to expect. This assumption is discussed in section 7.2, and will be shown to have little impact on the estimates at moderate resolutions.

Notation and convention

In the remainder of this chapter, the following notation and convention are adopted:

- The static component of the electric field is noted $V_s = a \exp j\varphi_s$.
- The dynamic component related to the direct scattering from the leaves and stalks is $V_{d1} = b_1 \exp j\varphi_{d1}$.
- The dynamic component related to the double-bounce scattering from the stalks and ground is $V_{d2} = b_2 \exp j\varphi_{d2}$.
- The dynamic component related to the direct scattering from the wheat heads is $V_{d3} = b_3 \exp j\varphi_{d3}$.
- It is implicit that the distribution of the slant range displacements derived from the measurements concerns the wheat heads. From it, the Gaussian distribution providing the best fit can be calculated and converted to a phase distribution which defines φ_{d3}. The mean and standard deviation of the fitted Gaussian phase distribution are noted $\mu_{\varphi_{d3}}$ and $\sigma_{\varphi_{d3}}$ respectively.
- The mean and standard deviation of φ_{d1} are equal to $(3/7)\mu_{\varphi_{d3}}$ and $(3/7)\sigma_{\varphi_{d3}}$ respectively.
- The mean and standard deviation of φ_{d2} are equal to $0.5 * (3/7)\mu_{\varphi_{d3}}$ and $0.5 * (3/7)\sigma_{\varphi_{d3}}$ respectively.
- The RT2 estimates give the coefficients σ^0 from the several scattering mechanisms in dB. The amplitude of the different components are therefore proportional to $\sqrt{\exp\left(\frac{\ln 10}{10}\sigma^0\right)}$. The constant of proportionality is ignored because it does not affect the coherence (normalised coefficient).

- When the RT2 estimates from Table 7.3 are used, the incidence angle is $\theta = 23°$ and the polarisation is VV.

- The motion correlation distance d_c is set to 0.5 m. The number of cells of coherent motion in the simulated pixel is a function of the resolution (see Equation (7.1)).

The coherence model now has all its necessary inputs: the definition of the amplitude of the different components with RT2, the phase distributions related to the motion of the different elements, and the possibility to include several dynamic terms to account for the presence of more than one equivalent scatterer in the each pixel. The following sections now move on to present the outputs of the coherence model in a series of different conditions.

7.2 Influence of the radar resolution on the coherence

The ground resolution of the SAR is directly linked to the number of cells of coherent motion included to represent each dynamic component of the coherence model, as explained in section 7.1.1. This section considers whether coherence shows a systematic variation as the resolution decreases.

7.2.1 Inputs of the coherence model

The coherence model uses the following inputs:

- The distribution of φ_{d3} is Gaussian and its standard deviation is varied from $\sigma_{\varphi_{d3}} = 0.5$ radian to $\sigma_{\varphi_{d3}} = 3$ radians, covering a wide range of wheat displacements cases obtained in low to high wind conditions.

- The amplitude of the 3 dynamic components is obtained from the RT2 outputs presented in Table 7.3. Three different dates are simulated with points 3 (1^{st} May), 8 (20^{th} June) and 12 (1^{st} August).

- The resolution is varied from 1x1 m to 11x11 m, in increments of 1x1 m.

It should be noted that the coherence simulations on May 1^{st} do include the dynamic component V_{d3}, related to the motion of the wheat heads, even though the wheat heads have not yet emerged at that date. It is possible to do so because the contribution from the wheat head scattering is set to a very low value (-50 dB) and therefore does not influence the results computed by the model.

7.2.2 Coherence model outputs

The outputs of the coherence model obtained from the inputs above are plotted in Figure 7.2.

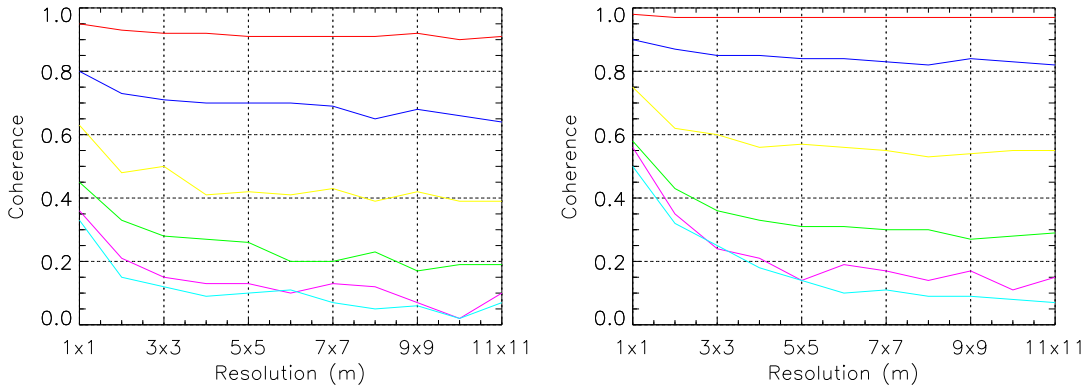

(a) 1^{st} May

(b) 20^{th} June

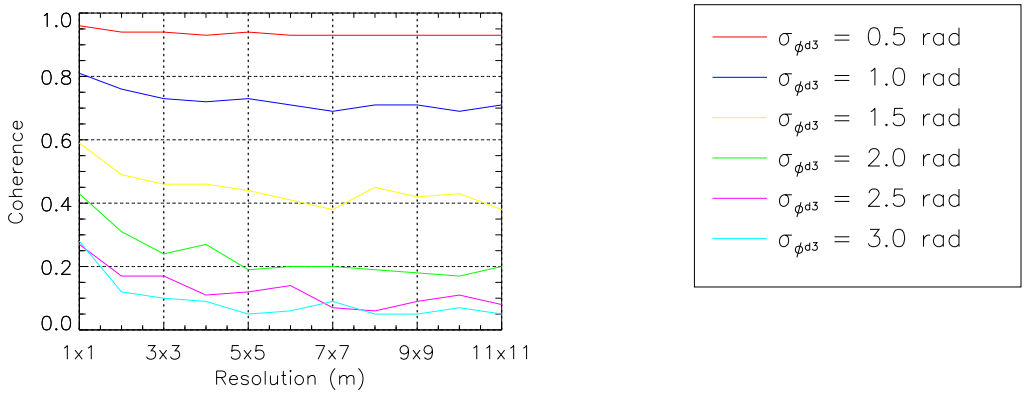

(c) 1^{st} August

Figure 7.2: Variation of the coherence with radar resolution for 3 backscatter conditions

Several features of the plots require discussion here. First, for a given phase standard deviation and resolution, the coherence obtained is different at the 3 different dates. This is related to the fact that the relative amplitude of the 4 different components of the electric field simulated in the model vary between the 3 dates. The variation of coherence with time will be the focus of section 7.7, so it is not discussed further here. It is simply introduced here to show that the features concerning the variation of the coherence with resolution are consistent in different cases of backscatter contributions. The several curves on each graph correspond to different values of phase standard deviation. Cases of small values of $\sigma_{\varphi_{d3}}$ correspond to small motion of the wheat and yield high coherence. The coherence decreases with increasing phase standard deviation, as already shown in section 3.5.

For a given phase standard deviation, there is a decrease of coherence with decreasing resolution. To avoid confusion, 'low' resolution refers here to a ground resolution cell of large dimensions, and vice-versa. So a decrease of the resolution means a variation from small dimensions (1x1 m) to large dimensions (11x11 m).

Qualitatively, a ground resolution cell of large dimensions includes a high number of wheat elements and the resultant complex backscatter should therefore be susceptible to high phase noise due to the motion of these independent elements. For fixed wind conditions, Figure 7.2 shows that the coherence from a low resolution SAR is lower than with higher resolution.

The coherence drops to an asymptotic value which is reached at about 4x4 m, and the drop between 1x1 m and 4x4 m is more pronounced for high values of $\sigma_{\varphi_{d3}}$. When there is very little motion of the wheat (low $\sigma_{\varphi_{d3}}$), the number of cells of independent motion within the pixel does not affect strongly the coherence because it remains high in all cases. In fact, Figure 7.2(b) in particular shows that the coherence obtained for $\sigma_{\varphi_{d3}} = 0.5$ radian is not significantly affected by the size of the ground resolution cell. However, the coherence drop for $\sigma_{\varphi_{d3}} = 3$ radian reaches about 0.4. This is the extreme case, because Figures 7.2(a) and 7.2(c) show a maximum coherence decrease of about 0.2 in the high wheat motion cases.

Current civil spaceborne SAR systems have a resolution of the order of 5x10 metres and the coherence obtained from them therefore corresponds to the asymptotic value shown in Figure 7.2 after 4x4 m. It is expected from the model that the coherence from high resolution SARs, airborne SARs for example, would yield higher coherence than a lower resolution SAR, for a same wheat field imaged in the same weather conditions. To the knowledge of the author, there is not any available data collected in these conditions which could be used to confirm the prediction of the model. Even if the variation of the coherence with resolution presented here can be justified qualitatively, it is not possible to validate it with existing SAR data.

The results presented here have no practical implications on the current spaceborne SAR systems since they do not yet reach the resolution limit under which higher coherence could be observed. However, airborne SARs are more directly concerned by the model predictions: high resolution airborne SARs are expected to yield higher coherence and therefore a higher quality of their interferometry products. In particular, phase noise on the interferograms is expected to be lower, facilitating the phase unwrapping and the generation of good quality DEMs. The use of high resolution SAR data for DEM generation is to be traded-off against other important considerations such as ground coverage and data processing time. For agricultural applications, higher coherence could lead to a higher sensitivity to gradients and consequently a better possibility to differentiate crop types or the growth stage of a single crop. However, this possibility is based on the results above only and ignores the other effects at the origin of the variability of coherence. These effects are discussed in future sections of this chapter.

The number of independent cells generated in the model for a single pixel and a single dynamic component is given by Equation (7.1). In the case used here where the 3 dynamic components of the model are assumed to be independent (see previous section), the total number of independent cells generated for a single pixel of resolution R (m^2) is therefore:

$$N = 3 * (R/d_c^2) \tag{7.9}$$

The simulations presented in Figure 7.2 show that the coherence remains approximately constant after a resolution of about 4x4 m. In the model, this means

that the coherence is not affected when the number of independent cells simulated is higher than a number $N_{4X4} = 192$. If the 3 dynamic components of the model are assumed to be totally dependent, then the factor 3 in Equation (7.9) disappears and the resolution at which the asymptotic value of the coherence is reached would be $R = 192 * d_c^2 \approx 49m^2$ ≈7x7 m. As mentioned in the previous section, the case of real vegetation is likely to yield an intermediate case between total dependence and total independence of the 3 dynamic components. For resolutions of the order of the ERS resolution (25x5 m), the analysis above shows that the coherence outputs of the model are not affected by the assumption of total independence. More care would be required in the justification of the amount of dependence between the 3 dynamic components for simulations in high resolution cases. The simulations presented in the remainder of this chapter deal with a resolution of 25x5 m, so the issue of dependence of the 3 dynamic components is not investigated further. In practice, this dependence issue means that simulations at high resolution require a more in-depth knowledge of the exact motion of the different elements of the wheat. The measurement system presented in Chapter 4 does not provide this detailed knowledge, so the coherence model should be confined to a use at lower resolutions. This shows a limitation of the use of crop motion measurements for coherence modelling, which affects not only the simplified model used in this study, but also in principle other coherent backscatter models.

7.3 Influence of the radar wavelength on the coherence

Wavelength is one of the most important parameters of radar systems used for remote sensing applications because it affects the intensity of the backscatter and also conditions the type of backscattering processes, in particular from a vegetation medium. From the point of view of backscatter intensity only, section 3.2 showed how C-band SARs were most suited for agricultural applications, whereas forestry applications are more efficiently studied with longer wavelengths, at L and P bands. This section focuses on the variation of the coherence with wavelength.

7.3.1 RT2 outputs used in the coherence model

Before running the coherence model, the backscatter contributions from a wheat field at several wavelengths are estimated with RT2, using the wheat parameters from [1] and given in Appendix A.4. The parameter varied in the model is the wavenumber $k = 2\pi/\lambda$, from $k = 41.9m^{-1}$ ($\lambda = 15cm$) to $k = 314.2m^{-1}$ ($\lambda = 2cm$). Note that the surface scattering model used in the RT2 simulations is changed from small perturbation to physical optics at $k = 60m^{-1}$ in order to comply with the validity limits of each surface scattering model for the entire range of wavenumber values.

Figure 7.3 shows the variation of the different scattering contributions with the wavelength. At short wavelengths, the ground contribution is negligible and the scattering originates mainly from the vegetation layer, either directly or through

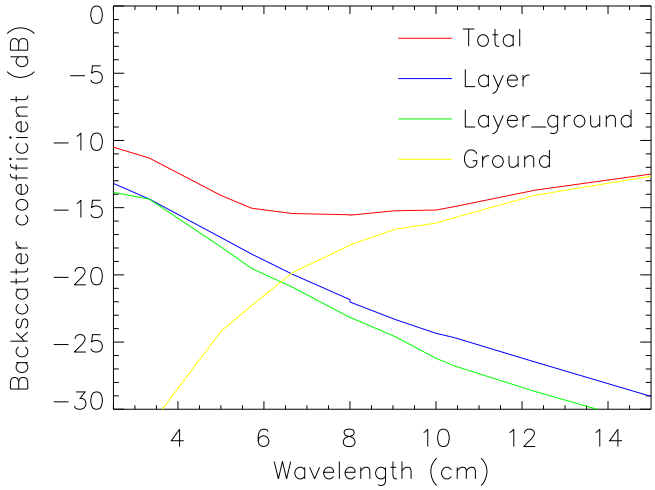

Figure 7.3: Variation of the scattering contributions from a wheat field, estimated with RT2 and based on the wheat parameters given in Appendix A.4

double (ground/vegetation) scattering. These last two scattering contributions are of the same order of magnitude for the entire range of wavelengths displayed. For $\lambda \approx 6.5$ cm, the surface scattering contribution is of the same order of magnitude as the vegetation contributions, and it becomes dominant as λ increases. The long radar wavelengths tend to have a stronger surface scattering contribution because of their higher penetration depth in the vegetation medium. Short wavelength radar waves, at X-band for example, do not penetrate dense vegetation and the backscatter intensity is determined only by the vegetation, and not surface scattering processes. An increase of coherence is therefore expected with increasing wavelength, due to the increase of the static contribution from surface scattering.

7.3.2 Coherence model inputs and outputs

The vegetation is modelled as a single layer containing leaves and stalks. Since the wheat simulated here does not include wheat heads, the motion measurements made early in the season are used. The phase of the dynamic contributions to the total electric field follow the Gaussian distributions derived from the measurements made on 4 targets on June 6^{th}. Table 7.4 gives the standard deviations σ_s and mean μ_s of these distributions of the target displacement in slant range direction, as they are used in the coherence model.

Target number	1	2	3	4
σ_s (cm)	0.13	0.25	0.27	0.14
μ_s (cm)	-0.30	-0.18	-0.13	-0.11

Table 7.4: Mean and standard deviation of the Gaussian distribution fitting the true distributions obtained from measurements made on June 6^{th}, and used in the coherence simulations

Note that the phase standard deviations derived from the motion of targets 1

and 4 are of the same order of magnitude, but target 2 and 3 were subject to a larger motion amplitude because they yield higher standard deviations. This shows the variability of the motion in the wheat field, already pointed out in Chapter 6. It provides here an interesting case because the variation of the coherence with wavelength can be analysed in different motion conditions. Comparison with other targets at other dates shows that the motion of the 4 targets used here is typical of the range of motion a wheat plant experiences. Figure 7.4 shows the coherence estimates from the model corresponding to the input values presented above. The run numbers shown on the graph correspond to the target number of Table 7.4

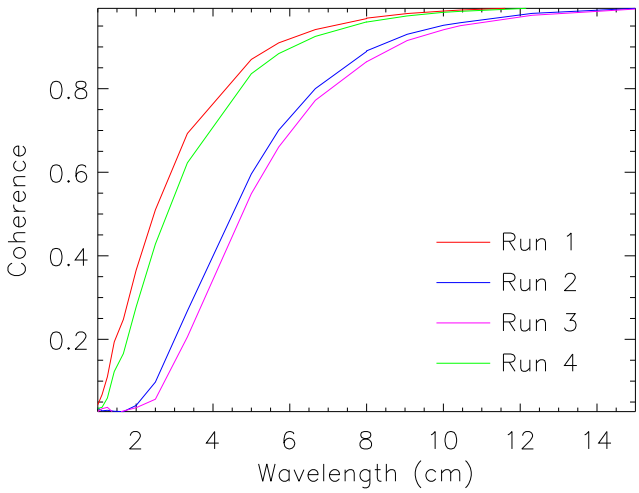

Figure 7.4: Variation of the coherence with wavelength, for 4 different instances of wheat motion derived from measurement data collected on June 6^{th}

The coherence increases with increasing wavelength, due a higher contribution of surface scattering mechanisms at long wavelengths, as shown in Figure 7.3. Adding to this effect is the fact that a fixed crop motion translates into a higher phase standard deviation at shorter wavelengths. The decrease of coherence with increasing phase standard deviation was shown in section 3.5.1 and in the previous section. It combines with the variation of the scattering contributions with λ to explain the coherence variation shown in Figure 7.4.

At long wavelengths, the coherence is nearly equal to 1 in all 4 runs, because the radar sees very little of the vegetation and of its motion. At the shortest wavelengths, the radar wave is backscattered by the upper part of the canopy, and a small vegetation motion is sufficient to infer total decorrelation. Up to $\lambda \approx$ 5-6 cm, the slope of the coherence curves is steep. This relates to the rapid increase of the surface scattering contribution observed in Figure 7.3 for λ <6 cm. Runs 1 and 4 on the one hand, 2 and 3 on the other hand, show similar variations because of the similarity of the displacement distributions in these two pairs of cases. In the case of large motion (runs 2 and 3) the coherence is lower than for small motion (runs 1 and 4). The coherence difference is particularly significant at $\lambda \approx$2-3 cm, where it is about 0.5.

There are several implications deriving directly from the features shown in Figure 7.4. First, the choice of the radar wavelength has a significant impact on the

coherence level from a wheat field, and this is likely to be the case for most agricultural crops. Even within the C-band itself, the coherence expected from a crop field will vary significantly at different wavelengths and consequently change the interpretation and use that can be made of it. There is not a single optimal wavelength at which the use of coherence is maximised, since different applications can have different requirements. At λ =5.6 cm (ERS value), the coherence obtained from a wheat field experiencing high wind conditions (high motion variations) is inferior by about 0.2 to the value which would be obtained from the same field in low wind conditions. This variability can be considered as a negative effect when the coherence is to be used to study the relations with crop parameters like height or biomass because it translates into higher uncertainty margins on the empirical relationships. For that reason, longer wavelength SARs would be more adapted to crop monitoring. However, this conclusion should be mitigated by the fact that long wavelength SARs are sensitive to the surface rather than the vegetation, and therefore not sensitive to the part of the scattering medium of prime interest. The variability of coherence with crop motion conditions can also be seen as a positive effect because it is a potential sensitivity to different vegetation types: short, medium and tall vegetation have distinct amplitudes and coherence thresholds could be adjusted to make a broad classification.

In summary, and drawing conclusions only from the viewpoint of the use of coherence, short wavelength SARs are suitable to differentiate vegetation types with very distinct motion characteristics in given wind conditions. Long wavelength SARs are insensitive to the vegetation, and more adapted to obtain good quality interferograms. The wavelength domain between these two extremes roughly corresponds to the C-Band region. It yields intermediate coherence levels which are both sensitive to the motion characteristics of vegetation and sufficiently high to be used for interferometry applications. In that sense, a C-band SAR can be viewed as a good compromise for several applications.

The variability of the C-Band SAR coherence with the motion characteristics will be the subject of section 7.6, but it can be seen already that it is a major limitation to the operational use of coherence for crop monitoring, as it infers high uncertainties on any potential empirical relationship. It is certainly one of the reasons why most of the studies based on the use of coherence for vegetation applications have failed to obtain consistently good results (see section 2.3).

7.4 Influence of the radar look direction on the coherence

The scattering processes responsible for the backscatter intensity from a vegetation layer are dependent on the radar incidence angle, and the motion of the vegetation in the direction parallel to the travelling direction of the radar wave affects the phase of the radar backscatter. Therefore the backscatter intensity and coherence obtained from a given vegetation medium are expected to vary with the radar look direction.

The radar look direction is defined by the incidence angle θ and the azimuth

angle α. θ is the angle between the travel direction of the incoming radar wave and the local vertical defined at the surface. For a surface with no slopes due to local topography, it is also equal to the angle between the local vertical at the radar antenna and the radar beam direction. However, slopes on the surface change the angle at which the incident radar waves reach the vegetation layer. α is the angle between a fixed direction in the horizontal plane and the projection of the radar beam on this plane. The choice of the reference direction is arbitrary. Here, it is taken as the x direction of the wheat motion measurements, which is also the approximate direction of the mean wind during the measurements. With this definition, it is possible to study whether the coherence shows a systematic variation, depending on the alignment of the look direction with the mean wind at the time of the radar pass.

7.4.1 Coherence and incidence angle

In Chapter 3, the influence of the radar incidence angle on the backscatter intensity (section 3.3) and on the coherence (section 3.5.2) was presented to illustrate the respective capabilities of RT2 and the coherence model. The analysis here is based on the same input parameters, but now includes the knowledge of the wheat displacements.

The wheat is modelled as in the previous section, using the parameters presented in Appendix A.4. The radar wavelength is fixed to the ERS value (λ=5.66 cm), and the incidence angle is varied from 10° to 70°. The phase distributions of the dynamic components present in the coherence model are based on the displacement of the scatterers in the slant range direction. This direction varies with the incidence angle and consequently the phase distributions are calculated for each instance of θ. As in the previous section, the motion measurements used here are those collected on June 6^{th}. The phase distributions based on motion measurements of targets 1 and 2 are used here to show the variability of the coherence in low (target 1) and high (target 2) motion conditions. The radar resolution cell is set to 25x5 m, and the azimuth angle is fixed to $\alpha = 0°$ for the moment.

The variation with θ of the several scattering contributions was plotted in Figure 3.4. The analysis is not repeated here, but briefly summarised. The surface scattering contribution dominates the total backscatter for $\theta < 25°$. At VV polarisation, for $30° < \theta < 55°$, the dominant scattering mechanism is the double-bounce between the wheat stalks and the ground, and the direct scattering from the vegetation layer is the most significant contribution for $\theta > 60°$. The peak contribution of the double scattering between 30° and 55° is a specific feature of the VV polarisation. The two scattering processes (direct and double scattering) are equally significant at HH polarisation. The stronger coupling between the vertically polarised radar wave and the vertically oriented wheat stalks is at the origin of this difference between the VV and HH variations.

Figure 7.5 shows the variation of the coherence with the incidence angle computed with the coherence model based on the inputs above.

The decrease of the coherence with increasing θ is due to the combination of two independent effects. First, the surface scattering contribution is stronger at low

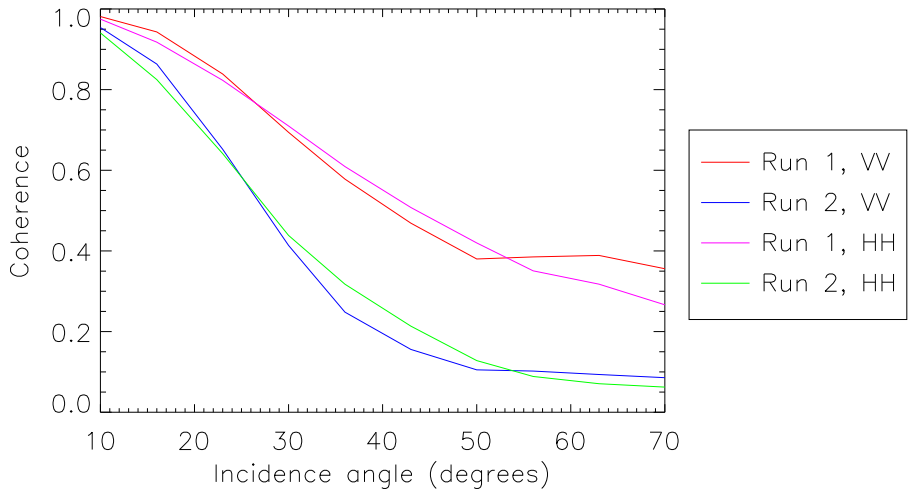

Figure 7.5: Variation of the coherence with the incidence angle for VV and HH polarisations

incidence angles and results in high coherence values. The increasing significance of the vegetation scattering processes as θ increases is at the origin of the coherence decrease. Adding to this effect, a given data set of wheat positions translates into larger slant range displacements at high incidence angle because the motion of wheat occurs mainly in a horizontal plane. Consequently, the phase distribution of the dynamic components in the coherence model widens as θ increases. The amplitude and phase of the total electric field are more variable at high incidence angles and the coherence associated with this variable electric field is therefore lower. The origin of the coherence decrease here presents some similarity with the decrease with wavelength analysed in the previous section, in that it is linked to the combined effect of a variation of the dominant scattering processes and an increase of the phase standard deviations of the dynamic components of the electric field.

As in section 7.3, the coherence obtained from the lower motion amplitude (target 1) is higher than when the wheat motion has a larger amplitude (target 2). For both polarisations, the coherence from run 1 is still about 0.3 at $\theta = 70°$, whereas in run 2 the decorrelation is almost total ($\gamma = 0.1$) for $\theta > 55°$. The coherence difference between the two runs is low for small incidence angels because the radar backscatter is dominated by surface scattering, and increases to reach about 0.3 at $\theta = 35°$. For $\theta > 35°$, the difference between run 1 and 2 is stable and even diminishes slightly to 0.25. The variability of the coherence with the motion characteristics of the wheat is once more highlighted here. The coherence difference of about 0.2 between runs 1 and 2 for $\theta = 23°$ is visible in Figure 7.5 and, incidentally, also in Figure 7.4 at $\lambda = 5.6cm$.

The difference between the VV and HH polarisations is inferior to 0.1 for all incidence angles. The coherence obtained from the scattering contributions at VV and HH polarisations are called here the VV and HH coherence respectively. In both runs, the HH coherence is superior for $\theta < 25°$ and $\theta > 55°$. Between these two values, the VV coherence is higher, due to the extra scattering linked to the double bounce between the stalks and the surface. The difference in the coherence estimates

from the two polarisations was already highlighted in Figure 3.8(c). It was then said that this difference could be used to differentiate crop types with a clear vertical structure such as wheat. Although this is true in principle, the difference between the VV and HH polarisations is only 0.1 at most, and likely to be overshadowed by the coherence variability linked to the wind conditions, and is difficult to quantify accurately due to the uncertainties in the estimates from the coherence model and from RT2.

The slope of the coherence decrease is maximum for $15° < \theta < 35°$. Focusing on run 2 and VV polarisation, which represents the most extreme case, an incidence angle variation of $\pm 5°$ centred on θ=23° corresponds to a coherence variation of about 0.3. The coherence obtained with SAR data from vegetation on sloping terrain will therefore be subject to such variability. It is a significant amount that can change the interpretation of surface features based on the coherence, either through classification thresholds or empirical relationships with biophysical parameters. If the surface contains significant topographic features, then the coherence user should take additional care in the interpretation of the coherence levels, since they are likely to be strongly affected by the local slopes. For the slope effect on coherence to be ignored, radar incidence angles superior to $\theta = 50°$ should be used, but they yield low coherence levels incompatible with other SAR interferometry applications.

As for the study of the influence of the wavelength, the ERS value chosen for the incidence angle (θ=23°) translates into the highest sensitivity, this time to the surface slopes. But it is nevertheless the most adapted to vegetation monitoring. Radar backscatter from low incidence angles is not sensitive to the motion of the crop elements and therefore does not have the potential to give useful information about them and, at high incidence angles, the sensitivity to the motion of scatterers is too important and gives consistently low coherence. The range if incidence angles from which the coherence is potentially useful is approximately $[20°, 40°]$.

7.4.2 Coherence and azimuth angle

The azimuth angle α defines the radar look direction in a horizontal plane, relative to a fixed direction in this plane. The coherence can in principle show a dependence to α if the scatterers in the vegetation medium move in a dominant direction in the horizontal plane. For example, it is possible that the wind moves the vegetation elements in a dominant direction (the wind direction). If the azimuth angle is such that the incoming radar wave travels in a direction parallel to that dominant direction of motion, then the resulting coherence is expected to be lower than in the perpendicular direction because the complex backscatter signal is subject to larger phase changes.

The variability of the coherence with the azimuth angle is therefore linked to the condition that the vegetation is moving in a dominant direction in the horizontal plane. The wheat motion measurements presented in the previous chapter have shown that there is not a clear preferred direction of motion (section 6.5.1), so the coherence estimates made here and based on these measurements are not expected to show a consistent variation with α. However, the motion of wheat heads was occasionally measured to follow a dominant direction, and this section will present

the resulting effects on coherence if all scatterers in the ground resolution cell have this dominant direction. For that purpose, the targets 1 and 2 used above for the study of the incidence angle are useful here again because target 1 does not show a strong motion orientation in the horizontal plane, but target 2 does. The comparison of the two provides a good estimate of the effect of the relative orientations of the wheat motion and the radar azimuth on the coherence.

The radar wavelength is still $\lambda = 5.66cm$, the resolution 25x5 m, and the incidence angle fixed to $\theta = 23°$. The scattering contributions at this angle are taken from the same estimates as those presented above for the study of the incidence angle effects. The scattering contributions are assumed to not be significantly dependent on the azimuth angle. α is not a parameter which can be accounted for in RT2 anyway, because the orientation of the vegetation scatterers is assumed to be uniformly distributed in azimuth in the backscatter model. However, RT2 does include the possibility to define a corrugated surface by its amplitude, wavelength, and orientation with respect to the radar look direction. A surface showing regular patterns is likely to influence the radar backscatter and therefore the dependence of σ^0 and the coherence to the azimuth angle. This effect is not studied here because a wheat field does not show surface corrugations, but it is acknowledged as a potential area of further study for crops growing on such surfaces.

The azimuth angle is varied from $-90°$ to $90°$. For each value of α, the distribution of the slant range displacements based on the motion measurements of targets 1 and 2 on June 6^{th} is calculated. The associated Gaussian distributions in each case are used to define the phase of the dynamic component in the coherence model. Figure 7.6 shows the variation of coherence with α, together with the locus of targets 1 and 2 in the horizontal plane. The angle α simulates the angle between the radar look direction in this horizontal plane and the x axis. The correlation coefficient of the (x,y) coordinates shown in Figures 7.6(b) and 7.6(c) are 0.25 and 0.86 respectively, and confirm numerically the stronger motion direction dependence measured with target 2.

The coherence from run 1 does not vary significantly with α and approximately remains in the range [0.85;0.9]. This relates well to the locus of target 1 (Figure 7.6(b)), which does not show a dominant direction of motion. Figure 7.6(c) shows that the motion of target 2 is oriented at an angle of about $45°$ with respect to the x axis. The variation of the coherence is sensitive to this direction. For $\alpha \approx -50°$, the coherence is maximum because the motion of wheat is oriented perpendicularly to the radar look direction and infers little phase variations of the complex backscatter. The coherence decreases as the radar look direction becomes aligned with the main motion direction ($0° < \alpha < 50°$). It should be noted however that the minimum coherence is reached for a wide range of azimuth angles and not particularly marked at $\alpha = 45°$.

The amplitude of the coherence variation is about 0.3. The coherence from crops moving in a dominant direction is therefore significantly affected by the azimuth angle of the radar antenna. In the case of wheat, the measurements of Chapter 6 showed that there is not a systematic dependence of the motion to a particular direction, except in some isolated cases such as target 2 on June 6^{th}. For that reason, the coherence obtained from a wheat field should not show a significant variability

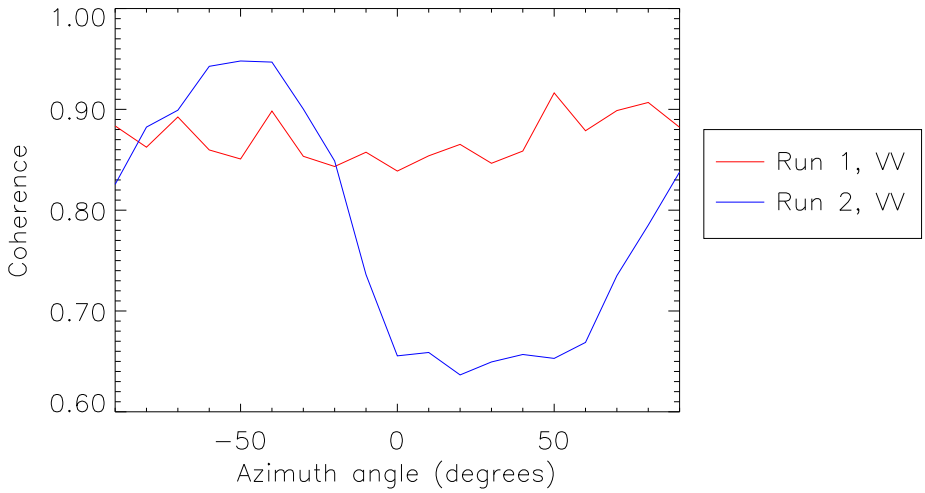

(a) Coherence vs. azimuth angle

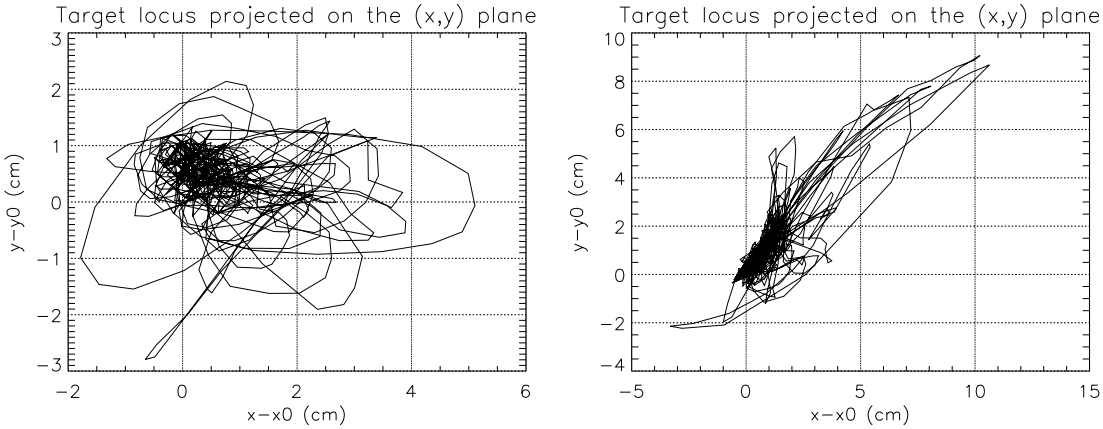

(b) Target 1 locus

(c) Target 2 locus

Figure 7.6: Variation of the coherence with azimuth angle and locus of the targets used to generate the phase distributions

with the radar azimuth angle, which means that several wheat fields at different locations will not yield variable coherence values. This conclusion only concerns the effect of the azimuth angle, and not other independent effects such as the variability of the wind conditions at different locations or the slope differences. The results presented here also showed that a large coherence variation can be expected from a crop which would have a dominant motion direction. Measurements such as those presented in Chapter 6 should be made on other crops in order to determine if such vegetation types exist.

7.5 Influence of the repeat time on the coherence

So far the coherence estimates have been based on the assumption that the scattering contributions remain constant for the two sets of pixels which simulate the two passes of the radar antenna over the same area. Such an assumption is correct if the repeat time between the passes is short, so there is no significant change to the surface and the vegetation. If the scattering volume is a field covered by a crop such as wheat, the scattering contributions are likely to change after a certain time difference between the radar passes, due to changes in the wheat phenotype throughout its growth period. For that reason, the coherence obtained from SAR data over a wheat field or any other crop is expected to vary with the time difference between the two radar passes. This section aims to quantify how the repeat time of the radar passes influences the coherence from a wheat field.

The time variation of the scattering contributions from a wheat field presented in Table 7.3 and published in [51] will be used here. The two sets of pixels in the coherence model are computed with different amplitudes for the different components of the total electric field, each set being generated with the contributions from one of the 13 dates available in Table 7.3. The scattering contributions being available for a time span of 4 months (from April 10^{th} to August 10^{th}), the maximum repeat time which can be simulated here is 120 days. It is not possible to make coherence estimates with longer time difference between the radar passes because the variability of the scattering contributions in the same field from one year to the other is unknown.

For the coherence estimates presented here, the radar wavelength is set to $\lambda = 5.66cm$, the incidence angle is $\theta = 23°$, the azimuth angle is $\alpha = 0°$, the resolution is 25x5 m. In order to assess the variability of the coherence only with the change of the scattering contributions, the wheat motion conditions are fixed. They are based on the motion measurements of target 6 on July 19^{th}. This choice is justified by the fact that the mean wind speed on July 19^{th} is close to the average of all the mean wind speeds at the different recording dates ($\bar{w} = 2.2m.s^{-1}$, see Table 6.12). The motion conditions on July 19^{th} are therefore representative of average conditions. The distribution of the slant range displacement of target 6 on July 19^{th} is used to generate a Gaussian phase distribution, in a similar manner as in the previous sections and following the methodology presented in section 7.1.2.

The first set of pixels is computed with each date available in Table 7.3. For a simulation of the first pixel set made with scattering contributions from a given date D_1, the second set of pixels is simulated with each date available in Table 7.3 and subsequent to D_1 . Therefore the coherence is estimated by the model for repeat times ranging from 10 to 120 days. With N$\epsilon\{1, 12\}$, the 10xN day repeat time coherence is achievable 13-N times with the values of Table 7.3. The parameter of interest being here the influence of the repeat time on the coherence, the estimates obtained with the several time intervals are compared to the case where the two sets of pixels are computed with scattering contributions from the same date. In other words, the reference case is that of short repeat time, as in the ERS-1/2 Tandem mission, and the coherence in all other cases are compared to this reference.

First, the simulated Tandem coherence obtained from the 13 dates is averaged,

giving the reference value $\overline{\gamma}_R = 0.52$. All coherence estimates based on the same repeat time ΔT are also averaged, leading to 12 values of $\overline{\gamma}_{\Delta T}$. Figure 7.7 shows the variation of the difference $\Delta\gamma = \overline{\gamma}_R - \overline{\gamma}_{\Delta T}$ with repeat time ΔT.

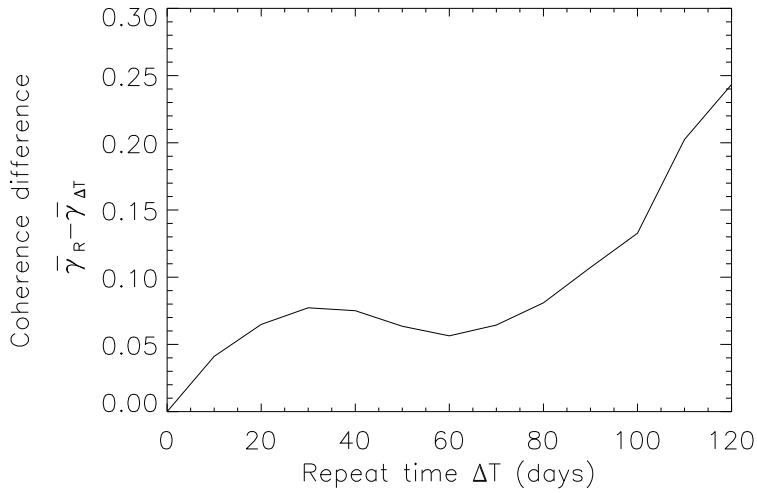

Figure 7.7: Variation of the coherence difference $\overline{\gamma_R} - \overline{\gamma_{\Delta T}}$ with the repeat time between the two radar passes

The first feature to note on the graph is that $\Delta\gamma$ is positive for all values of the repeat time. This means that the coherence calculated with the same scattering contributions for the two sets of pixels (short repeat time coherence) is higher than when different contributions are used (long repeat time coherence). There is a general increase of $\Delta\gamma$ with increasing ΔT, representing a decrease of the coherence with increasing time difference between the two radar passes. Figure 7.7 shows that the coherence difference remains inferior to 0.1 for up to 90 days, and reaches its maximum of about 0.25 for the maximum time difference (120 days). A difference inferior to 0.1 for $\Delta T < 90$ days is not significant because of the other sources of variability affecting the coherence and discussed in the previous sections. However, it is important to remember here that the coherence estimates have assumed constant wind conditions at all dates. The variation displayed in Figure 7.7 is interesting because it shows the minimum intrinsic coherence decrease to expect due to phenotypic changes in the wheat field, but the different wind conditions at the two radar passes will add to this minimum variation. Bearing this aspect in mind, Figure 7.7 shows that changes of the wheat phenotype alone do not affect the coherence significantly if the repeat time between the two radar passes is shorter than 90 days (3 months). This result is *a priori* surprising because a wheat field undergoes significant changes throughout the growth season, from the state of bare soil to that of a mature crop. The repeat time should therefore affect the coherence more significantly.

Figure 7.8 helps to clarify this difficulty in the interpretation. The coherence plotted in Figure 7.7 is based on average values over the total number of coherence estimates available for a given repeat time and therefore does not allow to identify the time variation of the coherence difference. Figure 7.8 shows the variation with the day of year of $\Delta\gamma(t) = \gamma_R(t) - \gamma_{\Delta T}(t)$. $\gamma_R(t)$ is the short repeat time coherence

(same scattering contributions for the two sets of pixels) and $\gamma_{\Delta T}(t)$ is the coherence based on scattering contributions at two different dates separated by the time ΔT. The day of year displayed on the x axis of the graph is the date used for the simulation of the first set of pixels. The time variation is displayed for ΔT ranging from 10 to 60 days, in increments of 10 days.

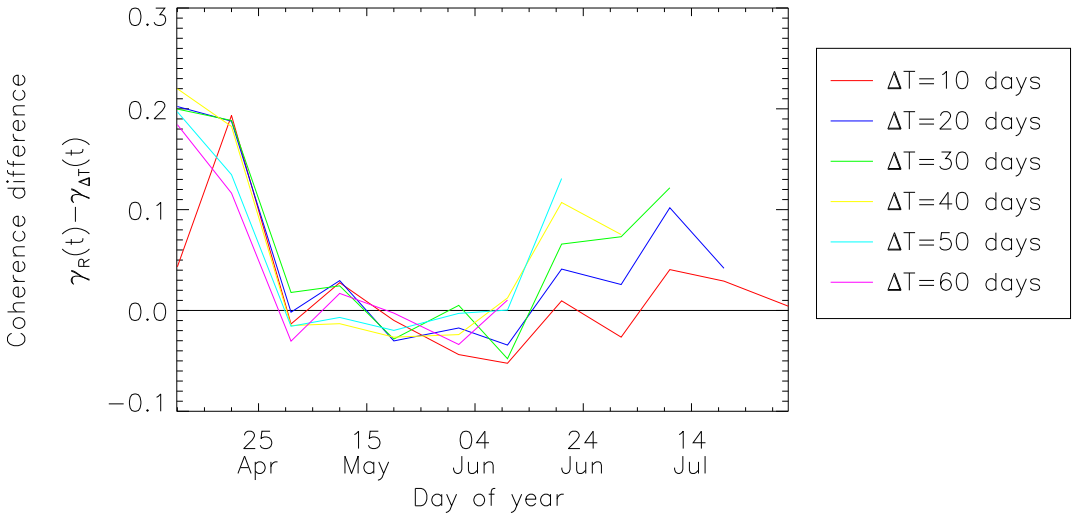

Figure 7.8: Variation of the coherence difference $\gamma_R(t) - \gamma_{\Delta T}(t)$ with the day of year for 6 instances of the repeat time ΔT

The variation obtained for each value of the repeat time covers a shorter time period on the x axis of the graph as ΔT increases because no scattering contributions are available after August 10^{th}. Therefore the latest date when it is possible to estimate the coherence $\gamma_{\Delta T}$ is (August 10^{th} - ΔT). The coherence difference is maximum if the first radar pass occurs at the beginning of the season. On April 10^{th}, $\gamma_{\Delta T}$ is lower than γ_R by about 0.2 for $\Delta T \geq 20$ days. The difference is due to the rapid change of the wheat field at the beginning of the season, from the state of bare soil to that of a growing crop. Table 7.3 shows that the scattering contributions do change significantly between April 10^{th} and the rest of the season, and this translates in the coherence drop of 0.2 between short and long repeat time coherence. Note that the coherence difference between γ_R and γ_{10} on April 10^{th} is low, because the wheat field remains close to bare soil between April 10^{th} and April 20^{th}. From May onwards, the difference $\Delta\gamma$ is inferior to 0.1. The wheat does undergo changes of its phenotype after May, but they do not affect the coherence significantly, in terms of the time difference between the two radar passes. However, comparison of the curves in June shows a slight increase of the coherence difference with increasing repeat time. The wheat in June is at its full growth and in its maximum green state, whereas it is drying rapidly in July and August. The coherence obtained with one radar pass in June and the other in July or August is therefore significantly different than the short repeat time coherence, where the radar collects data from wheat in an identical state of moisture content.

The first conclusion from the variations above is that there will be a significant drop of coherence if one of the radar pass occurs while the wheat field is close to its bare soil state, and the other pass is during the main growth season. This result

could have been expected since the appearance of a wheat field is most different in the two cases. The analysis quantifies to 0.2 the difference to expect compared to short repeat time coherence, assuming the average wind conditions represented by the wheat motion measurements made on July 19^{th}.

The other conclusion from the analysis is that, if the two radar passes occur between May and August, then the coherence obtained with a long repeat time should not be significantly different from the short repeat time coherence. This has important implications on the operational use of SAR interferometry. The design of a spaceborne radar with a short repeat time imposes stringent constraints on the satellite orbit. In particular, reducing the repeat time of the orbit over a certain area results in a longer time required for global coverage of the Earth. This is not always compatible with other applications based on SAR data from the same satellite and, more importantly, it starts to defeat the object of using satellites for Earth observation. Since the coherence obtained from wheat is not strongly changed if the orbit repeat time is 10 or 90 days, then the orbit specifications can be more flexible, and consequently satisfy a larger number of users. The analysis above tends to show that the coherence from a wheat field, collected at two dates between May and August, is not very sensitive to the repeat time between the two satellite passes. From this point of view, there is not a strong requirement for interferometric data based on a short repeat time, similar to that of the ERS-1/2 Tandem mission. However, this conclusion needs to be mitigated by several considerations. First, reducing the repeat time allows to collect more data from the same field in the growth season and therefore increases the potential use of coherence for analysis of biophysical parameters. The second aspect to consider is that the coherence is significantly affected if one of the radar passes occurs when the crop field is in a bare soil state, before growth or after harvest. For that reason, in InSAR applications where low coherence is not desirable, a short repeat time is more adapted. Finally, the study concentrated on wheat and, for crops changing more significantly during their growth, the repeat time will impact more strongly the coherence. This is likely to be the case for example for corn, which is a higher crop.

The coherence simulations were based here on the assumption that the same wheat motion characteristics could be used at all dates during the growth season. This assumption was useful to see the influence of the repeat time on the coherence, based only on the change of the scattering contributions in the season. However, the variability of the wind conditions adds extra decorrelation. The amount of this decorrelation is assessed in the next section.

7.6 Variability of the coherence due to wind conditions

The estimates of the preceding sections indicated that the coherence can vary significantly with the wind conditions. This section aims to quantify this variability throughout the growth season. The use of coherence in forestry or agricultural applications is based on the assumption that its value is representative of some of the biophysical properties of the forest or crop of interest. Knowing the variability of

the coherence expected from a crop subject to variable wind conditions is therefore essential to assess the validity of this assumption. Most of the past studies presented in section 2.3 have used empirical relationships or have defined thresholds for classification purposes without assessing the variability of the coherence with the wind conditions at the date the SAR data were collected. The coherence model is used here to make this assessment, in the case of wheat.

The methodology below is applied and discussed in detail in the remainder of this section. It is outlined here in order to present its objectives and expected outputs, and justify the description of intermediate steps. Since the wind conditions at the day and time of the radar passes are unknown in general, the only way to assess the coherence variability is to use a statistical approach. Section 6.4.4 presented some wind statistics based on data collected by a local weather station at Cranfield University in 1996 and 1997. The wind speed statistics were translated to statistics of wheat motion amplitude in section 6.6.3, via the use of an empirical relationship relating the wind speed and the wheat amplitude. In this section, the same method is applied to relate the wind speed and the standard deviation σ_s of the Gaussian distribution describing the slant range displacement of the wheat heads. Then, using the weather station wind statistics of section 6.4.4, the probability density function of σ_s can be estimated. It is noted here $p(\sigma_s)$. σ_s is used to define the phase distribution of the dynamic components of the coherence model. It is therefore possible, from the knowledge of $p(\sigma_s)$, to calculate the average coherence to expect at a given date in the season, as well as the standard deviation on this average coherence. The method is entirely numerical and therefore involves estimates by the Monte-Carlo method. The resulting standard deviation of the coherence is an indicator of its variability.

Section 7.6.1 shows how σ_s is related to wind speed and shows its statistical properties. The probability density function $p(\sigma_s)$ is then used in section 7.6.2 to estimate the mean coherence and its standard deviation at a given date in the growth season.

7.6.1 Statistics of the slant range standard deviation σ_s

In the remainder of this section, the radar incidence angle is fixed to the ERS value of 23°, and the azimuth angle is fixed to $\alpha = 0°$. In section 6.6.3, it was shown how probability density functions of the wheat head amplitude could be derived from the annual wind statistics provided by the Cranfield weather station. Here, the same method is applied to calculate the probability density function of σ_s, based on the same wind statistics.

For this purpose, Gaussian distributions are fitted to the true distributions of slant range displacement, for each wheat head tracked during the measurements, and for all recording dates. For each date when measurements were taken, the average standard deviation obtained from all targets is calculated. Then it is possible to relate these average values of σ_s to the corresponding wind speed at canopy level measured at each date. Figure 7.9 shows the average value of σ_s plotted against the average wind speed. In the remainder of this section, the average value of σ_s is simply noted σ_s.

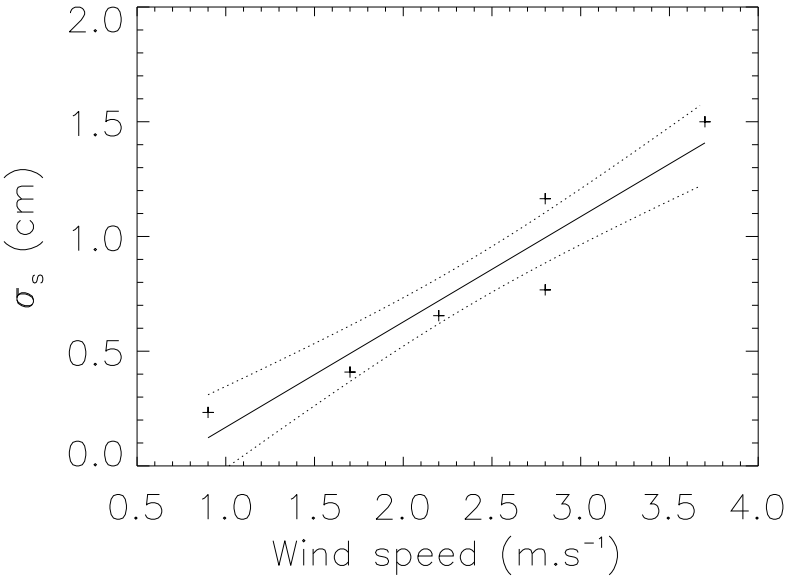

Figure 7.9: Average standard deviation of the wheat head slant range displacements vs. mean wind speed with regression line (solid line) and 80% confidence interval (dotted lines)

Figure 7.9 is similar to Figure 6.26, where the value plotted on the y axis is the wheat amplitude, instead of σ_s. The linear fit obtained shows that the wheat head motion spread about its mean value increases as the wind speed increases. The equation of the linear fit is:

$$\sigma_s[cm] = 0.459 * w[m.s^{-1}] - 0.290 \tag{7.10}$$

In section 6.6.3, the probability density function of the wheat amplitude was derived from the linear relationship of Equation (6.11). The same methodology can be applied here to derive statistics of σ_s, based on the wind statistics collected by the weather station, and on Equation (7.10). Since the main wheat growth season ranges from May to August, only the wind speeds from these months are used here to calculate the statistics of σ_s, in order to give a more accurate representation. In addition to this, the wind statistics are different at different times of the day, so the probability functions of σ_s are given for the four categories introduced in section 6.4.4 (night, morning, afternoon, evening).

First, the weather station wind speeds for each category are translated into speeds at wheat height with Equation (6.8). Then the values of σ_s associated to these canopy height wind speeds are calculated from Equation (7.10). The probability density function of σ_s can then be computed. Figure 7.10 shows the probability density functions of σ_s for the four daily categories, as well as the cumulative probability functions. Statistics based on the 1996 and 1997 data are presented.

As for the statistics of the wheat amplitude, there is a non-zero probability that $\sigma_s = 0$. Physically, it corresponds to the fact that there is a minimum wind speed required to actuate the wheat plant. It also corresponds to the minimum motion detectable by the measurement system. The probability density function of Figure 7.10(b) and 7.10(d) will be used in the numerical simulations of the next section.

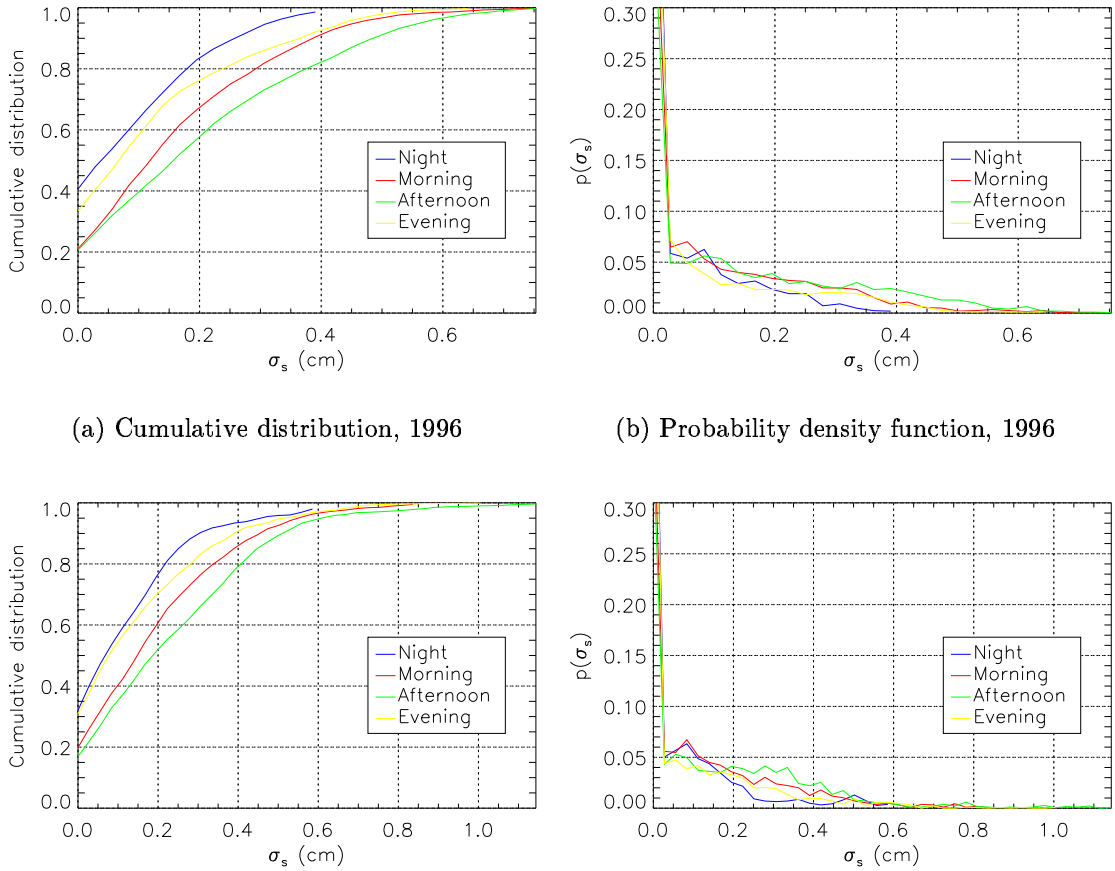

(a) Cumulative distribution, 1996

(b) Probability density function, 1996

(c) Cumulative distribution, 1997

(d) Probability density function, 1997

Figure 7.10: Probability density functions of σ_s for the 4 daily categories, based on the wind data collected in 1996 and 1997

The cumulative probability functions of Figure 7.10(a) and 7.10(c) show that the wheat motion at night is lower than during the day because a given probability is reached for a lower value of σ_s at night. This feature was already observed in section 6.6.3 for the wheat amplitudes. The slant range standard deviation is expected to be higher in the afternoon, so the coherence obtained from data collected between 12am and 6 pm should yield lower coherence than with SAR data collected at night. The next section will quantify this expected effect.

The approach presented here is subject to several sources of uncertainty:

- The average values of σ_s calculated from the measurements are based on the total number of targets tracked at each recording date. This number is at most 8, but it is an implicit assumption in the method above that the average value of σ_s is representative of the motion of all wheat plants at a given date. A better accuracy on the mean σ_s would be obtained with a higher number of targets tracked by the video system. However, this infers an increased processing time.

- The relation between the wind speed at wheat height and at the height of the

weather station is based on the wind measurements presented in section 6.4.1. Again, more wind measurements would strengthen the relation.

- The linear relation presented above between the mean value of σ_s and the mean wind speed at wheat canopy height is based on 6 points, corresponding to the 6 measurement dates. The estimates provided by the regression line fitted to these points have an uncertainty associated to them, which can be evaluated by the 80% confidence intervals displayed in Figure 7.9. For a wind speed at canopy height of 2.4 $m.s^{-1}$ (average wind speed represented on the graph), the value of σ_s obtained from the linear fit is about 0.8, and the width of the 80% confidence interval at this point is about 0.2. This is a significant amount of the nominal value (25%), showing that the linear fit between the wind speed and the standard deviation of the slant range displacements has a limited accuracy. It can be improved by increasing the number of measurement points in Figure 7.9, meaning that a more intensive measurement campaign is required.

The issues raised above show the direct relation between the necessity to have as many measurement data points as possible and the accuracy of the method presented in this section. They show clearly how the design of the measurement system and the planning of its use throughout the growth season affects the results of the modelling presented here. The modelling approach and analysis to follow in this section and the next would benefit significantly from additional measurements. However, it is interesting to carry on the analysis to provide an estimate of the sensitivity of the coherence to the wind conditions. This estimate is subject to further modifications if more measurement data sets become available, but the methodology applied to provide them will already be demonstrated in this report. It integrates the wind and wheat motion measurements, the weather station wind data, and the coherence model.

7.6.2 Simulation of the coherence in the growth season

The coherence model is run here with the scattering contributions given in Table 7.3. The wavelength is set to $\lambda = 5.66cm$, the radar azimuth and incidence angles are $\alpha = 0°$ and $\theta = 23°$ respectively, and the resolution is 25x5 m. The parameters aim to simulate the case of the ERS SAR because the coherence estimates will be compared in the next section to ERS coherence obtained from data collected in 1996 over the agricultural area surrounding Cranfield University.

Monte-Carlo simulation of the coherence from a wheat field

A series of N values of σ_s are randomly generated, and made to follow the probability density function shown in Figures 7.10(b) and 7.10(d). The generation of the N values of σ_s is performed with an algorithm applying the rejection method given in [56]. Each value of σ_s represents a slant range displacement standard deviation used to define the Gaussian distribution of the dynamic components of the coherence model. So, for each set of scattering contributions of Table 7.3 (i.e. each growth

stage), the coherence model is run N times. The outputs represent the coherence expected in the different wind conditions characteristic of the local area. Therefore the N outputs express the coherence values which are likely to be obtained from SAR data collected in the area. A good representation of the coherence by this method depends on the number of simulations N. A high number is required to increase the significance of the coherence average and standard deviation derived from them. The drawback of increasing the number of simulations is that it increases the processing time. The results presented below are based on a number of simulations N=50, as preliminary tests showed it combines a workable processing time with stable output coherence averages and standard deviations.

The average coherence γ obtained from the 50 simulations is plotted in Figure 7.11 against the time of year. A standard deviation σ_γ is also calculated from the 50 estimates at each date and represented as an error bar. Since the probability density function of σ_s is defined for 4 categories related to the time of day, the coherence estimates are also made separately for these four categories, and plotted in Figure 7.11(b). The results were obtained from the 1996 weather station data.

The variation of the coherence with time will be discussed in more detail in section 7.7. Of interest here is the variability of the coherence due to the wind conditions. Figure 7.11(a) shows that the $\pm\sigma_\gamma$ error bars represent a significant amount of the average coherence values. Table 7.5 gives the average coherence and the average standard deviation obtained for all dates throughout the growth season (noted $\overline{\gamma}$ and $\overline{\sigma_\gamma}$ respectively).

	$\overline{\gamma}$	$\overline{\sigma_\gamma}$
Overall	0.58	0.23
Night	0.67	0.20
Morning	0.61	0.23
Afternoon	0.51	0.24
Evening	0.62	0.22

Table 7.5: Average coherence and standard deviation obtained for all dates throughout the growth season

Analysis of the variability of the coherence

The overall standard deviation on the coherence estimates is about 0.2 and the average coherence is 0.6. A variation of 1 standard deviation from the mean therefore represents a change of 33% of the mean value. This is a significant amount which quantifies the variability of the coherence in the summer wind conditions. The average standard deviation of 0.2 remains approximately constant for all 4 categories related to the time of day. Figure 7.11(b) shows the different coherence variations depending on the time of the day from which the SAR data originate. The two extremes cases correspond to the coherence estimated from the night and afternoon categories. The wind conditions at night being more quiet than during the afternoon, the resulting coherence estimates at night are higher. The average coherence

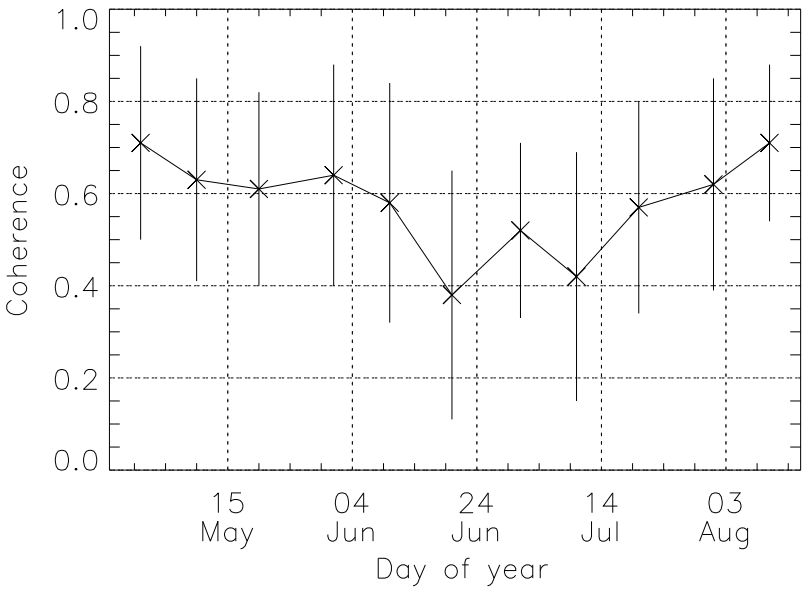

(a) Overall variation with error bars corresponding to ± 1 standard deviation

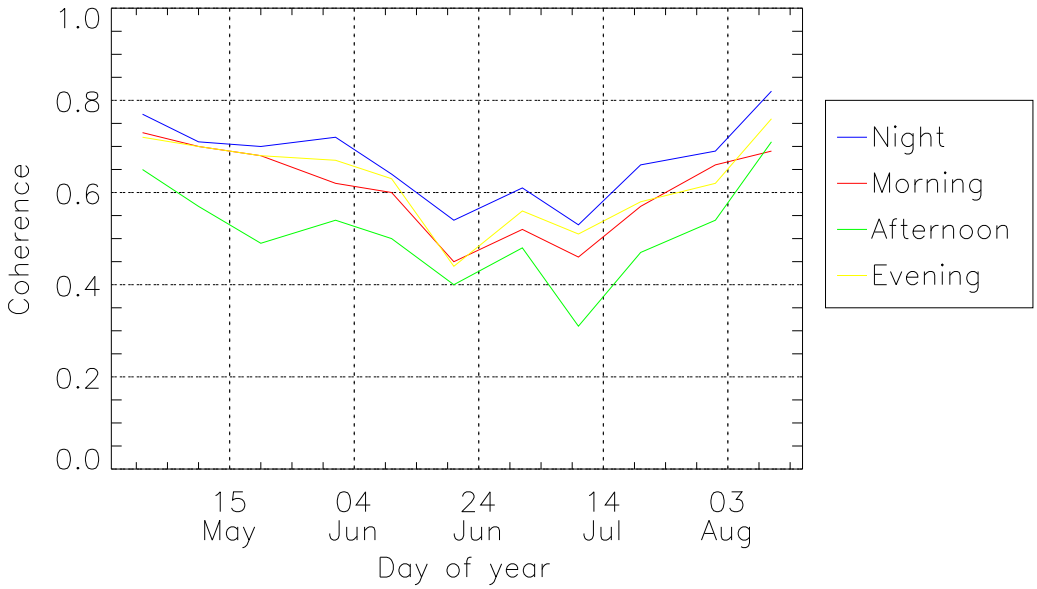

(b) Variation for the 4 daily categories

Figure 7.11: Variation of the average coherence with day of year, obtained from 50 simulations

difference between the two cases is 0.16, with a maximum difference of 0.22 obtained on July 10^{th} and a minimum of 0.11 on August 10^{th}.

The average coherence obtained for a given date is based on 50 estimates and for that reason it can be considered as a reliable representation of the biophysical properties of the wheat, or more precisely of the relative contributions of the different

scattering mechanisms governing the total backscatter. The coherence obtained from real SAR data is a representation of the added effects of these biophysical properties and of the wind conditions at the time of the radar passes. Only the biophysical parameters of the crop are of interest to the scientist and represent the useful signal. The variability due to the wind conditions can be considered as noise added to the useful signal. With such a representation, the analysis above shows that the signal-to-noise ratio is on average 0.6/0.2=3. However, this value is not in itself an indicator for the quality of the retrieval of the coherence "signal". It is dependent on the application for which the coherence is to be used.

Another way to have a concrete understanding about the amount of variability of the coherence is to use the concept of confidence intervals. Let $\mathcal{P}$ be a population of random variables generated in the same way as the coherence values estimated above for a fixed date. From Table 7.5, these random variables have a mean γ=0.6 and standard deviation σ_γ=0.2. Let γ_i (i $\in \{1, \ldots, m\}$) be m coherence values obtained with SAR data from a wheat field, assumed to be m samples from the population $\mathcal{P}$. They define a sample mean γ_s, and principals of sampling theory [65] state that the true mean γ lies in the (1-υ)*100% confidence interval defined by:

$$CI_{(1-\upsilon)} = [\gamma_s - z_{\upsilon/2}\frac{\sigma_\gamma}{\sqrt{m}}; \gamma_s + z_{\upsilon/2}\frac{\sigma_\gamma}{\sqrt{m}}] \tag{7.11}$$

where $z_{\upsilon/2}$ is such that the area between $\upsilon/2$ and $+\infty$ under the Gaussian distribution of mean 0 and standard deviation 1 takes the value $\upsilon/2$. The condition for this definition of the confidence interval to hold is that, either the random variables of the population $\mathcal{P}$ have a Gaussian distribution, or the number of samples taken from this population (m) is sufficiently large. The values of $z_{\upsilon/2}$ are given in most statistics textbooks: for an 80% confidence interval, υ=0.1, and $z_{0.1}$=1.28 [68]. Therefore the size $S_{CI_{80\%}}$ of the 80% confidence interval is:

$$S_{CI_{80\%}} = 2z_{\upsilon/2}\frac{\sigma_\gamma}{\sqrt{m}} = 2 * 1.28 * \frac{0.2}{\sqrt{m}} = \frac{0.512}{\sqrt{m}} \tag{7.12}$$

From Equation (7.12), the number of independent coherence estimates required from a given field so that the 80% confidence interval has a size of 0.1 is 27. From a practical point of view, it is very unlikely that such a high number of samples can be obtained because it involves a high number of radar passes over the same area which is incompatible with spaceborne SARs, and would involve high running costs with an airborne SAR. A reasonable value for the number of coherence estimates from the same field is at most 5, and in most cases 1 or 2. With 5 samples, the size of the 80% confidence interval is about 0.2, and it is 0.5 for a single sample. However, these two values do not carry much meaning about the accuracy of the coherence estimates because they do not fall into the validity limits for the definition of the confidence interval given in Equation (7.11). However, the main message conveyed here is that an accurate estimate of the coherence which is not significantly biased by the wind conditions of a particular day requires a high number of individual estimates, not practically compatible with the current SAR interferometry techniques. It is therefore intrinsic to the coherence values that they carry a high level of "noise" related to the variability of the wind conditions, mixed with the coherence "signal", which is a numerical representation of some of the crop biophysical properties.

From the analysis above, it appears that the use of the coherence for wheat monitoring is significantly limited by its variability with the wind conditions. For that reason, the derivation of empirical relationships between coherence and one or more biophysical parameters is subject to the uncertainties inherent to the coherence estimates. The knowledge of the wind conditions at the time of the radar passes appears to be necessary in order to be able to use coherence more reliably. It is likely that local weather stations in the vicinity of the zone of interest could provide the necessary wind data, or simply standard weather forecasts.

Another interesting feature of the analysis concerns the variation of the coherence with the time of day at which the SAR data are collected. Coherence from crop field obtained from night data is consistently higher than from afternoon data. This has no direct implication on the conclusions above concerning the retrieval of biophysical parameters, but it means that applications of SAR interferometry where a high coherence is required (e.g. DEM generation, tectonics) would gain from using data collected at night. Quantifying this gain in the different applications is beyond the scope of this report since it requires a good knowledge of the key issues in each case. The point is however made here that night SAR coherence should be higher on average than daytime (afternoon) coherence. However, spaceborne SAR systems usually impose high power requirements on the spacecraft bus, and therefore night operations are usually kept to a minimum because they run only on the spacecraft internal batteries: the spacecraft solar panels being in eclipse at night, they do not provide any additional power. Again, the scientific interest goes against more practical issues of spaceborne SAR systems.

An example: retrieval of wheat height from the coherence

In order to assess the impact of the coherence variability on the retrieval of crop parameters, it is interesting to use as an example two published studies which have derived empirical relationships with the wheat height. The following two linear relations between the wheat height h in cm and the coherence γ originate from [13] and [15]:

$$h(cm) = 140 - 170 * \gamma \tag{7.13}$$

$$h(cm) = 153 - 185 * \gamma \tag{7.14}$$

For example, a coherence value of 0.5 from a wheat field translates into wheat height of 55 cm from Equation (7.13) and 60.5 cm from Equation (7.14). The two estimates are close together, which *a priori* indicates their capability to reliably predict crop height. However, the analysis above has shown that a single coherence value can depart from the mean that would be obtained if many samples were available. From Equations (7.13) and (7.14), a $\pm$ 0.1 variation of the coherence translates into a crop height accuracy of $\pm$ 34 cm and $\pm$ 37 cm respectively. In other words, the variability of the coherence due to unpredictable wind conditions infers that the linear relationships with crop height are not suitable to make accurate predictions. In [13], it is stated that the linear relation with crop height is not accurate, due to the variability of the coherence. Additional studies should be made

on this particular point, but the analysis here tends to support the conclusion that wheat height cannot be accurately retrieved from the coherence alone, unless some additional information is known, such as the wind conditions, the day of year, or the wheat type.

7.7 Variation of the coherence in the wheat growth season based on ERS data and model estimates

In the previous section, the coherence estimates γ between May and August were presented in order to illustrate their variability due to the wind conditions. However, the variation of γ with time was not analysed and related to the changes of the wheat phenotype throughout the season. This section aims to make this analysis, and to compare the coherence variation predicted by the model to coherence obtained from ERS-1/2 Tandem data.

There are two objectives to this section: first, relate the coherence time variation to features of the wheat phenotype in order to assess its capability for wheat monitoring, putting aside for the moment the sources of variability discussed in the previous sections. The second objective here is to make a comparison of the ERS-1/2 Tandem coherence with the model outputs for validation purposes. So far the coherence model has provided estimates which have not been compared to outside data sources and therefore have not proven their accuracy. Comparison with Tandem coherence will provide a partial validation of the model.

Section 7.7.1 presents the set of ERS SLC data available from the area surrounding Cranfield University and details the necessary processing leading to a series of coherence images covering a period from June 1995 to May 1996. Section 7.7.2 shows the coherence variation obtained from the ERS data, and compares it to the estimates provided by the model.

7.7.1 Extraction of coherence and backscatter intensity images from the ERS-1/2 Tandem data

This section describes how the coherence images are obtained from the ERS-1/2 Tandem SLC data. The location and the extraction of the region of interest (Cranfield) is described. The ISAR software used to generate the coherence image is briefly presented, as well as the standard techniques used to extract information from the coherence and intensity images.

Available Tandem data pairs

The coordinates of the Cranfield campus are 52°04.06'N-0°37.1'W. The ERS passes over this point were obtained using a software provided by ESA-ESRIN, called *Descw* [69]. The software gives all passes when SAR data were actually collected over the area of interest. The SLC data are recorded in a series of rectangular areas on the ground, labelled in a track/frame coordinate system. As the satellites have a

35-day repeat cycle, they repeatedly follow the same tracks on the Earth's surface, which are numbered to give the track coordinate. Each track is divided in several frames which are also numbered and give the frame coordinate. Several track/frame combinations can contain a given area, as is the case for Cranfield. Figure 7.12 shows the available track/frame combinations which contain the Cranfield area.

Figure 7.12: Available track/frame combinations of the ERS satellites which contain the Cranfield area, represented by the small square area at the centre of the 6 track/frame footprints. This map is obtained with the *Descw* software.

The frames 3 and 6 on Figure 7.12 correspond to an ascending pass of the satellites and are therefore oriented differently from the others, which correspond to descending passes. *Descw* outputs a list of all available data over the defined area and using the date and time information, it is possible to list all available Tandem pairs. The pairs acquired on a descending pass were recorded at the end of the morning, while the acquisition time of the data for the ascending passes is about 10 pm, i.e. at night time. The following analysis concentrates on data from descending passes mainly in order to build a database of images with the same characteristics. Appendix H.1 gives details on the image pairs acquired and

processed for the research. Table H.1 shows that the Tandem data (13 pairs from descending passes + 2 from ascending passes) cover the end of the growth season 1995 and the first half of 1996. Most of the image pairs ordered and processed correspond to interesting periods of the growth season, i.e. in spring and summer.

Data extraction

The SLC data is delivered by ESA-ESRIN on magnetic tapes. They cover a quarter of a full frame (complete frames can also be ordered and are referred to as SLCI data). The tapes are delivered with a draft paper version of the intensity image of the quadrant which allows to approximately locate the area of interest on the image. The user can then read from the tape the desired number of lines and columns, starting from a specified origin.

The study is based on the agricultural fields surrounding Cranfield. The area for which the coherence images were generated contains 300 pixels in ground range and 1500 pixels in azimuth. With an approximate pixel size of 25x5 m, the surface area covered by these images is about 7.5x7.5 km. However, in order to build a more general database of SAR SLC data of the area and to allow for other areas to be studied in future research projects, it was decided to extract and store from the tapes a sub-scene of 600 columns x 3000 lines, covering a surface area of 15x15 km. For reference, the quadrant sizes, the exact position of Cranfield in the quadrants, and the exact position of Cranfield in the 15x15 km extracts are given in Appendix H.2.

The analysis below concerns 300x1500 pixel sub-scenes of the 15x15 km extracts, centred on the Cranfield area. The intensity images are created from the real and imaginary part provided by the SLC data. The coherence images are generated with the ISAR software.

Generation of the coherence images with ISAR

The ISAR interferogram generator software [46] takes as inputs two SLC data files and a series of orbital and computational parameters, which are detailed in Appendix I. The main outputs of ISAR are:

- the interferogram, obtained by multiplying the second SLC image by the complex conjugate of the first image,
- the coherence image,
- two slope files (in the range and azimuth direction), estimated from the interferogram,
- a modified first image, stretched and shifted to fit the first image.

Image processing techniques

After the ISAR runs, some processing is required to access useful information from the coherence and intensity images. The coherence and intensity data files were

imported into Erdas Imagine for display and visual analysis. A conversion from real/imaginary to magnitude/phase is required prior to the import, as well as an averaging of five lines in the azimuth direction in order to remove the distortion in azimuth and be able to compare features on the images with actual characteristics of the real terrain as displayed on a geographic map. The conversion to magnitude/phase and the five line averaging were performed by simple C programs.

Once imported, two intensity images from the same Tandem pair are co-registered using the 'geometric correction' module of Erdas Imagine. This module requires the definition of ground control points on each image. The permanently bright scatterers were chosen as control points. The co-registration of the 26 intensity and 13 coherence images created from the 13 ascending pass data sets is necessary to compare the variation with time of pixel values representing the same target area on the ground.

Average backscatter intensity and coherence image

Figure 7.13 shows the backscatter intensity and coherence image obtained by averaging all available images (13 pairs of images for the backscatter intensity and 13 coherence images, from June 1995 to May 1996) after co-registration. The red cross on the images shows the wheat field from which the coherence will be extracted later in this section. It is also the wheat field where the wind and wheat motion measurements were made.

The general aspect of the backscatter intensity and coherence images shows that they provide different information. On the backscatter intensity image the runway system of the airfield appears clearly at the bottom right corner, as well as the built-up area corresponding to the University, left of the runways. Comparison with a geographic map shows that the other groups of bright pixels in the image correspond to other built-up areas such as individual farms or small villages. These permanent scatterers are useful for image co-registration. Some field structure also appears in the intensity image but is not particularly clear, mainly because the image results from an average of 26 images covering a period of about one year. Individual fields have variable properties over such a period as far as backscattering properties are concerned: the roughness, moisture, and content of the scattering medium vary greatly in one year, particularly in an agricultural region.

For the same reasons the field structure on the average coherence image is not very pronounced. However, the areas permanently yielding low coherence appear clearly. Comparison with a map shows that areas of low coherence correspond to groups of trees and small woods on the map. The swaying of trees, even under quiet wind conditions and in winter when no leaves are present (most of the forest in the region is deciduous) is sufficient to displace the scatterers by more than a wavelength at C-Band. This results in a complete loss of coherence which shows on the image. Some regions of high coherence are also present on the image, at the same location as strong backscatter on the intensity image. The built-up areas yield high coherence because of their very static nature.

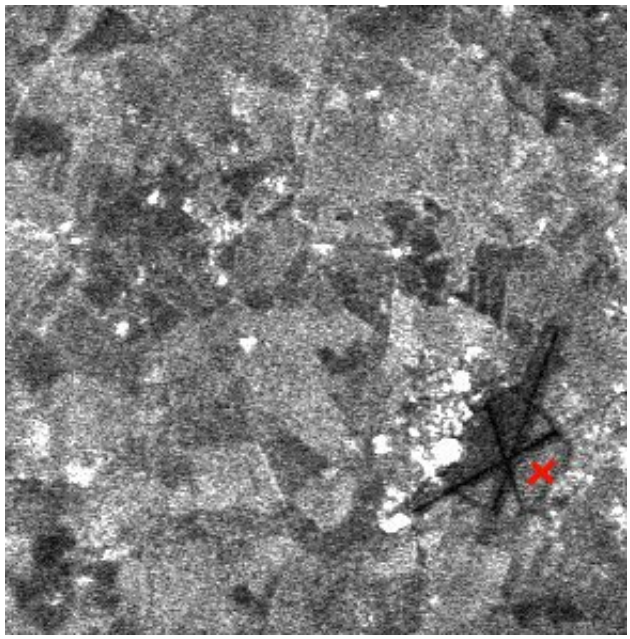

(a) Average backscatter intensity

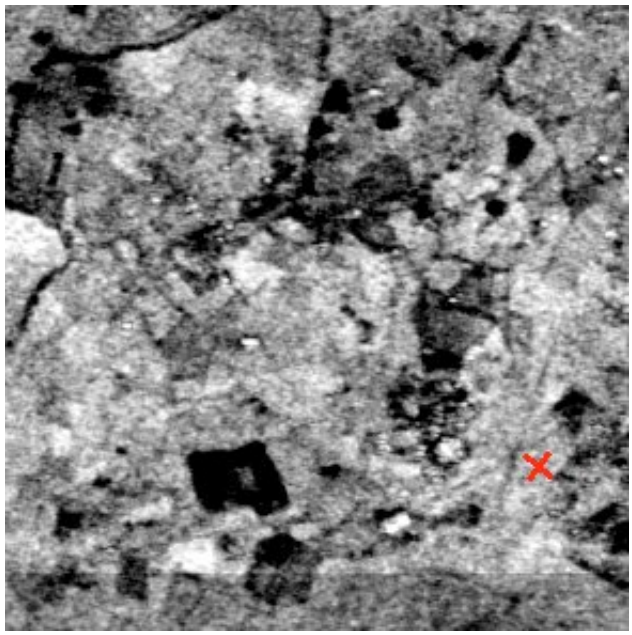

(b) Average coherence

Figure 7.13: Backscatter intensity and coherence image of the Cranfield area, obtained from averages of the 13 pairs of images available, from June 1995 to May 1996

7.7.2 Comparison between the ERS-1/2 Tandem coherence and the model estimates

Temporal variation of the Tandem coherence

The cross on Figure 7.13 marks the wheat field from which the coherence estimates were obtained. Prior to the analysis, the coherence bias at low values was corrected

for, using the method summarised in section 2.2.4 and detailed in [28]. The coherence values of all pixels in the field are averaged in order to get a single value for the crop field. 13 values were obtained, corresponding to the 13 coherence images from the descending passes of the ERS satellites. They are plotted against time in Figure 7.14. The data points are numbered from 1 to 13. The figure also shows the coherence value obtained by the same process over a portion of the Cranfield airfield covered by short grass.

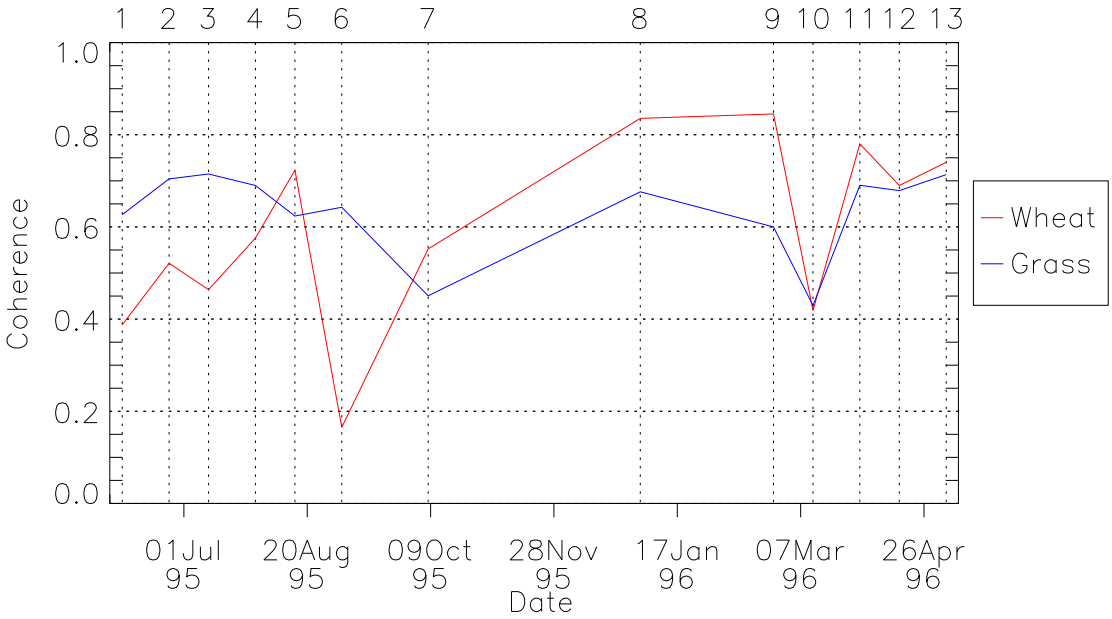

Figure 7.14: Temporal variation of the coherence for a wheat field and grass obtained from ERS-1/2 Tandem data

In winter, the agricultural field is kept as a bare surface and the corresponding coherence values are higher than those obtained from a grassland area, with the exception of the coherence from the March $12^{th}/13^{th}$ 1996 pair (point 10) which will be discussed later in this section. The coherence values for the wheat field are lower in the summer 1995, as expected from a fully grown plant compared to short grass. The low coherence obtained on September $3^{rd}/4^{th}$ 1995 (point 6) most probably corresponds to the ploughing of the field between the two radar passes, resulting in a radical change of the scattering properties of the surface and therefore yielding low coherence. The coherence value obtained on March 31^{st}/April 1^{st} 1996 (point 11) is higher from the crop field than from the grass, although the difference is not as important as in the middle of the winter. About 15 days later, the coherence values on both fields are comparable (April $16^{th}/17^{th}$, point 12), and it is also the case another 15 days later (point 13). This behaviour can be explained by the change in the crop field from a bare surface to a sparsely vegetated surface typical of an early growth stage of the plant. Although it is difficult to confirm this point with no corresponding ground truth data, it is reasonable to suppose that the coherence values from March to the beginning of May indicate indirectly the emergence of the crop in the agricultural field. It is likely that the emergence occurred between points 11 and 12, i.e. between April 1^{st} and April 16^{th}.

It appears that wheat at an early growth stage cannot be differentiated from grassland with the coherence values. This is not surprising, considering that a young crop does not fully cover the surface and therefore most of the radar incoming wave reaches the surface. In a young wheat field, most of the scattering is surface scattering, as for surfaces covered by short grass. In both cases the coherence is therefore expected to be fairly high and identical. When the crop grows, it finally yields the behaviour observed in the summer points of the graph, i.e. lower coherence than for the grass area. The second point to make is that shorter wavelengths should in principle be more suited to crop emergence detection as the coherence would be lost for smaller amplitudes of the crop motion and a greater fraction would be scattered by the crop.

On March $12^{th}/13^{th}$ 1996 (point 10), the coherence values for the crop field (simply bare soil at the date of the image) and the grass field are identical and low. This particular feature is thought to be due to the presence of a layer of frost on the surface at the time of the satellite passes. The air temperature is continuously recorded by the automatic weather station at Cranfield. The analysis of the weather data shows that the temperature was below 0°C during the two nights preceding the recording of the SLC data, still 0°C at 11am (the time of the ERS pass) on March 12^{th}, and 0.8°C on March 13^{th}, same time. The supposition here is that the surface was covered by a layer of frost (possibly in a thawing state for the second date) which changed its dielectric properties, and consequently the backscattering properties of the surface between the two dates. This hypothesis would explain the low coherence for the two fields.

The temporal variation of the coherence obtained from ERS-1/2 Tandem data shows that several features affecting a wheat field can be potentially detected, from farming activity to emergence in spring. It also shows how the coherence is influenced by meteorological events such as freezing. The analysis above is a good summary of the positive and negative sides of the use of coherence: it carries useful information about the properties of the Earth's surface but is affected by unwanted effects such as the weather conditions. The next section goes one step further in the analysis of the coherence, and attempts to relate its variation in the growth season to the changing properties of wheat from May to August. The Tandem coherence and the model outputs presented earlier are used for this purpose and compared to each other.

Comparison with the coherence estimates from the model

The coherence estimates from the model were presented in Figure 7.11. They cover a period from May 1^{st} to August 10^{th}. The Tandem coherence used here for comparison is the value obtained on May $5^{th}/6^{th}$ 1996 and from June 5^{th} to August 16^{th} 1995. Using the coherence value from May 1996 and the values from 1995 assumes that the wheat has similar biophysical properties in the two successive seasons. It also supposes that these properties are similar to those of the wheat used in [51] to generate the scattering contributions presented in Table 7.3, which are at the basis of the coherence estimates by the model. Section 6.3 has shown that the wheat height from the same field follows a comparable time variation in two successive years, so it is reasonable to assume that the biophysical properties of the same wheat field

in 1995 and 1996 are similar and therefore can be used to represent the crop in a single growth season.

It is also possible to indirectly assess the assumption that the wheat used for the estimation of the scattering contributions in [51] has similar properties to the wheat from which the Tandem coherence was obtained. In [51], the RT2 model used the characteristics of wheat grown on the Flevoland test site in the Netherlands. In [13], data from the same site were used, and in particular the variation of the wheat height in the growth season was presented: the average wheat height in the Flevoland test site increases linearly and reaches its maximum approximately on June 10^{th}, with a maximum of about 90 cm. Figure 6.2 showed that the wheat height on the field from which the Tandem coherence is calculated (field 1) reaches a maximum of about 80 cm on June 20^{th}, both in 1997 and 2000. Assuming that these properties were similar in 1995 and 1996, when the Tandem data were collected, there is a difference of 10 days between the dates when the wheat reaches its full growth in the Flevoland site and the Cranfield site. The difference in maximum height is about 10 cm. These differences should be kept in mind when the coherence variations from the Tandem data and from the model estimates are analysed.

Figure 7.15 reproduces the variation of the coherence estimates from the model, as already displayed in Figure 7.11. Since the Tandem data are obtained at 11am, the model estimates used here for comparison are those derived from the morning category (see Figure 7.11(b)). The Tandem coherence is also reproduced in Figure 7.15. Note that no line is drawn to join the Tandem coherence values in order to highlight the fact that they do not follow a chronological order: the point on May $5^{th}/6^{th}$ is from 1996, and those from June to August are from 1995.

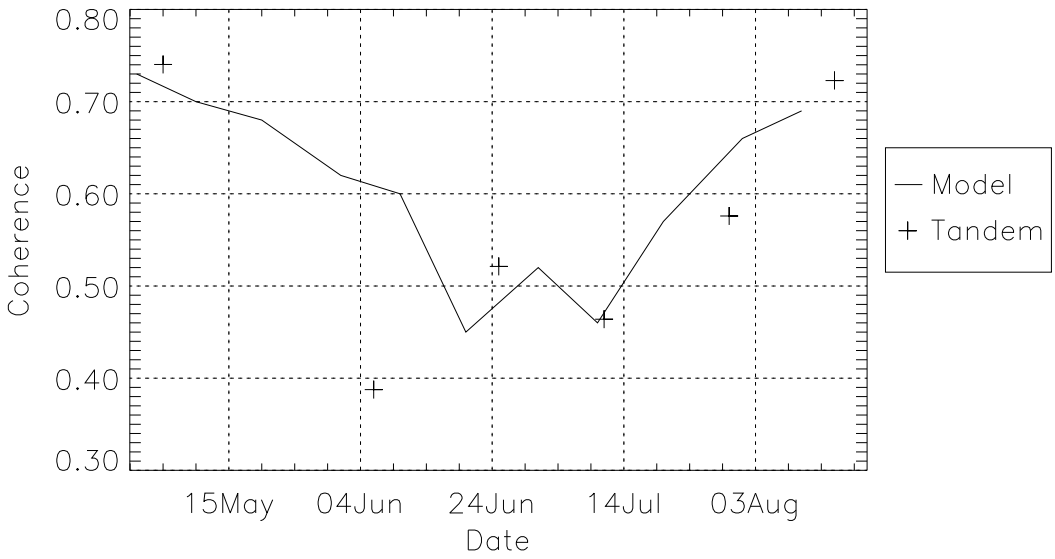

Figure 7.15: Temporal variation of the coherence for a wheat field: estimates from the coherence model and from the ERS-1/2 Tandem data for the Cranfield test site in 1995-96

The coherence estimates from the model for each date represent an average of 50 values generated from wind conditions randomly chosen and made to follow the distribution of the wind speed obtained from the weather station data. This was

explained earlier in section 7.6.2. At the beginning of the growth season, from May to the first half of June, the model outputs show that there is a regular decrease of the coherence from about 0.7 to 0.6. This decrease can be related to the progressive growth of the wheat, which is subject to an increasing motion amplitude due to its increasing height. From the second half of June, the wheat has reached its maximum height. The model estimates show a sharp drop of the coherence from June 10^{th} to June 20^{th}, from γ=0.6 to γ=0.45. From the scattering contributions given in Table 7.3, it appears that June 20^{th} is the date at which the scattering from the wheat heads becomes the dominant contribution to the total backscatter. Then from June 20^{th} to July 10^{th}, Figure 7.15 shows that the coherence remains approximately constant at about 0.5. It is not clear from the scattering contributions why the coherence on July 1^{st} is higher than for its neighbouring points. From July 10^{th} to the end of the season, there is a steady increase of the coherence, due to the increase of the surface scattering contribution. This increase is explained by the fact that, as the wheat dries in July and August, its volume backscattering coefficient decreases, and its attenuation of the incoming radar wave decreases, leaving a higher backscattering contribution from the surface. This increasing contribution of surface scattering appears in Table 7.3, and its causal relation with the wheat drying is acknowledged in [53]. It is interesting to note that the model shows that the coherence to expect from a dry wheat field is similar to coherence early in the season, when the crop is not fully grown ($\gamma \approx 0.7$). Therefore the relative contributions of surface scattering and volume scattering from the vegetation are similar in May and August, although the wheat is in a very different phenotypic state.

The coherence obtained from the Tandem data is represented in Figure 7.15 by the crosses. The comparison with the model is limited since only 6 data points are available from the Tandem data. However, there seems to be a good agreement between the model and the true data: the Tandem coherence shows a decrease of coherence from May to June and the increase in the drying period, in July and August. The most important difference between the model and the Tandem coherence occurs for the June $6^{th}/7^{th}$ data point: the Tandem coherence at that date is about 0.4 and it is 0.6 from the model. This difference can have two origins. The first possibility is related to the difference between the wheat description used by the model and the wheat from which the Tandem coherence is obtained. The former (from the Flevoland test site) is higher and reaches its peak height earlier than the latter (from the local Cranfield site). A peak height reached earlier for the wheat used by the model can in principle translate into a drop a coherence at an earlier date than for the Tandem coherence. Figure 7.15 shows that the opposite situation is observed: the drop of the Tandem coherence occurs earlier. So the difference in wheat growth does not explain on its own the difference observed at the beginning of June, but it is possible that the wheat used in the model has different bio-physical characteristics than the wheat from the Cranfield site. This would explain the coherence difference. The second possible explanation is linked to the fact that the wheat at Cranfield on June 6^{th} and/or June 7^{th} 1995 experienced particularly high wind conditions inferring higher temporal decorrelation. This is to relate to the point made earlier in this chapter that the coherence from a wheat crop is subject to a high variability linked to the weather conditions. More data would be required

to make a definitive judgement on this point: either weather data from June $6^{th}/7^{th}$ 1995 are needed, or more information about the wheat bio-physical characteristics in the Flevoland and Cranfield sites.

Apart from the data point on June $6^{th}/7^{th}$, there is a general good agreement between the model estimates and the Tandem coherence. There are two ways to interpret this good correspondence. First, it can be seen as a point which strengthens the validity of the coherence model. It is based on the artificial separation of the scattering medium into a static and dynamic part, and therefore does not represent the true physical reflection, absorption, and transmission properties of the vegetation, which would be accounted for more rigorously in a coherent backscatter model. In addition to this, section 7.6.1 pointed out that there are several sources of uncertainty which affect the accuracy of the numerical simulations performed with the coherence model. These uncertainties are linked to the limited amount of data from which empirical relationships between the weather station wind data and the wheat motion were derived. For these reasons, the model is based on a series of approximations and the good agreement with the Tandem data can be viewed as a point which partially validates them. In turn, the analyses and conclusions of the previous sections can be trusted more strongly than if the model did not agree with the Tandem coherence data.

However, the compatibility between the model outputs and the Tandem data also raises questions about the model validity. The simulations presented in section 7.6 showed that the coherence is expected to be very variable with the wind conditions at the time of the radar passes. For this reason, it could have been expected that the Tandem coherence, which is obtained from a single pair of radar passes, would deviate more significantly from the model than it actually does in Figure 7.15. It is possible that the coherence variability predicted in section 7.6 is not found in practice, due to additional mechanisms of the coherent scattering which have not been accounted for. Another explanation is that the wind conditions at the time of the ERS-1/2 passes were such that they yielded coherence values near the average predicted by the model. It should be noted however that the agreement between the model and the Tandem data is not consistently good, as on June $6^{th}/7^{th}$ as already stated, and also on July $30^{th}/31^{st}$, where the difference is about 0.1. More Tandem coherence would be required in order to make a more definite judgement on this point.

7.7.3 Suggestions for a complete validation of the model

No attempt is made here to perform a more rigorous validation of the coherence model with SAR data, because it would require the availability of a number of data sources which are not accessible. However, it is important to identify these data sources so future developments of the work presented here can collect them and build on the experience gathered during the research. This section identifies the methodology to apply and the necessary data to perform a full or partial validation of the coherence model. Most of the considerations presented here apply to the validation of other coherent backscatter models as well.

Data concerning the wheat phenotype should be collected throughout the growth

season, from March to August mainly. The data required includes the stalk, leaf and wheat head number density, their orientation, moisture content, and dimensions. Surface data is also required (roughness, correlation length, moisture and corrugations, if present). Wind and wheat motion data should be recorded, as often as possible during the growth season, ideally several times a week, in order to cover a maximum number of wind conditions and to follow the changes of the wheat characteristics. Simultaneously with the measurements of wind data and wheat motion, SAR data should be collected, from which coherence can be computed. Since the model can in principle be applied to several incidence angles and wavelengths, SAR data covering different values of these two parameters are desirable.

From the wheat phenotype, and the wind and motion measurements, coherence estimates from the model can be made, following the methodology presented in this report. Comparison of these estimates with the coherence obtained from the SAR data can provide a validation analysis of the model.

From a practical point of view, it is very unlikely that a complete validation campaign can be achieved as it is described above, because of the heavy resources it requires. The necessary resources are both financial and temporal, and can be only justified if the coherence shows a serious potential to improve agricultural monitoring issues from remote sensing sources. This potential will be discussed in the next section. From a technical point of view, obtaining SAR data recorded simultaneously with the wind and wheat motion measurements is difficult with spaceborne SARs, possibly easier with airborne SARs.

From the analyses presented in this chapter, it seems that a coherent backscatter model aiming to make accurate estimates of the complex backscatter from a vegetation medium needs to incorporate motion information about this vegetation. Therefore, validation of such models necessitates some motion measurements, similar to those presented in this report. The difficulty of obtaining these measurements in conjunction with SAR data shows that the development of coherent backscatter models is difficult not only from the point of view of the computational implementation, but also because of the issues related to model validation.

7.8 Conclusion on the use of coherence for wheat monitoring

Several points were made in the previous sections, concerning the coherence and its characteristics with respect to the radar parameters, the wind conditions, and the wheat characteristics. This section summarises the most important issues raised in order to have a global view of the coherence, and of its capability for crop monitoring.

7.8.1 Summary of the key parameters affecting the coherence

This current chapter started by including the knowledge gathered from the wheat motion measurements in the initial coherence model presented in Chapter 3. Modifications concerned the inclusion of several cells of coherent motion to represent the

spatial correlation of the wheat positions observed from the measurements, and the use of Gaussian distributions to represent the displacement of the wheat scatterers in the radar look direction.

Radar resolution

The resolution of the radar affects the number of independent cells used in the coherence model, and section 7.2 showed that a decrease of the coherence with decreasing resolution can be expected. The most significant result of the study is that the coherence decrease with resolution reaches an asymptotic value for resolutions of about 4x4 m. It is therefore expected that the resolution does not have a significant effect on current spaceborne SAR systems, as far as the coherence is concerned. It is also pointed out that the variation of coherence with resolution is very difficult to verify in practice with SAR data.

Radar wavelength

More directly relevant to the coherence from agricultural crops is the influence of the radar wavelength. Section 7.3 showed that using a C band SAR results in intermediate coherence levels which offer the highest sensitivity to crop motion. Section 3.2 showed that C Band was also most suited from the point of view of the backscatter intensity, so it appears that it is the most suitable choice overall for the remote sensing of wheat. The choice of a particular wavelength within the C-band can have a significant effect because the coherence variation from wavelengths of $\lambda = 3$ cm to $\lambda = 7$ cm covers a wide range of values. Future spaceborne SARs having as one of their mission objectives the study of agricultural crops should use the C-band, and preferably the same wavelength as the current systems such as the SAR on ERS or in the near future on ENVISAT ($\lambda = 5.66$cm), so it is possible to compare the coherence levels obtained from them.

Radar look direction

The study of the influence of the incidence angle on the coherence produced similar conclusions. Low incidence angles result in a greater sensitivity to surface scattering processes, which are not useful for the remote sensing of crops. On the other hand, very high incidence angles give consistently low coherence. For that reason intermediate values between 20° and 30° offer a good compromise as they yield intermediate coherence. However, at these intermediate incidence angles, the coherence sensitivity to local slopes on the surface is maximum, meaning that an accurate interpretation of the coherence for crop monitoring purposes requires the knowledge of the local topography. It was shown that a $\pm 5°$ deviation from the horizontal results in a change of coherence of about 0.3 for a fixed set of wheat configuration and wind conditions. Such a variation is significant enough for example to change the coherence thresholds in land-use classification applications, and to affect the accuracy of empirical relationships with crop parameters. The influence of the azimuth angle on the coherence is critical if all wheat elements in the field move in a preferred direction. However, measurements have shown that this is not particularly the case

for wheat. The azimuth angle is therefore not expected to significantly change the coherence from several wheat fields subject to different mean wind directions.

Repeat time

The time between the two passes of the radar affects the coherence because of changes in the wheat characteristics, and therefore of the dominant scattering mechanisms. Section 7.5 showed that the coherence from a wheat field decreases with increasing repeat time, but the decrease is significant only at the beginning of the growth season, when the wheat is changing rapidly. There is an indication that the coherence also decreases with repeat time at the end of the season, in the ripening phase, but the difference is not significant (0.1 at most). The conclusion here is that the repeat time does not affect significantly the coherence after the wheat reaches its full growth. This conclusion relieves some constraints on the definition of the satellite orbit for spaceborne SARs. However, the study of agricultural crops from InSAR coherence requires as many data points as possible, meaning that a short repeat time is more adapted. If other applications, for which high coherence is desirable, require images taken in spring and summer, then they can use coherence based on longer repeat times, except at the beginning of the growth season, in April in particular. Coherence obtained from two SAR data sets collected before and after harvest will also result in low coherence.

Wind condtions

Section 7.6 estimated the variability of the coherence with the wind conditions. The simulations were based on wind statistics from the summer months. They showed that the coherence from a wheat field with fixed characteristics can vary significantly, depending on the wind it is subject to. The simulation of the possible wind conditions given by the Cranfield weather station statistics showed that, for an average coherence of 0.6, the associated standard deviation on this value is about 0.2. Therefore the coherence from a wheat field obtained with SAR data collected at two dates where the wind conditions are different can differ by this amount (0.2), or more in the extreme cases. Radar parameters discussed earlier are related to the SAR configuration and are therefore adjustable to maximise the return for a particular application of the coherence. However, the variability due to changes in the wind is an intrinsic property of the coherence which cannot be corrected for, and imposes significant limitations on its use for crop monitoring.

Crop growth stage

ERS-1/2 Tandem data were available to provide a temporal variation of the coherence from a local wheat field in 1995 and 1996. The comparison of this temporal variation with the coherence estimates showed a good agreement between the two at most dates. Despite the high variability predicted by the model, the coherence, both predicted by the model and obtained with Tandem data, represents the biophysical properties of the wheat and their changes in the season, from the growth in spring yielding a decrease of the coherence, to the ripening in July and August,

translating into a coherence increase in those months. Two interesting features of the coherence temporal variation are the sharp drop in June and the increase in July/August. The decrease of coherence in June seems to correspond to the emergence of the wheat heads. The coherence could therefore be used as an indicator to monitor this emergence. The coherence in August could be used as an indicator of the most appropriate harvest time. In particular, this technique could prove relevant in large scale farming where different fields can have a growth cycle shifted in time. Coherence values on these different fields could help to identify which areas are driest in the exploitation and therefore most suitable for early harvest. Some additional studies are required on these two aspects in order to see their applicability for operational use and, more importantly, studies should assess if there is a real need for such information provided by the coherence.

7.8.2 Coherence and crop monitoring: potential uses and limitations

The analyses presented in this chapter show that the radar configuration most adapted to the study of agricultural crops is the one which was used by the ERS-1/2 satellites, and which is going to be used in future major SAR missions such as ENVISAT and RADARSAT. However, such a configuration results in significantly variable coherence values, the main causes of variability being the local slopes on the surface and the wind conditions. For the coherence to be accurately used in crop monitoring applications, the knowledge of the local topography and of the wind conditions at the time of the radar passes is required. Information about these two parameters can be integrated into a coherent backscatter model, or into a model such as the one presented in this report, and be used to make more accurate assessments of the crop bio-physical parameters.

The current applications of the coherence for crop monitoring presented in section 2.3 can be divided in two areas: land-use classification and retrieval of bio-physical quantities. For land-use classification, the coherence from a wheat field varies roughly between 0.4 and 0.7, so such a range can be used to define a 'wheat' class. However, it is likely that other crops would yield similar coherence values, so the range [0.4;0.7] is more susceptible to describe a class which encompasses several crop types rather than a single crop such as wheat. For differentiation between several crops, the temporal variation of the coherence is potentially valuable, since the analysis presented in this chapter showed that it follows the changes of the crop characteristics during the season.

The retrieval of bio-physical parameters from the coherence presents more challenges than the classification problem. Using the knowledge of the wind conditions and topography in a coherent backscatter model is identified as a necessary requirement if accurate retrievals are needed. The use of empirical relationships without *a priori* information of the local terrain and the meteorological conditions is not expected to lead to accurate results in all cases. The term meteorological conditions used here encompasses the wind, but also rain and temperature, especially near the freezing point.

The present research focused on a single crop, and generalisation to other types

should not be made without the help of similar studies for other agricultural products. Differences in the coherence from wheat and from other crops can be due to different motion characteristics and different scattering contributions to the total backscatter intensity. Differences in motion can be related to height or to the amount of mechanical interaction between neighbouring plants. For example a crop such as rape at its full growth stage is expected to have stronger interactions with its neighbours than wheat because it extends vertically as well as horizontally. Differences in the scattering contributions are related to the reflection, absorption, and transmission properties of the crop of interest. These properties depend on the development stage of the plant and on the density and geometry of its elements. The temporal variation of the coherence showed in section 7.7.2 emphasised the fact that the principal features of the wheat development in the season leave a noticeable effect on the coherence. This is likely to be the case for other crops, opening the possibility to follow the main stages of the development of crops with the coherence.

This last point is not necessarily in contradiction with the fact that the coherence was found to be very variable with the weather conditions. However, because of this variability, SAR interferometric data should be collected as frequently as possible in order to limit the impact of isolated meteorological events which change drastically the coherence, such as rain, frost, or strong wind. For wheat, the change from April to August is such that several coherence data points should be available every month in the summer. The constraints imposed by this requirement for data collected at short time intervals may not be acceptable for other applications of SAR data, because of the orbital restrictions implied. Crop monitoring with SAR interferometric coherence would require an almost dedicated spaceborne SAR system, or an airborne SAR, with the high costs associated to it.

Even if, in practice, an accurate crop monitoring system based on the use of coherence does not seem feasible because of operational constraints and of the intrinsic variability of the coherence, the study presented in this chapter still presents some interests. It shows that the coherence can be used to retrieve information about the surface, either through classification, or via the use of coherent backscatter models. It was shown that the modelling approach is a necessary step towards the accurate use of the coherence, on its own or in conjunction with the backscatter intensity. In addition to this, the knowledge of the conditions which maximise the coherence is useful for SAR applications based on the use of interferograms. Being able to estimate the expected coherence from a vegetated surface given its phenotypic state and the weather conditions can help to make a pre-selection of the most suitable pairs of SAR data which should be used for a particular application.

7.9 Suggestions for follow-on work

The approach adopted in this chapter presents some strengths and weaknesses, and raised some specific points requiring further analysis. They are summarised in this section, which aims to provide a critical view on the methodology and results of the research.

Wheat is the crop on which the main focus of the research was placed. The reason for this choice is that the objectives of the study were mainly to demonstrate the

feasibility of *in situ* measurements of crop motion and the methodology to integrate them into a model providing more accurate insights about the different parameters which influence the coherence from agricultural fields. Because the focus of the research was to demonstrate the methodology more than to give a complete study of the coherence from a series of different crops, it was decided to focus on a single crop type. Wheat was chosen because of it is economically significant, it was convenient to observe locally at Cranfield University, and it has a relatively simple geometry. However, it is suggested here that the motion of other types should be measured and that their relation with coherence should be studied in a similar way to the approach followed here for wheat. Studying other crops would allow to identify key differences which could be used to differentiate several types of fields, from the coherence alone or as a complement with other data sources.

Measurements on wheat should be made more extensively throughout the growth season, especially at the beginning of the growth season, when data were missing in the present study. The coherence model used extensively in this chapter finds its roots in previous research made at Cranfield University, and was developed and applied in the project for that reason. It is based on a statistical representation of the scattering processes taking place inside the vegetation medium, rather than on a physical representation. The modelling approach would benefit from validation with SAR data collected simultaneously with the motion and wind measurements. It would be very valuable for the research to obtain complex SAR data from which coherence can be extracted and correlated to motion characteristics measured in parallel. The most sensible approach to fulfill this need is via the use of an airborne SAR operated in collaboration with research groups interested in other applications of SAR data.

The motion of wheat is measured on a single point on each plant because the video camera system cannot accurately retrieve the position of targets placed inside the canopy. For that reason modelling the motion of wheat stalks and leaves requires some additional assumptions based on the measured displacements of the wheat head. Wheat being a rather simple plant with a clear vertical structure, the motion of its constituents can be retrieved with reasonable accuracy from theoretical considerations on its mechanical properties. This may not be the case for all vegetation types having more complex structural properties. The adaptability of the methodology demonstrated here for wheat to other crop types is a potential area of future research opened by the project.

It is probable that a coherent backscatter model would give a more accurate representation of the complex backscatter to expect from a crop than the statistical approach developed here. However, building an accurate coherent model requires full-time research which would not have allowed to develop the other interesting aspects presented in this report, in particular concerning the motion measurements. The use of a coherent backscatter model is acknowledged here as a potential improvement to the methodology used in the research. However, it was shown that the motion characteristics of crops must be accounted for in coherent modelling, and for that reason the three-dimensional measurements of crop displacements represent an indispensable source of information. A comparison with more sophisticated coherent backscatter models could also be made to test the validity of the simplified

approach used in this study.

Chapter 8

Conclusion

The complex degree of coherence in SAR interferometry is an indicator of the change in the complex backscatter between two images of the same area on the surface. If the two SAR data sets are collected at a different time, the coherence is sensitive, among other parameters, to the temporal changes which affect the scene between the two passes of the radar antenna. When the area on the Earth's surface is covered by vegetation (trees or crops), the coherence is affected by the wind induced motion of leaves, stalks, etc... For fixed wind conditions, this motion depends on the vegetation type and on the growth stage, so coherence has the potential to provide useful information about vegetation parameters. Past studies have attempted to use this property of the coherence for forestry and agricultural applications. They showed that the coherence is indeed sensitive to parameters such as forest biomass or crop height. However, they also point out that observations of plant motion would be a valuable source of information which models could use to quantify the temporal decorrelation mechanisms and make a more precise analysis on the use of coherence for forestry or agricultural applications.

The research presented in this report demonstrates a methodology which can be used to make accurate measurements of the three-dimensional position of crop elements and of wind velocity at canopy height. These measurements were made in summer 2000, in a wheat field local to Cranfield University. The data collected were used in a coherence model from which the applicability of using coherence for agricultural applications was analysed.

8.1 Summary of the report

Three-dimensional motion measurement system

The three-dimensional position of moving objects was achieved with two digital video cameras imaging the same target at two different angles. The viewing geometry and principles of stereo vision have long been applied to a wide range of applications, but the originality of the method developed in this research lies in the fact that it uses videos cameras normally designed for a more general public use and not for scientific measurements. This is achieved by the recent availability of digital video cameras and the possibility to transfer video data on a computer for processing. An object

of high contrast with the background is tracked here by correlating its pixel values to a user-defined mask, specified in a Windows based program. After tracking, the pixel coordinates defining the position of the object in the two video images is translated to an absolute position in a fixed reference system for every frame of the video sequence, giving the three-dimensional locus of the tracked target. For that purpose, calibration procedures are required, in order to determine the position of the cameras in the fixed reference system and the relation between pixel coordinates in the image and angular values with respect to the camera viewing axes.

The use of consumer digital video cameras provides a cost effective way to make three-dimensional measurements of wheat motion *in situ*. The three-dimensional locus of wheat elements was measured at several dates, on several targets at each date. The potential improvements on the system are the inclusion of a capability to download and perform partial processing of the video data in near real-time. Additional processing of the video data was shown to be very useful for an improved tracking of objects in the image. The cost of the video equipment is likely to come down in the future, as well as its efficiency and capabilities are likely to increase. From a more global perspective, the measurement system presented in this report is an example of a potential new trend in the way scientific experiments in general can be designed, whereby new technologies aimed to a large public can be used efficiently for scientific uses, as opposed to the more traditional approach where dedicated scientific instruments are adapted for commercial release.

Wind velocity measurement system

The measurement of wind velocity requires that the wind is determined along the 3 axes of a coordinate system. For that purpose, it is measured by a set of 3 anemometers oriented at different angles. The anemometers used for the research were available at Cranfield University, and have been used for past projects in micrometeorology. They are vane anemometers which output an electric signal composed of a number of pulses proportional to the rotation of the vanes, and therefore to the wind speed. Prior to the use of the anemometers to make measurements in a wheat field, it was necessary to design an acquisition system to replace the old existing equipment. The data acquisition system receives the electric signal sent by the anemometers, and counts the number of pulses in a fixed time interval, in order to translate it into a pulse rate and consequently a wind speed. The system uses a data acquisition board capable to receive analogue and digital inputs, and a clock board allowing the selection of the adequate sampling frequency. The associated software counts the number of pulses acquired via the acquisition board in a fixed time interval given by the clock board. Particular attention was paid to the capability of the system to make measurements and store them in real time. The real time capability of the software is only limited by the sampling frequency. The wind measurements were made at 5 Hz, allowing the acquisition software and hardware to function satisfactorily for the entire range of wind velocities measured at canopy height. The measurement of wind velocity was realised in a wheat field, simultaneously with the wheat motion measurements. The system is suitable for outdoors use and can be managed by a single person, which is an important aspect as it reduces its running cost.

Data measurement campaign and analysis

Synchronised wheat motion and wind data were acquired on 6 occasions from May to August 2000, in a field local to Cranfield University. The data are provided in this report, in the form of text files stored on the CD attached. The number of wheat elements measured accurately at each date depends on the wind conditions and on the orientation of the tracked targets (red labels glued on the wheat elements) with respect to the camera viewing angle. Only elements on top of the canopy can be tracked by the system: these elements are wheat leaves in the early season and wheat heads at a later growth stage. One minute of video data was processed at each date and analysed in conjunction with the wind data, collected at wheat canopy height and about 1 m above the canopy.

The wind at canopy height is variable, both on spatial and temporal scales. On the spatial scale, the mean wind speed increases with increasing vertical height, and is also variable horizontally. The interactions between the wheat and the wind seem to affect the vertical component of the wind velocity. The variability of the winds tends to degrade the potential relationships showing the causal effect of wind forcing on wheat motion, because the wind measured by the anemometers can be significantly different from the wind which is causing the tracked wheat elements to move. The wind data collected by the Cranfield Automatic Weather Station are used to calculate the probability of certain wind conditions to be found in the summer, and at a particular time of day. They show that lower wind conditions are found in the summer, and at night.

The wheat motion data show that the wheat elements move mainly in a horizontal plane, but not particularly in the direction of the mean wind they are subject to. The three-dimensional coordinates of the tracked elements can be translated into a probability distribution of displacement in slant range, which is in turn used in the coherence model. The time variation of the wheat position shows an oscillating frequency of about 1.2 Hz, and shows that the motion of wheat plants separated spatially is correlated. The spatial extent of this correlated motion is quantified by a correlation distance, which is of the order of half a metre. The average wind speed relates well and linearly to the wheat motion amplitude, but the comparison of the time variations of the two synchronised data sets does not yield consistently good results. This is due mainly to the variability of the wind velocity at canopy height.

Coherence modelling

In order to assess the relation between the coherence and a series of radar parameters and wind conditions, a statistical estimator was developed. The coherence model is based on a Monte-Carlo simulation of pixels representing the complex backscatter from the vegetation. Two sets of pixels are generated, representing the two radar passes over the same area. The backscatter is modelled as the complex addition of several components, each of them representing a scattering mechanism. The amplitude of each component is estimated from the independent scattering contributions to the total backscatter, as predicted by the RT2 backscatter intensity model. The phase of each weather dependent component is defined with a probability function which represents the variability of the scatterers' position due to their wind driven

random motion. It is at this particular point that the measurements made on wheat come into play, as they are used to define the phase distribution of the weather dependent components of the complex backscatter. The phase distributions were shown to be well approximated by a Gaussian distribution. In addition to this, the existence of a spatial correlation of the wheat motion in areas of about 0.5 m^2 is used in the model to divide each weather dependent component into smaller elements representing individual "cells" of coherent motion within the radar ground resolution cell. Modelling the complex backscatter in this way is a simplified approach which does not have the complexity of a coherent backscatter model based on the geometry, orientation, and scattering properties of the crop elements. However, it allows to make a quantitative estimate of the coherence, which can be used to state on its potential use for agricultural applications, and it shows how motion measurements can be integrated into a modelling approach.

Coherence model outputs over a wheat field

The influence of radar parameters (resolution, wavelength, incidence angle, repeat-time) and of the wind conditions on the coherence from wheat was assessed with the model. Resolution was shown to have a limited impact on coherence, except at very fine resolutions, where the model predicts an increase. Coherence increases with the radar wavelength, due to the increasing contribution of surface scattering processes and to the insensitivity of vegetation motion at long wavelengths. The range of wavelengths at C-Band corresponds to the highest sensitivity to wind conditions. Coherence decreases with increasing incidence angle because of the increasing contribution of vegetation scattering at high incidence, and because of the higher sensitivity to horizontal displacement in the crop canopy. The highest sensitivity is found at incidence angles ranging between 20° and 30°. The time between the two radar passes affects the coherence mainly at the beginning of the season, when the first pass of the radar occurs before the main growth phase in April/May, and the second pass after or during that period.

Radar parameters such as those of the ERS satellites are suited to crop monitoring, but there is an intrinsic variability of the coherence due to the changeable wind conditions. The model predicts that coherence from the same wheat field can vary by as much as 0.2 depending on the wind conditions at the time of the radar passes. Coherence from a wheat field was calculated with ERS-1/2 Tandem data collected in 1995 and 1996. The model estimates were compared to this Tandem coherence and showed a good qualitative agreement, but a full validation of the model would require SAR data and ground truth measurements to be collected simultaneously. The temporal variation of the coherence throughout the season shows that it is sensitive to changes of the bio-physical properties of the wheat, from its main growth period in May to its ripening in July and August.

8.2 Relation to the initial objectives of the research and further work

The initial objectives of the research were presented in the introduction of this report, and formally listed in section 2.5.2. This section returns to these objectives and shows that they were met, with a certain number of restrictions or comments which are also discussed. They lead to areas of further developments of the research.

Objective 1: database of three-dimensional wheat motion and wind velocity

Wheat velocity and wind motion data are provided on the CD attached with this report. It is made available for further applications of SAR backscatter intensity or SAR interferometry, but it can in principle be used for types of studies. The methodology to apply in order to make the measurements was demonstrated in summer 2000, and it can be used more extensively in future growth seasons to make measurements from crop emergence to harvest at regular time intervals, in order to increase the database of wheat motion. The system should also be used to make measurements on other crops, in order to analyse the differences with wheat and, again, increase the database of wind and motion measurements.

It is suggested that future crop motion measurements are made on as many elements as possible, in order to increase the statistical significance of the relationships obtained. In particular, the motion of elements other than the wheat heads would allow to refine the assumptions made in the coherence model concerning these elements (leaves, stalks). Measuring the motion of these elements *in situ* is difficult because they are deeper inside the vegetation volume and do not appear clearly on the video images. The possibility to make these measurements on a single plant should be investigated. Two possible ways to achieve this are to film a wheat plant at the edge of a field, or to place a single plant (or a limited number) in a wind tunnel. The latter is achievable with the facilities available at Cranfield University.

Objective 2: Low cost, portable motion measurement system

The total cost of the three-dimensional motion measurement system is estimated at about £ 2000, based on the prices at which the equipment was bought in 1999 and 2000. As mentioned earlier, the video cameras, the acquisition card, and the computer are likely to be cheaper in the future.

Only the two video cameras, tripods, and a calibration reference frame are required for field measurements. These items are easily transportable and can be placed to fit different viewing geometries which depend on the application the system is used for.

The limiting factor of the system in its current form is the processing time of the video data, mainly due to the size limit imposed on files, which requires the video data to be processed in sequences of 1 minute. Additional video data is available on tape for processing and this report provides the necessary synchronisation information with the wind data sets. The inclusion of new technology in the field of video data acquisition would decrease the pre-processing time and therefore allow a faster

access to the motion data. In particular, the potential use of other digital video formats should be investigated, as it may be possible to make real-time downloads to a computer. Processing more than a single minute of data depends on the possibility to use another video format than uncompressed AVI for target tracking. Ways to overcome the 2 Gbyte size limit on files should also be investigated.

It is suggested that the filtering techniques presented in section 4.6.8 as potential improvements of the tracking algorithms are used more systematically. This is especially the case if the object to track is moving fast in the field of view of the camera, or if it has a low contrast with the surrounding background.

Finally, the applicability of the system to other cases should be investigated, as it has the potential to provide valuable information in a wide range of applications. It should be noted here that the system developed for the purposes of this research has been used successfully by another student at Cranfield University to determine the trajectory of planes landing and taking off at the Cranfield airfield.

Objective 3: relationships between wheat motion and wind velocity

The data collected from May to August 2000 were used to derive relationships between wheat motion and wind velocity, based on values averaged over the 1 minute of video data processed. The analysis of the wind and wheat motion data provided some insights into the understanding of the interactions between the turbulent wind and the canopy. The study indicates that detailed relations between the two are difficult to highlight, so it is suggested that future projects aiming to relate crop motion and wind at canopy height for coherence modelling base their analysis on average values and statistical properties.

A potential further area of study is the determination of the wind field structure above the canopy. It can show the spatial extent over which the vegetation affects the wind flow directly above it. More directly relevant to coherence modelling is the measurement of the correlation distance, because it determines the area in the wheat field over which the crop elements are defined to move coherently. With additional measurement data, it is interesting to estimate the variation of the correlation distance with wind speed, and to determine the value of this distance for other crops.

Objective 4: potential use of coherence for agricultural monitoring

The wind and wheat motion measurements were used as inputs in the coherence estimator. They are used to define the number of independent cells of motion in the radar ground resolution cell, and to define the phase distribution of the weather dependent components of the complex electric field generated by the model. Analysis of the model estimates showed that coherence obtained from the radar configuration of the ERS satellites is variable with the wind conditions and therefore difficult to use in empirical relationships without prior knowledge of the wind speed at the time of the radar passes. The study concludes that there is a need to develop a coherent backscatter model from which coherence could be predicted with the specification of the elements in the vegetation volume and the motion of these elements (forward model). Retrieval of bio-physical parameters can then be attempted by model inversion. The research showed that the introduction of motion measurements is

necessary to develop coherent backscatter models, and pointed out that validation of these models requires simultaneous measurements of crop motion and SAR data. In practice, these measurements are likely to be more easily achievable in laboratory conditions.

The study points towards the conclusion that the coherence is more adapted for purposes involving general thresholds of the coherence values, for example for land-use classification or qualitative monitoring of crops and farming practice. Quantitative use of the coherence can be made but requires a more accurate knowledge of the conditions at which the SAR data are collected, and is subject to the existence of accurate backscatter models usable for inversion.

A radar configuration similar to that of the ERS satellites (C-band, incidence angle 23°) is appropriate to the use of coherence for agricultural applications because it yields a high sensitivity to the vegetation elements, which are the elements of main interest for crop monitoring. Different incidence angles or wavelengths would increase the sensitivity to surface parameters or, at the other extreme, would yield consistently low coherence for all vegetation types. The study showed that departing from the ERS wavelength and incidence angle would result in significant changes in the coherence derived from the SAR data. For that reason it is suggested that future SARs keep the same configuration, because it maximises the potential use of coherence for agricultural applications and allows comparison with the existing sets of SAR interferometric data. These conclusions are drawn from the point of view of crop monitoring only and are not generally true for other applications. It is difficult anyway to design a SAR system which serves equally well different research applications.

8.3 Conclusion

This report covers a wide range of topics and brings together research fields not usually used in conjunction with each other. Some of the issues raised would have required dedicated research and, because of the nature of the work presented here, have been left as open areas for future developments. This is not seen as a weakness but as a strength of the study presented here, because it combines three important sides common to most scientific research projects: the measurement and analysis of data, the use of these data to develop a mathematical model, and the formulation of conclusions based on the understanding of the model outputs.

The development of the motion measurement system, the collection of wheat motion and wind velocity data, and the assessment of the potential of coherence for agricultural applications based on these data, are the three main original contributions of this research. It is hoped that further studies can build on them in the future.

Bibliography

[1] A. Touré, K.P.B. Thomson, G. Edwards, R.J. Brown, and B.G. Brisco. Adaptation of the MIMICS backscattering model to the agricultural context-wheat and canola at l and c band. *IEEE Transactions on Geoscience and Remote Sensing*, 32(1):47–61, January 1994.

[2] A.M. Sardar. The evolution of space-borne imaging radar systems: A chronological history. *Canadian Journal of Remote Sensing*, 23(3):276–280, September 1997.

[3] L.J. Porcello, R.L. Jordan, and J.S. Zelenka et al. The apollo lunar sounder radar system. *Proceedings of the IEEE*, 62(6):769–783, June 1974.

[4] L.C. Graham. Synthetic interferometer radar for topographic mapping. *Proceedings of the IEEE*, 62(6):763–768, June 1974.

[5] R.M. Goldstein, H.A. Zebker, and C.L. Werner. Satellite radar interferometry: two-dimensional phase unwrapping. *Radio Science*, 23(4):713–720, July-August 1988.

[6] C. Seynat, R. Smith, and S.E. Hobbs. Commercial viability of satellite constellations as future earth observation systems. In *Remote Sensing Society Conference*, pages 841–848, Swansea, Wales, September 1999.

[7] F.T. Ulaby. SAR biophysical retrievals: Lessons learned and challenges to overcome. In *2nd International Workshop on Retrieval of Bio- and Geo-Physical Parameters from SAR data for Land Applications*, ESA SP-441, pages 19–25, Noordwijk, The Netherlands, October 1998.

[8] J.I.H. Askne, P.B.G. Dammert, L.M.H. Ulander, and G. Smith. C-band repeat-pass interferometric SAR observations of the forest. *IEEE Transactions on Geoscience and Remote Sensing*, 35(1):25–35, January 1997.

[9] M. Santoro, J.I.H. Askne, P.B.G. Dammert, J.E.S. Fransson, and G. Smith. Retrieval of biomass in boreal forest from multi-temporal ERS-1/2 interferometry. In *2nd International Workshop on ERS SAR Interferometry Fringe '99*, Liège, Belgium, November 1999.

[10] U. Wegmüller and C.L. Werner. SAR interferometric signatures of forest. *IEEE Transactions on Geoscience and Remote Sensing*, 33(5):1153–1161, September 1995.

[11] U. Wegmüller and C.L. Werner. Retrieval of vegetation parameters with SAR interferometry. *IEEE Transactions on Geoscience and Remote Sensing*, 35(1):18–24, January 1997.

[12] S. Remondiere and H. Laur. The use of ERS SAR data for land applications: an overview of ESA ERS announcement of opportunity achievements. In *2nd International Workshop on Retrieval of Bio- and Geo-Physical Parameters from SAR data for Land Applications*, ESA SP-441, pages 27–33, Noordwijk, The Netherlands, October 1998.

[13] M. Engdahl and M. Borgeaud. ERS-1/2 tandem interferometric coherence and agricultural crop height. In *2nd International Workshop on Retrieval of Bio- and Geo-Physical Parameters from SAR data for Land Applications*, ESA SP-441, pages 121–127, Noordwijk, The Netherlands, October 1998.

[14] B. Moeremans and S. Dautrebande. The use of ERS SAR interferometric coherence and PRI images to evalluate crop height and soil moisture. In *2nd International Workshop on* ERS SAR *Interferometry Fringe '99*, Liège, Belgium, November 1999.

[15] X. Blaes, P. Defourny, D. Derauw, and C. Barbier. InSAR coherence for crop parameter monitoring. In *2nd International Workshop on* ERS SAR *Interferometry Fringe '99*, Liège, Belgium, November 1999.

[16] P. Bally. Optical-radar complementarity for land applications: The SPOT image coherence product. In *2nd International Workshop on* ERS SAR *Interferometry Fringe '99*, Liège, Belgium, November 1999.

[17] F.T. Ulaby, R.K. Moore, and A.K. Fung. *Microwave Remote Sensing, Active and Passive. Volume 1: Fundamentals and Radiometry.* Artec House Inc., 1981. ISBN 0-89006-190-4.

[18] F.T. Ulaby, R.K. Moore, and A.K. Fung. *Microwave Remote Sensing, Active and Passive. Volume 2: Radar Remote Sensing and Surface Scattering and Emission Theory.* Artec House Inc., 1982. ISBN 0-89006-191-2.

[19] J.C. Curlander and R.N. McDonough. *Synthetic Aperture Radar: Systems and Signal Processing.* Wiley series in remote sensing. J.Wiley and Sons Inc., 1991. ISBN 0-471-85770-X.

[20] B.C. Barber. Theory of digital imaging from orbital synthetic aperture radar. *International Journal of Remote Sensing*, 6(7):1009–1057, 1985.

[21] C. Oliver and S. Quegan. *Understanding synthetic aperture radar images.* Artech House Inc., 1998. ISBN 0-89006-850-X.

[22] A. Papoulis. *Probability, Random Variables, and Stochastic Processes.* Electrical Engineering. McGraw-Hill, 1984. ISBN 0-07-Y66465-X.

[23] D. Derauw. *Phasimétrie par Radar Synthèse d'Ouverture; Théorie et Applications.* Phd thesis, Faculté des Sciences, Université de Liège, Belgium, 1999.

[24] M. Born and E. Wolf. *Principles of Optics.* Pergamon Press, 5^{th} edition, 1975. ISBN 0-08-018018 3.

[25] H.A. Zebker, C.L. Werner, P.A. Rosen, and S. Hensley. Accuracy of topographic maps derived from ERS-1 interferometric radar. *IEEE Transactions on Geoscience and Remote Sensing*, 32(4):823–836, July 1994.

[26] P.B.G. Dammert. Accuracy of INSAR measurements in forested areas. In *Fringe 96 Workshop, ERS SAR Interferometry*, ESA SP-406, pages 37–49, Zurich, Switzerland, 30 September - 2 October 1996.

[27] R. Touzi and A. Lopes. Statistics of the stokes parameters and of the complex coherence parameters in one-look and multilook speckle fields. *IEEE Transactions on Geoscience and Remote Sensing*, 34(2):519–531, March 1996.

[28] R. Touzi, A. Lopes, J. Bruniquel, and P.W. Vachon. Coherence estimation for SAR imagery. *IEEE Transactions on Geoscience and Remote Sensing*, 37(1):135–149, January 1999.

[29] H.A. Zebker and J. Villasenor. Decorrelation in interferometric radar echoes. *IEEE Transactions on Geoscience and Remote Sensing*, 30(5):950–959, September 1992.

[30] F.K. Li and R.M. Goldstein. Studies of multibaseline spaceborne interferometric synthetic aperture radars. *IEEE Transactions on Geoscience and Remote Sensing*, 28(1):88–97, January 1990.

[31] J.O. Hagberg, L.M.H. Ulander, and J. Askne. Repeat-pass SAR interferometry over forested terrain. *IEEE Transactions on Geoscience and Remote Sensing*, 33(2):331–340, March 1995.

[32] F. Gatelli, A. Monti Guarnieri, F. Parizzi, P. Pasquali, C. Prati, and F. Rocca. The wavenumber shift in SAR interferometry. *IEEE Transactions on Geoscience and Remote Sensing*, 32(4):855–865, July 1994.

[33] J.I.H. Askne and G. Smith. Forest INSAR decorrelation and classification properties. In *1^{st} International Workshop on* ERS SAR *Interferometry Fringe '96*, ESA SP-406, pages 95–103, Zurich, Switzerland, October 1996.

[34] G. Smith, P.G.B. Dammert, M. Santoro, J.E.S. fransson, U. Wegmüller, and J.I.H. Askne. Biomass retrieval in boreal forest using ERS and JERS SAR. In *2^{nd} International Workshop on Retrieval of Bio- and Geo-Physical Parameters from SAR data for Land Applications*, ESA SP-441, pages 293–299, Noordwijk, The Netherlands, October 1998.

[35] C. Proisy, F. Sarti, A. Lopes, E. Dufrêne, V. LeDantec, C. Ruiz, P. Borderies, and I. Chênerie. Temporal variations of interferometric coherence over a deciduous forest. In CEOS SAR *Workshop*, Toulouse, France, October 1999.

[36] J.I.H. Askne, P.B.G. Dammert, and G. Smith. Understanding ERS INSAR coherence of boreal forests. In *International Geoscience and Remote Sensing Symposium IGARSS'99*, volume 4, pages 2111–2114, 1999.

[37] T. Börner. Coherent modelling of vegetation for polarimetric SAR interferometry applications. In *2^{nd} International Workshop on Retrieval of Bio- and Geo-Physical Parameters from SAR data for Land Applications*, ESA SP-441, pages 93–98, Noordwijk, The Netherlands, October 1998.

[38] T. Börner. Development of a coherent scattering model for polarimetric SAR interferometry applications. In *International Geoscience and Remote Sensing Symposium IGARSS'99*, volume 2, pages 1414–1416, 1999.

[39] C. Ruiz, P. Borderies, I. Chênerie, E. Mougin, and C. Proisy. Modelling of electromagnetic waves interaction with forest canopies. In CEOS SAR *Workshop*, Toulouse, France, October 1999.

[40] H. Mayer. Wind-induced tree sways. *Trees*, 1:195–206, 1987.

[41] T.K. Flesch and J.D. Wilson. Wind and remnant tree sway in forest cutblocks. II: Relating measured tree sway to wind statistics. *Agricultural and Forest Meteorology*, 93(4):243–258, 1999.

[42] B. Scannell. *Quantification of the Interactive Motions of the Atmospheric Surface Layer and a Conifer Canopy*. Phd thesis, Cranfield Institute of Technology, December 1983.

[43] T.K. Flesch and H. Grant. Corn motion in the wind senescence: 1. motion characteristics. *Agronomy Journal*, 84:742–747, 1992.

[44] T. Maitani. An observational study of wind-induced waving of plants. *Boundary-Layer Meteorology*, 16(1):49–66, February 1979.

[45] J.J. Finnigan. Turbulence in waving wheat. *Boundary Layer Meteorology*, 16(2):181–236, March 1979.

[46] J. Koskinen. The ISAR interferogram generator manual. Technical Report DEX/ED, ESA-ESRIN, July 1995. Version 3.0.

[47] S.E. Hobbs. Weather effects on SAR backscatter for agricultural surfaces. In *Fringe 96 Workshop, ERS SAR Interferometry*, ESA SP-406, pages 179–188, Zurich, Switzerland, 30 September - 2 October 1996.

[48] P.A. Knight. SAR interaction modelling software, contract MRC ref.122.0, Backscatter software user guide. Technical Report Ref. Y/BD/970283/BA402, GEC-Marconi Research Centre, Space Division, Avionics Laboratory, May 1997.

[49] H. Xu. Monitoring leaf area of sugar beat using ERS-1 SAR data. *International Journal of Remote Sensing*, 17(17):3401–3410, 1996.

[50] E.A. Cloutist. Agricultural crop condition monitoring using airborne C-band synthetic aperture radar in southern Alberta. *International Journal of Remote Sensing*, 17(13):2565–2577, 1996.

[51] P. Saich and M. Borgeaud. Interpreting ERS SAR signatures of agricultural crops in flevoland, 1993-1996. *IEEE Transactions on Geoscience and Remote Sensing*, 38(2):651–657, March 2000.

[52] K. Morrison, J. Bennett, G. Cookmartin, A. McDonald, and S. Quegan. Very high resolution microwave measurements of the scattering from vegetation. In *Remote Sensing Society Conference*, pages 15–21, Swansea, Wales, September 1999.

[53] F.T. Ulaby, R.K. Moore, and A.K. Fung. *Microwave Remote Sensing, Active and Passive. Volume 3: From Theory to Apllications.* Artec House Inc., 1986. ISBN 0-89006-192-0.

[54] F.T. Ulaby, K. Sarabandi, K. McDonald, M. Whitt, and C. Dobson. Michigan microwave canopy scattering model. *International Journal of Remote Sensing*, 11(7):1223–1253, 1990.

[55] P. Ferrazzoli and L. Guerriero. Radar sensitivity to tree geometry and woody volume: a model analysis. *IEEE Transactions on Geoscience and Remote Sensing*, 33(2):360–371, March 1995.

[56] W.H. Press, S.A. Teukolsky, W.T. Vettering, and B.P. Flannery. *Numerical recipes in* C*, the art of scientific computing.* Cambridge Univesity Press, second edition, 1992. ISBN 0-521-43108-5.

[57] F. Domps. Retrieval of earth surface biophysical parameters from SAR data. Msc thesis, Cranfield University, 1999.

[58] Y. Yakimovsky and R. Cunningham. A system for extracting three-dimensional measurements from a stereo pair of TV cameras. *Computer graphics and image processing*, 7:195–210, 1978.

[59] D.B. Gennery. Stereo vision for the acquisition and tracking of moving three-dimensional objects. *Techniques for 3-D Machine Perception*, pages 53–74, 1986. Elsevier Science Publishers B.V.

[60] T. Schenk. Object recognition in digital photogrammetry. *Photogrammetric record*, 16(95):743–762, April 2000.

[61] I. Tsatsakis, E. Kayafas, V. Loumos, and G. Cambourakis. Using low-cost video cameras in automation, a close range photogrammetry approach. In *Proceedings of the IEEE International Symposium on Industrial Electronics*, pages 523–528, July 1995.

[62] J.F. McGowan. AVI overview. http://www.jmcgowan.com/avi.html, 1996-2000. Last visited 23^{rd} August 2000.

[63] S.E. Hobbs. Calibration and performance evaluation of a lightweight propellor anemometer for micrometeorological research. *Boundary-Layer Meteorology*, 68:259–273, 1994.

[64] Y. Philippe. Development of a PC-AT based field anemometry measurement system. Msc thesis, Department of Avionics, College of Aeronautics, Cranfield University, August 1993.

[65] J.S. Bendat and A. G. Piersol. *Random data: Analysis and measurement procedures*. Wiley-Interscience, 2^{nd} edition, 1986. ISBN 0-471-04000-2.

[66] X. Blaes and P. Defourny. Crop parameters retrieval by SAR phasimetry. In CEOS SAR *Workshop*, Toulouse, France, October 1999.

[67] T.K. Flesch and R.H. Grant. Corn motion in the wind during senescence: 2. effect of dynamic plant characteristics. *Agronomy journal*, 84:748–751, August 1992.

[68] R.E. Walpole and R.H. Myers. *Probability and statistics for engineers and scientists*. Macmillan Publishing Company, maxwell-macmillan international edition, 1989. ISBN 0-02-946910-4.

[69] ESA-ESRIN. Descw: Display earth remote sensing swath coverage for windows. http://earth.esa.int/l2/10/descw. Last visited 15^{th} October 2000.

[70] M. Hallikainen, F. Ulaby, M. Dobson, M. El-Rayes, and L. Wu. Microwave dielectric properties of wet soil - part 1: Empirical models and experimental observations. *IEEE Transactions on Geoscience and Remote Sensing*, GE-23(1):25–34, January 1985.

[71] J.M. Gere and S.P. Timoshenko. *Mechanics of Materials*. Van Nostrand Reinhold (International), second edition, 1987. ISBN 0-278-0040-1.

[72] J.D. Anderson. *Fundamentals of Aerodynamics*. McGraw-Hill, international edition, 1991. ISBN 0-07-001679-8.